Energy Storage in Carbon Nanotube Super-Springs

by

Frances Ann Hill

B.A.Sc. Systems Design Engineering
University of Waterloo, 2006

Submitted to the Department of Mechanical Engineering
In partial fulfillment of the requirements for the degree of

Master of Science in Mechanical Engineering
at the
MASSACHUSETTS INSTITUTE OF TECHNOLOGY

June 2008

Author .....
Department of Mechanical Engineering
May 9, 2008

Certified by .....
Carol Livermore
SMA Assistant Professor of Manufacturing
Thesis Supervisor

Accepted by .....
Lallit Anand
Chairman, Department Committee on Graduate Students

Energy Storage in Carbon Nanotube Super-Springs

by

Frances Ann Hill

Submitted to the Department of Mechanical Engineering
on May 9, 2008, in partial fulfillment of the
requirements for the degree of
Master of Science in Mechanical Engineering

Abstract

A new technology is proposed for lightweight, high density energy storage. The objective of this thesis is to study the potential of storing energy in the elastic deformation of carbon nanotubes (CNTs). Prior experimental and modeling studies of the mechanical properties of CNTs have revealed nanoscale structures with a unique combination of high stiffness, strength and flexibility. With a Young's modulus of 1 TPa and the ability to sustain reversible tensile strains of 6% [1, 2] and potentially as high as 20% [3-5], mechanical springs based on these structures are likely to surpass the current energy storage capabilities of existing steel springs and provide a viable alternative to electrochemical batteries. Models were generated to estimate the strain energy of CNTs subject to axial tension, compression, bending and torsion. The obtainable energy density is predicted to be highest under tensile loading, with an energy density in the springs themselves about 2500 times greater than the maximum energy density that can be reached in steel springs, and ten times greater than the energy density of lithium-ion batteries. Practical systems will have lower overall stored energy density once the mass and volume of the spring's support structure and any additional extraction hardware are taken into account, with a maximum achievable stored energy density predicted to be comparable to lithium-ion batteries. Due to the poor load transfer between MWCNT shells and the radial deformation of larger SWCNTs, bundles of SWCNTs with diameters of 1 nm or smaller are identified as the best structure for high-performance springs. The conceptual design of a rechargeable portable power source is developed as a tool to study the performance and feasibility of building such a device. In this design, energy is stored in a grouping of densely-packed, aligned CNTs stretched in tension. The design includes an escapement mechanism to regulate the energy release from the spring and a generator to convert the output work from the spring into the electrical domain. The results indicate that the performance of the power source scales well with size so there is flexibility in choosing the overall scale of the device. Achieving a high fraction of CNTs in the overall device proved to be challenging. Future work should concentrate on building and testing high-quality, densely-packed macroscale SWCNT assemblies that are expected to form the basis of super-springs for implementation into practical devices.

Thesis Supervisor: Dr. Carol Livermore
Title: SMA Assistant Professor of Manufacturing

Table of Contents

1. Introduction

In response to the growing energy requirements of electronics and the need for higher efficiency and higher density energy storage systems, a demand exists for breakthrough technologies in the field of energy storage. Reliable, high density energy storage is key to supplying long-lasting power to applications such as portable electronics and electric vehicles, or storing energy from intermittent renewable power sources such as wind or solar power. Current storage technologies include batteries, fuel, supercapacitors, compressed gas, pumped hydro, mechanical springs and flywheels. Fuel stores chemical energy with an energy density as high as two orders of magnitude greater than batteries, but the need for a combustion engine makes fuel impractical as an energy source for many portable applications. Batteries are the most common and versatile form of energy storage, though cited drawbacks are their low energy density, long recharge times, limited operating temperature range, self-discharge and low power densities. Capacitors offer rapid charge and discharge times and high power densities but still cannot match the energy density of batteries. Flywheels, mechanical springs, compressed air and pumped water all store mechanical energy. Although their energy densities are typically lower than batteries, mechanical energy storage devices can deliver long lifetimes and high power in a reliable, cost-effective and environmentally safe manner. While different energy storage systems are well-suited for particular modes of usage, none are ideal for all applications. There is still a need for sustainable, high density energy storage systems that offer both high energy density and high power density. Further research is being conducted to improve upon the capabilities of the current energy storage methods, such as batteries and capacitors, but it is worthwhile to also consider new, alternative technologies that may improve upon the limitations of the conventional storage systems.

An alternative form of energy storage is proposed based on the elastic deformation of carbon nanotubes (CNTs). Carbon nanotubes, first observed in 1991 [6], are carbon-based molecules with ideal graphitic bonding in high aspect ratio cylindrical structures a few nanometers in diameter and with lengths on the order of microns. Studies of their mechanical properties have revealed a remarkable combination of high stiffness, strength, flexibility and

low density, properties that set CNTs apart from all other materials. The carbon-carbon bond in graphite is the strongest bond found in nature [7], and a CNT is effectively a sheet of graphite rolled into a cylinder. The advantage of nanoscale materials is their ability to reach near-ideal crystallinity with few defects and impurities. The result is nanoscale materials with mechanical properties far superior to those of bulk materials [8]. The Young's modulus of CNTs is 1 TPa, five times greater than that of steel. Their failure strength of 50 to 200 GPa is over a hundred times greater than the strength of steel. With their strong bonding structure, CNTs can sustain considerable deformation in a reversible manner. Experimentally, CNTs have been shown to be capable of sustaining tensile strains as high as 6% [1, 2], and strains in defect-free CNTs are predicted by theoretical models to be as high as 20-30% [3-5].

These mechanical properties have motivated a study to explore the potential of using CNTs as "super-springs" for high density, lightweight, reversible, mechanical energy storage. Elastic strain energy is stored in a CNT by deforming it under an applied load. Once the load is removed, the released energy from the CNT can be used to perform mechanical work. The ability of CNTs to deform reversibly, along with their high strength and stiffness, indicate that springs made of CNTs would be an ideal medium for mechanical energy storage. Such a spring is expected to be able undergo repeated charge-discharge cycles elastically and without fatigue. The term "super-spring" refers to the expectation that CNTs will store elastic strain energy with a density several orders of magnitude higher than conventional spring materials such as steel. Strain energy density in a material is proportional to the product of its Young's modulus and the square of an applied strain. Accordingly, springs made of CNTs are expected reach energy densities as much as four orders of magnitude greater than the energy density of steel springs and on the same order of magnitude as the energy density of lithium-ion batteries. While a number of applications already take advantage of the unique mechanical properties of CNTs, including scanning probe tips, polymer composites, torsional springs and foams, the use of CNTs for energy storage is a new application that has been little studied to date.

CNTs present a useful alternative to conventional energy storage technologies. The ability of springs to discharge very rapidly suggests that CNTs can reach not only high energy densities but also high power densities. Because elastic strain energy relies on stretching bonds rather

than chemical reactions, advantages of CNT energy storage over batteries are a potentially infinite numbers of charge-discharge cycles, long term storage without losses, little or no degradation of the storage medium over time, rapid recharging and temperature insensitivity.

An important distinction between CNTs as a storage material and conventional energy storage devices is their small size. Individual CNTs have diameters measured in nanometers and lengths on scales ranging from microns to millimeters. For CNTs as springs to store useful amounts of energy, they must be assembled into larger groupings. An important challenge is developing methods of arranging the CNTs in such a way that a single mechanical load can deform many CNTs in a macroscale assembly at once while maintaining the mechanical properties and energy storage characteristics of a single CNT. Excellent load transfer is required between individual tubes so that an applied load is evenly distributed among all tubes in a grouping.

Given a spring made of CNTs, the next step is to study how it can be incorporated as the energy storage element into a rechargeable power source. Energy can be input into a spring using a motor, stored for a period of time prior to the spring's release, and once released, converted into electrical energy using a generator. For large-scale applications, achieving macroscale levels of energy storage can be done using either many small springs that release their energy at once or a single, much larger spring that is itself capable of storing a macroscale amount of energy.

1.1. Thesis outline

The following chapters will focus on assessing the feasibility of using CNT super-springs for energy storage. Chapter 2 provides background material on the atomic structure, methods of synthesis, mechanical properties, macroscale assemblies and applications of CNTs. Chapter 3 presents models that are used to predict the strain energy density of CNTs under different modes of mechanical deformation. These estimates are compared to the energy storage capabilities of other common storage devices. Chapter 4 examines the architecture of a power source that stores energy in the deformation of CNT springs. In particular, the question of scale will be addressed to evaluate the feasibility of building power sources at the nanoscale or at the

macroscale. Chapter 5 presents the design of a conceptual microscale portable power source. A model is used to examine the effect of scale on energy storage, power output, efficiency and system performance while assessing the potential utility and identifying the implementation issues associated with building such a device. Finally, Chapter 6 summarizes the results and suggests directions for the project to take in the future.

2. Carbon nanotubes: structure and properties

2.1. Carbon nanotube structures

2.1.1. Atomic structure

The structure of a CNT is similar to a graphene sheet rolled into a seamless cylinder with capped ends. Both CNTs and graphite have sp^2 bonding, a highly stable covalent bond that is stronger than the sp^3 bonding in diamond and is responsible for the high strength and stiffness of CNTs [8, 9]. Three σ bonds form the strong planar hexagonal network and an out-of-plane π bond gives the CNT its thermal and electrical conductivity. The curvature of the graphene sheet causes the π bond to be more delocalized than in a planar sheet, which results in a structure that is mechanically stronger and more conductive than graphite [10].

There are two types of CNTs: single walled carbon nanotubes (SWCNTs), with a single shell, and multi walled carbon nanotubes (MWCNTs), made of two or more concentric shells as shown in Figure 2.1. The presence of defects in a largely hexagonal network can create more diverse shapes. Stone-Wales defects, pentagon-heptagon pairs in the hexagonal network, result in non-planar structures that include capped nanotubes, helically coiled nanotubes, toroidal structures, cones, and branched nanotubes.

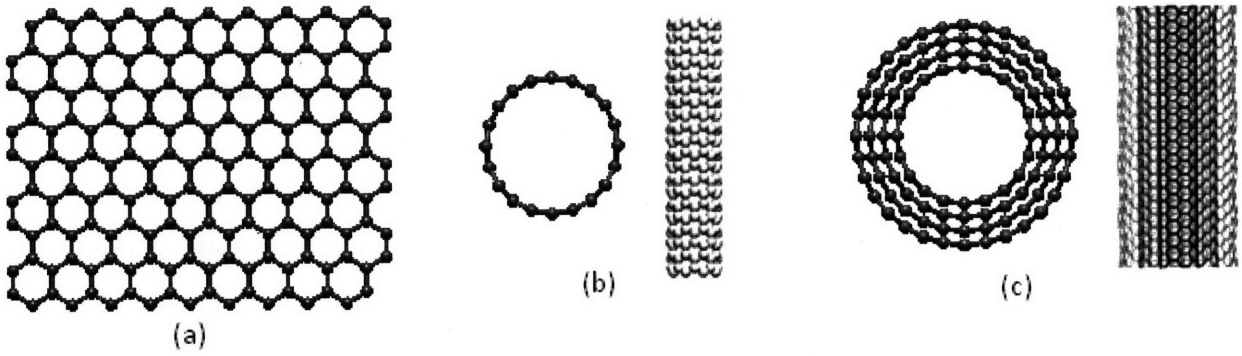

Figure 2.1: (a) Planar sheet of graphene rolled into (b) a SWNCT and (c) a MWCNT with four shells. [11]

2.1.1. Single-walled carbon nanotubes

A SWCNT is single graphene sheet that has been rolled into a cylinder and capped. The structure of a SWCNT is uniquely characterized by a diameter d and a chiral angle θ, or equivalently by a chiral vector [12]. The chiral vector C_h is defined perpendicular to the CNT axis, as shown in Figure 2.2 (a). Its length is equal to the perimeter of the cross-section, so that the ends of the vector overlap in the rolled structure. A translation vector T is defined in the direction of the CNT axis, perpendicular to C_h. The chiral vector is expressed as $C_h = na_1 + ma_2 = (n, m)$, where a_1 and a_2 are unit vectors. Special structures include armchair CNTs when n=m and zigzag CNTs when m=0, as shown in Figure 2.2 (b). Chirality affects electrical conductivity, determining whether a CNT is metallic or semiconducting, but has little impact on mechanical stiffness and strength.

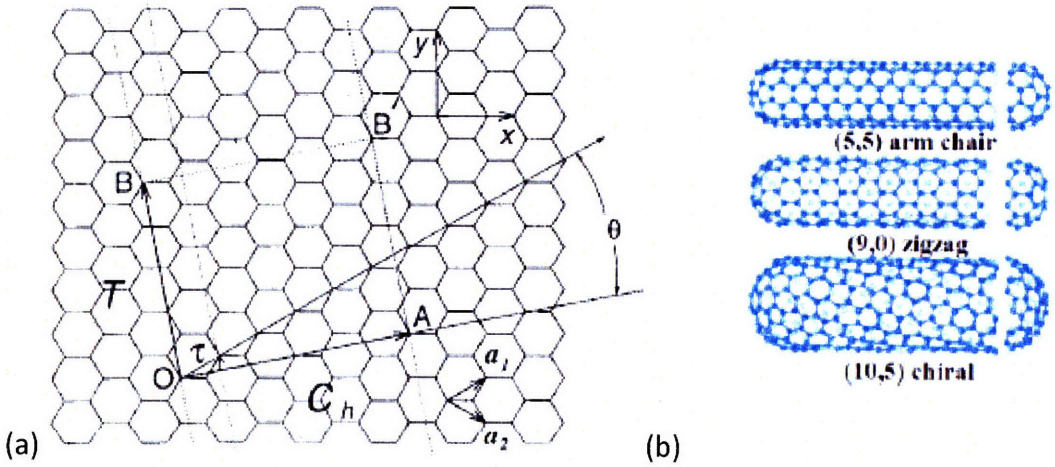

(a) (b)

Figure 2.2: (a) An unrolled graphene sheet showing the chiral vector C_h and translation vector T of a CNT [12]. (b) Examples of armchair, zigzag and chiral CNTs [8].

Experiments have shown that the diameters of SWCNTs fall in the typical range of 0.6 nm to 2 nm, though diameters as small as 0.4 nm and as large as 3 nm have been observed [10]. With small diameters and long lengths, SWCNTs can have aspect ratios as high as 1000 [7]. The stability of a SWCNT cross-section decreases as diameter size increases. The cross-section of a SWCNT deforms in the radial direction when it comes into close contact with another tube or a substrate because of the van der Waals interactions between them, forming structures called

nanoribbons. The flattening effect becomes more pronounced in tubes with larger diameters [13].

During synthesis, CNTs often form groupings because of the attractive van der Waals forces between them. The products of CNT synthesis processes are typically SWCNTs bundles [8], densely packed groupings of several hundred tubes arranged in a hexagonal lattice.

2.1.2. Multi-walled carbon nanotubes

Each concentric shell of a MWCNT has the same structure as a SWCNT, though each shell can have its own chirality. The interactions between neighbouring shells are based on van der Waals forces, and these are generally weak. MWCNTs typically have an outer diameter less than 100 nm and inner diameter greater than 2 nm [10], and can have between two to over a hundred shells [14]. The distance between adjacent shells in a MWCNT is measured to be 0.34 nm, the same distance as the separation between graphene sheets in graphite.

2.2. Carbon nanotube synthesis

Synthesis techniques have been developed to grow CNTs with millimeter-scale lengths, high purity, low defect density, rapid growth rates and at reasonable costs. Three common synthesis techniques are the arc discharge method, laser ablation and chemical vapour deposition.

The arc discharge method applies a voltage between two graphite electrodes spaced about 1 mm apart. A chamber is filled with low pressure helium or argon. The temperature of the gas between the electrodes reaches above 3000^{o}C and the carbon in the electrodes sublimates to form a plasma. The anode is consumed as deposits form on the cathode. MWCNTs grow without the need of a catalyst, and these deposit in bundles on the cathode. SWCNTs can be grown when catalyst particles such as iron, nickel, cobalt or yttrium are added to the graphite anode. SWCNTs also deposit in bundles on the cathode. The lengths of the produced CNTs are relatively short, generally about 20 μm long [14]. The geometry and type of CNTs produced can be varied by changing the pressure and feed rate of the background gas, the temperature, type of catalyst, the applied current and voltage and the distance between the electrodes. This

technique produces CNTs of high quality and with few structural defects, but the CNT products are mixed with graphite, metal clusters and amorphous carbon that must be separated to obtain purified CNTs. Drawbacks of this method include limited control of CNT lengths and diameters and the high cost of the gases and electrodes used in the synthesis process [15].

The laser ablation technique sends laser pulses toward a graphite target located in a quartz tube filled with low pressure argon. The tube passes through a furnace operating at 1200°C. The laser pulses decompose the target into small carbon aggregates which recombine to form long nanotubes in the vapour phase. These are carried with the surrounding gas toward a cooled collector made of copper at the end of the tube where they deposit in bundles with lengths on the order of tens of microns. The properties of the CNTs are varied by changing the catalyst, gas composition, temperature, pressure, flow conditions and laser pulse intensity. Graphite and metal catalyst particles also deposit on the collector and these must be removed using purification techniques. A target made of graphite results in the formation of MWCNTs while a target of graphite mixed with catalyst particles forms SWCNTs. CNTs produced with laser ablation are typically of high quality and contain few structural defects.

Growth of SWCNTs or MWCNTs using chemical vapour deposition (CVD) takes place on a small substrate that has been patterned with catalyst particles, often iron, nickel or cobalt. The substrate is placed in a quartz tube inside a furnace that heats the tube to a temperature between 500 and 1000°C. Hydrocarbon gas mixtures of methane, ethane, ethylene or acetylene flow through the tube during the growth period, which is followed by the flow of an inert gas while the tube cools down. The process parameters are temperature, gas composition and type of catalyst which determine the number of walls, lengths, and diameter distributions of the CNTs. The result is densely packed, vertically aligned CNTs grouped into bundles on a substrate, mixed with amorphous carbon and catalyst particles. Alignment of the CNTs depends on the process parameters, and can range from tangled, poor alignment to relatively good vertical alignment [16]. The lengths of CVD-grown CNTs can be as long as millimeters and MWCNTs can be grown with more than a hundred shells [14]. The defect density of CNTs grown using CVD is higher than with the other two methods because of the low temperature used in the process,

though it can be improved through annealing [17]. An important advantage of CVD is its ability to produce bulk quantities of CNTs at lower costs than other methods.

The highest quality CNTs are synthesized using arc-discharge and laser ablation methods that operate at very high temperatures. CNTs produced with CVD have higher defects densities and inferior mechanical properties [10] but the highest purity. An important advantage of CVD and the arc discharge method is that they are well-suited for large-scale production, while laser ablation is not [10]. CVD produces the longest tubes, provides the most control over diameter distribution and grows CNTs in ordered, vertically aligned arrays.

2.3. Mechanical properties

Considerable work has been done to experimentally characterize the properties of SWCNTs and MWCNTs despite the challenges posed by their nanoscale sizes. CNTs are difficult to manipulate, align and attach to surfaces. The experimental quantities being measured, such as length, diameter, force and displacement are small themselves and limited resolution at that scale introduces uncertainty in the measured data. Defects can have a large impact on the properties being measured, but these defects are hard to characterize.

A number of techniques have been devised to measure the mechanical characteristics of CNTs. The Young's modulus has been determined by measuring the amplitude of thermal vibrations of CNTs in a TEM [18], and embedding CNTs in a polymer and measuring stress using micro-Raman spectroscopy [19]. Other techniques, including performing tensile tests by mounting CNTs between AFM tips [2, 20] and deflecting a suspended CNT using an AFM tip [1, 21], have been used to measure both the Young's modulus and axial strength.

Many different types of models of CNTs have been built to validate the experimental results and explain their observed properties, such as their strength and stiffness, load transfer mechanisms and fracture modes. Common modeling techniques are ab initio methods, molecular dynamics, continuum approaches and finite element methods.

Carbon nanotubes are expected to have a Young's modulus near 1 TPa, the in-plane stiffness of graphite [2]. Assigning a Young's modulus to a CNT is applicable only within a continuum framework in which each shell is assigned an equivalent thickness. Proposed

thicknesses include 0.066 nm by Yakobson et al. [22], 0.154 nm by Liew et al. [11] and 0.076 nm by Wang et al. [23], but the more commonly used shell thickness is 0.34 nm, which is equal to the spacing between graphene sheets in graphite.

Studies have shown that CNTs are able to withstand considerable strains elastically. CNTs can undergo large deformations under axial and radial compression, bending, stretching and twisting reversibly and without permanent atomic defects forming in the hexagonal network of covalent bonds [21, 22]. This behaviour is explained by their nanoscale structure that doesn't form the stress concentrators that lead to failure in macroscale materials [24]. Maximum tensile strains as high as 6% have been measured experimentally to date [1, 2], though modeling studies predict strains in defect-free CNTs as high as 20-30% [3-5]. The experimental measurements are likely lower than the theoretical predictions because of structural imperfections. Strength is limited by the presence of defects and impurities, so high quality fabrication techniques are needed for experimental strains to reach the theoretically predicted values.

A summary of reported values for the Young's modulus of individual SWCNTs, MWCNTs, and ropes of SWCNTs obtained through experimental and theoretical work are listed in Table 2.1. Reported values for the shear modulus of CNTs are listed in Table 2.2. While the results contain some variation, there is generally good agreement between the experimental and theoretical values. Studies have shown that the Young's modulus is independent of the number of shells in a MWCNT and van der Waals interactions between the shells [25], so similar stiffness for both SWCNTs and MWCNTs is expected. The mean values are about 1 TPa for the Young's modulus and 450 GPa for the shear modulus.

Table 2.1: Experimental and theoretical determination of the Young's modulus of CNTs

Author	**Structure**	**Young's modulus**	**Thickness**	**Method**
Lu [25]	SWCNT SWCNT ropes MWCNT	0.97 TPa 0.43 – 0.8 TPa 0.97 – 1.1 TPa	0.34 nm	Empirical force-constant model
Yakobson et al. [22]	SWCNT	5.5 TPa	0.066 nm	Molecular dynamics
Meo et al. [4]	SWCNT	0.92 TPa	0.34 nm	Molecular mechanics and finite elements

Lourie et al. [19]	SWCNT MWCNT	2.8 – 3.6 TPa 1.7 – 2.4 TPa		Micro-Raman spectroscopy
Yu et al. [2]	SWCNT ropes	1.0 TPa	0.34 nm	Tension using an AFM probe
Yu et al. [20]	MWCNT	0.27 - 0.95 TPa	0.34 nm	Tension using an AFM probe
Wong et al. [26]	MWCNT	1.28 ± 0.59 TPa		Bending force measurement using AFM
Salvetat et al. [21]	SWCNT ropes	1 TPa	0.34 nm	Deflection using an AFM tip
Treacy et al. [18]	MWCNT	1.8 TPa		Measurement of thermal vibrations using a TEM

Table 2.2: Experimental and theoretical determination of the shear modulus of CNTs

Author	**Structure**	**Shear modulus**	**Method**
Lu [25]	SWCNT MWCNT	436 – 478 GPa 436 – 541 GPa	Empirical force-constant model
Yu et al. [27]	SWCNT	370-500 GPa	Molecular dynamics
Popov et al. [28]	SWCNT	414	Lattice-dynamical model
Hall et al. [29]	SWCNT	410 ± 36 GPa	Torsional springs

Table 2.3: Mechanical properties of CNTs compared to common engineering materials [10, 30, 31]

Material	**Young's modulus**	**Strength**	**Failure strain**	**Density**
SWCNTs/MWCNTs	1 TPa	50-200 GPa	5-20%	2200 kg/m^3
Graphite	350 GPa	2.5 GPa	0.7%	2200 kg/m^3
Carbon fibres	230 GPa	4.2 GPa	1.8%	1800 kg/m^3
Steel	200 GPa	0.4 GPa	0.2%	7800 kg/m^3
Titanium	116 GPa	0.14 GPa	0.12%	4500 kg/m^3
Wood	16 GPa	0.08 GPa	0.5%	600 kg/m^3
Epoxy	3.5 GPa	0.05 GPa	1.4%	1250 kg/m^3

The mechanical properties of CNTs are compared to the properties of common engineering materials in Table 2.3. The advantage of CNTs over the other materials is apparent. The unmatched combination of high Young's modulus, high strength and low density suggests that CNTs could form the basis of new, high-quality structural materials. The advantage of CNTs over carbon fibres, widely used as a reinforcing material in polymer composites, has motivated the

fabrication of CNT-based polymer composites, as discussed in section 2.5. The properties of CNTs have important implications in terms of mechanical energy storage. Elastic strain energy density u in a material is

$$u = \frac{1}{2} E \varepsilon^2, \tag{2.1}$$

where E is the Young's modulus and ε is the applied strain. With a higher combined Young's modulus and failure strain than any other material, CNTs can store large elastic strain energies, and this has prompted the investigation into the potential of CNTs as springs for mechanical energy storage.

When a small load is applied to a CNT, the induced strain is distributed through the CNT structure. When sufficiently large loads are applied, CNTs can deform into complex buckling patterns [13, 32]. Buckling causes regions of high local strains to develop, and these buckles concentrate most of the deformation [33]. CNTs buckle in bending, compression and torsion, but not in axial tension [22, 34]. These buckles are observed to have regular patterns with characteristic intervals regardless of their position on the nanotube, which suggests that the buckles are a result of the structure rather than defects, and thus are reversible [32]. Both experimental and theoretical studies have shown that the distortions from buckling can remain elastic and reversible, even with local strains as high as 16% [17, 22, 32]. Figure 2.3 shows the calculated strain energy in a (7,7) SWCNT under axial compression as a function of strain [22]. Each singularity on the graph corresponds to a strain at which the nanotube adopts a distinct buckling shape. The critical buckling strain is the strain at which the nanotube first buckles, or equivalently the strain at which the first singularity appears on the graph. Even at strains beyond the first singularity, it is possible for no defects to form among the atomic bonds and for the deformation to remain elastic. Similarly, the plot in Figure 2.4 shows the calculated strain energy in a (10,10) SWCNT as a function of twisting angle [33]. As the angle gets larger, the cross-section of the tube collapses to form a ribbon. The critical shear strain of a CNT under torsion is the shear strain at which the first discontinuity appears in the plot of strain energy as a function of twist angle.

In terms of energy storage, a buckle in a tube is the region where defects are most likely to form. For loading in compression, torsion and bending, applying a load beyond the first buckling

point increases the overall energy that can be stored in the structure, as shown in Figure 2.4 and Figure 2.5. However, beyond the first buckle, the quadratic relation between strain energy and strain is lost and the relation becomes roughly linear. Loading above the buckling point also increases the likelihood of permanent defects forming in the lattice to release the localized strain. To avoid permanent defects forming in the lattice and to maintain elastic behaviour, applying loads above the buckling strains should be avoided for these deformation modes. Loading in tension presents a useful alternative to compression, torsion and bending since buckling is avoided altogether and a quadratic relation is maintained between strain and strain energy up to higher strains. Consequently, tension is a good choice for a loading mode. This issue is addressed in more detail in Chapter 3.

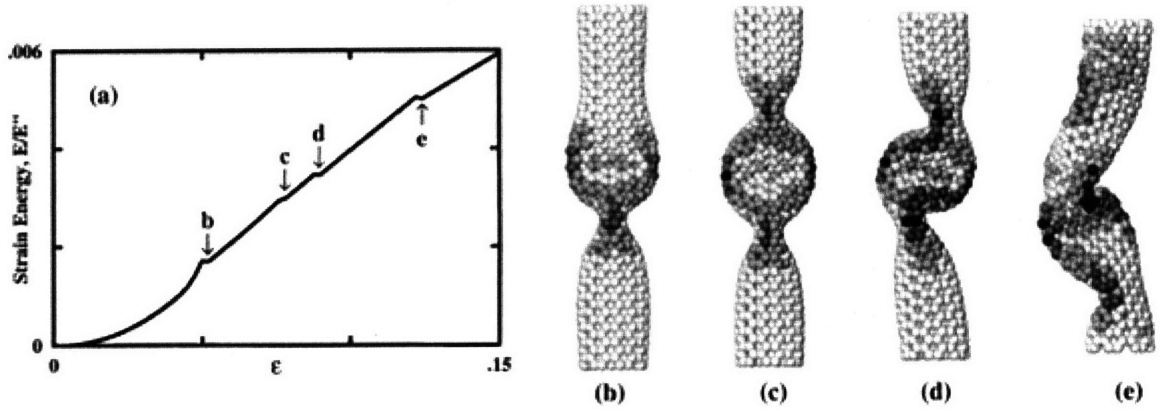

Figure 2.3: Modeled strain energy for a compressed (7,7) SWCNT of diameter 1 nm [22]. The singularities in the strain energy graph at points b, c, d and e correspond to buckling strains. The strain at which buckling first occurs is the critical buckling strain and occurs at 5% in this SWCNT.

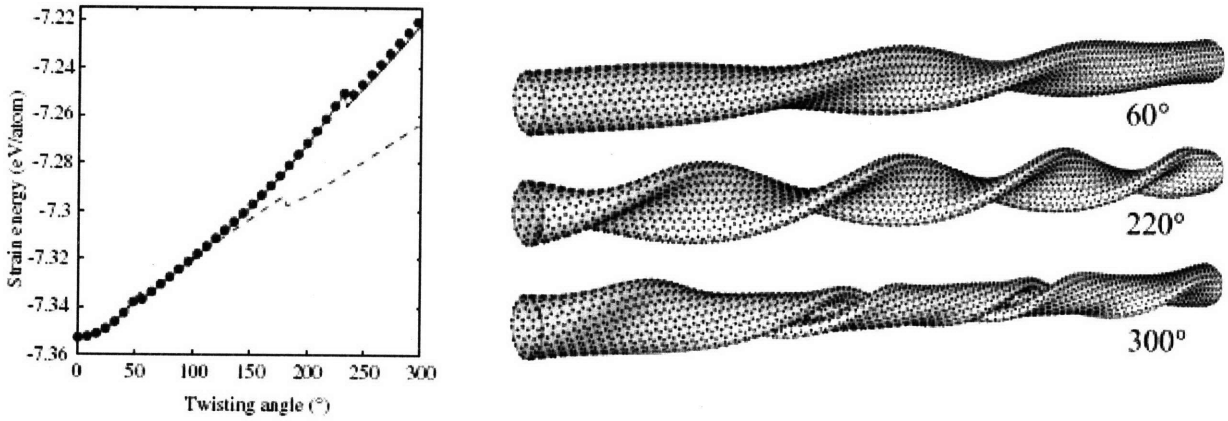

Figure 2.4: Modeled strain energy as a function of twisting angle for a (10,10) SWCNT [33]. The nanotubes are shown in their buckled shapes at different twist angles. The first singularity in the graph occurs at a twist angle of 50°, when the first buckle forms.

Failure of MWCNTs under tension has been described as a "sword-in-sheath" fracture mechanism [20] in which the outer shells fractures and the unaffected inner shells are pulled out. That behaviour is a result of poor load transfer from the outer shell of a MWCNT to the inner shells, with only weak van der Waals forces acting between the layers. A load applied to the outer shell of a MWCNT is largely carried by that outer shell. The effect is to lower the strength of a MWCNT since only the area corresponding to the outer shell contributes to supporting a load, using the continuum assumption. Limited load transfer between shells restricts the usefulness of MWCNTs [8] and indicates that SWCNTs may be the more useful structural material for springs.

Long CNTs have been found to have lower stiffness and strength than short CNTs. Pan et al. tested the strength of very long bundles of MWCNTs produced using CVD with lengths of 2 mm, and measured maximum strains of 0.4% [35]. They attributed their low results to high defect density, which reduces mechanical stiffness and strength. Among synthesis methods, a tradeoff exists between length and defect density. CVD produces the longest CNTs with the highest defect densities, while the arc discharge method and laser ablation technique produce higher quality CNTs but with much shorter lengths, so it is not surprising that CNTs produced by CVD with millimeter lengths are found to have lower strength. Aside from the synthesis process, another explanation is that CNTs with longer lengths are simply larger structures, so they have a higher probability of containing concentrations of defects that will lead to failure [8].

2.4. Applications of carbon nanotubes

A broad range of applications of CNTs have been motivated by their mechanical, chemical, electrical, thermal and optical properties. In electronics, applications include CNTs as field emission electron sources [10, 36], electrode material for lithium-ion batteries [37], as well as in nanoelectronic circuits as transistors [38], logic gates [39] and random access memory elements [40]. Other applications include CNTs as nanosensors [41], nanopipettes [42], nanotweezers [43], for drug delivery [44] and as a storage medium of hydrogen for fuel cells [45].

Recent work has been done to integrate CNTs into energy storage systems. Researchers are developing new supercapacitors that use CNTs in the electrodes [46, 47]. Capacitance is directly related to the surface area of a capacitor's electrodes. Since dense forests of CNTs have very large exposed surface areas and excellent conductivity according to their chirality, CNT forests as electrodes show excellent promise for improving the energy storage capacity of supercapacitors.

An important subset of CNT applications takes advantage of their mechanical properties. For their high aspect ratio, small diameter and high stiffness, CNTs are being attached to the end of AFM probe tips to improve AFM imaging [48]. CNTs are being used to fabricate lightweight high strength polymer composites, and work is being done to develop ceramic and metal composites as well. The combined high strength, high stiffness, low density, high surface area and large aspect ratio of CNTs make them an ideal structure for reinforcement. CNTs can produce composites with higher strength to weight ratios than any other reinforcing materials [8, 49]. To obtain the best matrix composite properties, CNTs must be well dispersed and have good adhesion to the polymer. Challenges to the process include weak interactions between CNT shells in MWCNTs and between tubes in bundles [50] as well as the high cost of obtaining bulk quantities of high quality CNTs. Current research is being done to develop ways of preventing CNT agglomeration, align CNTs throughout a matrix and improve load transfer between the CNTs and the matrix material [51].

CNT have been recommended for use in energy-absorbing composite materials due to their ability to absorb mechanical compression in a reversible manner [52]. For their compressive

strength, Cao et al. propose that forests of CNTs are an ideal material for fabricating strong, lightweight foams that could be used for packaging, energy dissipation and cushioning [53].

Torsional springs are being developed from single CNTs [29, 54, 55]. These devices consist of either a SWCNT or MWCNT placed over a trench patterned into a silicon wafer. The CNT is attached to the wafer at the edges of the trench using patterned metal electrodes, and a metal paddle is attached to the CNT at the centre of the trench. Electrostatic actuation deflects the paddle towards the substrate, inducing a torsional deformation in the CNT. The devices display high sensitivity, good precision and control over the angle of rotation, resilience, and no degradation over time with repeated actuation [29, 54]. Proposed applications of the torsional springs are sensors, optical modulators and high frequency electronics clocks. While these springs are not designed for energy storage, the devices show that elastic springs can indeed be built from CNTs.

Anyone who has deformed a CNT has stored energy, whether as part of an application or while testing the mechanical properties of these structures. As a result, a distinction should be made between incidental energy storage in applications in which CNTs were deformed, and purposeful energy storage with the intent of releasing the energy at a later time to perform useful work. CNTs have already been successfully demonstrated as elastic torsional springs. The use of CNTs as mechanical springs for reversible, elastic energy storage is a new application that has been little investigated to date, and merits further study.

2.5. Macroscale assemblies and their properties

While energy can be stored with high density in a single CNT, grouping individual CNTs into larger assemblies offers the advantages of storing a large amount of energy in a single spring and the ability to manipulate the spring at a macroscopic level. A single CNT can constitute a spring, but it is also important to consider the possibly of building macroscale springs as well. To maintain a mechanical advantage, macroscopic assemblies must be made of CNTs with high purity and low defect density, and demonstrate the same properties and energy storage characteristics as individual CNTs. It is often the case, however, that the mechanical and electrical properties of macroscale assemblies are inferior to those of individual CNTs [56], so

stiffness and strength are important criteria for selecting the best macroscale CNT structure for energy storage. Macroscale structures that can be fabricated from individual CNTs include bundles, mats, fibres, forests and solids.

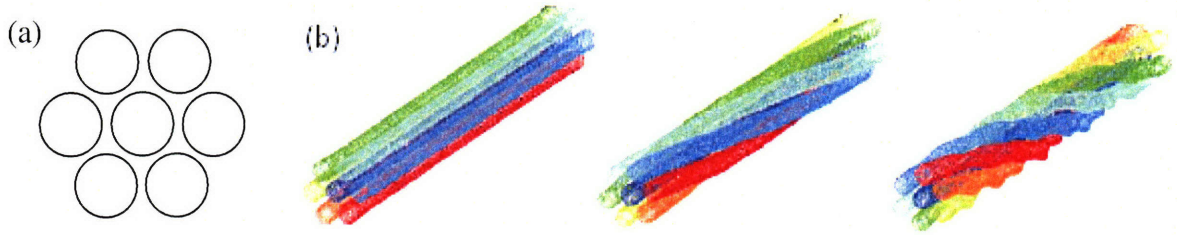

Figure 2.5: (a) Cross section of a bundle showing hexagonal packing. (b) Model of a bundle of straight nanotubes on the left and ropes with twisted nanotubes on the right [57].

Mats of CNTs, also called bucky paper, are created by drying solutions of CNTs to form thin films [58]. The mats are made of CNT bundles arranged in disorganized, tangled networks. The lack of alignment results in poor interactions between the bundles, high porosity and measured stiffness and strength several orders of magnitude lower than individual CNTs [59].

Fibres or yarns are long assemblies of MWCNTs or SWCNTs that are drawn from solutions and spun together [60, 61]. These fibres can be as long as several centimeters to tens of centimeters and have diameters on the order of 50 μm. Ericson et al. report a Young's modulus for a fibre of 120 GPa and a tensile strength of 116 MPa, considerably lower than the stiffness and strength of individual CNTs. Fibres improve upon the mechanical properties of mats with better alignment between the bundles, but still cannot match the stiffness and strength of SWCNTs in the axial direction due to relatively high levels of impurities and imperfect alignment and overlap between bundles [60, 61].

A bundle, often also called a rope, is a naturally occurring dense array of SWCNTs arranged in a lattice with hexagonal packing, as shown in Figure 2.5. The tubes are held together with van der Waals forces, and the bundles can be several hundreds of microns to a few millimeters long [62]. Ideally, the intertube spacing approaches 0.34 nm. The tubes are parallel and highly aligned within the bundle. Bundles of CNTs can also be found in which natural twisting occurs between the strands, and these structures are sometimes called ropes.

A continuous bundle of CNTs is one in which all tubes have the same length and span the entire length of the bundle. Bundles of continuous CNTs are expected to maintain the same stiffness as individual CNTs since the hexagonal network of covalent bonds gives CNTs their stiffness in the axial direction, and this structure remains unchanged in a bundle [21]. Salvetat et al. measured a bundle stiffness of 1 TPa [21], the same value as individual SWCNTs, by deflecting a suspended bundle of SWCNTs using an AFM tip. It is important to note that their measurement technique used bending, which ensured that all tubes within the bundle were loaded during the test. Similar to the interaction between the shells of a MWCNT, the forces between tubes in a bundle are weak van der Waals forces. Yu et al. [2] measured the stiffness of SWCNT bundles by stretching a bundle of SWCNTs in tension. One end of the bundle was attached to the end of an AFM tip using carbonaceous deposits. They noticed that only the SWCNTs on the perimeter of the bundle were supporting the load, with little load transfer to the inner tubes of the bundle. These observations were a result of their attachment method which gripped only the SWCNTs on the perimeter of the bundle. For energy storage, bundles are useful only if all of the inner tubes are equally loaded. For a bundle to display its true stiffness and strength under tension, all tubes must be gripped at the attachment site since the load transfer mechanism between tubes does not adequately distribute a load throughout the structure. It should be noted that the condition on the gripping method is relevant only for loading in torsion and tension since compression and bending will load all tubes within a bundle regardless of the attachment method. These observations suggest that it is indeed possible to achieve excellent stiffness and strength in continuous bundles. The shear modulus of bundles falls short of that of individual CNTs. Salvetat et al. measured a shear modulus of 1 GPa [21] and Lasjaunias et al. reported 1-2 GPa [63], considerably lower than 450 GPa for a SWCNT. The authors attributed their result to a shear modulus in bundles that is dominated by interactions between nanotubes rather than by the hexagonal lattice of an individual CNT.

Bundles of discontinuous CNTs are bundles in which the constituent tubes do not necessarily span the entire length of the bundle, as shown in Figure 2.6 [64, 65]. The bundle still maintains CNTs arranged in a hexagonal lattice, though vacancies may be present because of the discontinuous nature of the tubes [21]. The intercalated arrangement of tubes in the

bundle requires excellent load transfer between the tubes for the overall bundle to maintain high strength and stiffness. With weak shear interactions between tubes at the overlaps, slipping between the SWCNTs would be the principal failure mechanism. Ideally, van der Waals forces between the tubes could allow the CNTs in array to be loaded to the maximum loads of individual CNTs [64]. Yakobson et al. modeled such bundles and concluded that the length of the constituent SWCNTs should greater than 10 μm for the bundle to approach the strength of an individual SWCNT. Qian et al. estimated that contact lengths must be on the order of 10 to 120μm or greater for optimal load transfer [57]. If the results of Yakobson et al. and Qian et al. are correct, then macroscale bundles with this structure could be built with long lengths and large diameters and maintain excellent properties. The structure of bundles of discontinuous CNTs is similar to that of fibres, but improved fabrication techniques would be needed to obtain ideal bundle lattices with tight packing, high crystallinity, good load transfer and long overlaps between the tubes.

Figure 2.6: Diagram of a bundle of discontinuous CNTs where the length of individual CNTs is less than the length of the overall bundle [65].

Qian et al. report that twisting or weaving fibers can create a rope with better load transfer in tension than a grouping of straight fibers [8, 57], which applies equally to the twisting of CNTs in bundles. Twisting increases radial compression in a rope and friction between the fibers, resulting in improved load transfer with increased contact surface between the tubes. Better structural reliability is achieved because load is redistributed in case of the failure of one fiber. Consequently, CNT bundles with twisting between the tubes [8, 57] and helical geometries [66] are expected to be able to sustain higher loads in tension than straight bundles.

Irradiation has been proposed as a technique to improve the properties of CNT bundles. CNTs are strong because of their lattice of covalent bonds, but between SWCNTs in a bundle

there are only weak van der Waals forces. Exposure to irradiation can promote the formation of covalent bonds between SWCNTs in a bundle or even between shells in a MWCNT [64]. As long as the doses are sufficiently low that defects in the hexagonal lattice don't undermine the strength of individual CNTs, this technique has the potential to improve the strength and stiffness of bundles [67, 68].

Forests of CNTs are arrays of aligned, uniform SWCNTs or MWCNTs that grow vertically upward from a substrate. Synthesis is done using CVD on a silicon substrate patterned with catalyst. Forests can grow as high as 4 mm [69] with carbon purity as high as 99.98% [70]. The density of forests is relatively low, with a percentage of filled volume only on the order of 3% [56]. Advantages of CNT forests are their high degree of alignment and their large surface area, though forests tend to have high defect densities because of their fabrication using CVD at relatively low temperatures. With weak attachment between the forest and the substrate, forests can be easily removed from the substrate after they have been grown [70].

Once forests of CNTs have been synthesized, techniques have been proposed to densify forests into compact structures with densities approaching that of graphite. Liquid capillary forces are used to draw low density forests into densely packed "solids" of vertically aligned tubes with a density 20 times that of the original forest [56]. Applying a light pressure to a forest has a similar effect of causing the forest to collapse into a structure with a much higher density. The application of lateral forces creates compressed structures with vertical alignment, while shear forces can create flattened sheets which significantly improve upon the properties of mats due to their high degree of CNT alignment [56]. It is expected that with good alignment between the tubes and few defects in the CNTs, these compact structures should have excellent mechanical properties.

Macroscale assemblies must demonstrate exceptional properties to be selected as a material for super-springs. The objective is to group CNTs into a configuration so that a single applied deformation will load all individual CNTs within the grouping to their elastic limit, to maximize elastic strain energy density. The macroscale assembly must demonstrate strength and stiffness that approach the properties of individual CNTs. The grouping should have a mass density approaching the density of graphite. Forests show considerable promise as a starting

material for building super-springs because of the excellent alignment between the tubes and their millimeter lengths. The density of as-grown forests is too low, but compactifying techniques to increase their density show significant potential. Forests of CNTs can be used to build highly densified "solid" bundles of continuous CNTs a few millimeters long in which each CNT would span the length of the bundle, or dense sheets of CNTs with a high degree of internal CNT alignment. Forests could also be used as the starting material to fabricate bundles of discontinuous CNTs arranged into ideal structures as shown in Figure 2.6, with long overlaps between tubes and tight packing into hexagonal arrangements with inter-tube separation distances of 0.34 nm. Further work on assembling SWCNTs into macroscale structures is still needed to build and test materials that will be appropriate for the highest quality springs.

2.6. Attachment methods

Developing a reliable method of attaching CNTs to a surface is important for CNTs to be loaded to their elastic limit without inducing fracture at the attachment site. Attachment has previously been done by applying a soft acrylic adhesive to an AFM tip in an optical microscope [71], by applying a voltage between an AFM tip and a CNT to attach them using van der Waals forces [72], by direct CVD growth on an STM tip [73], and by deposition of SiO_2 over the ends of CNTs to rigidly attach them to a silicon substrate [74]. Attachment has also done by scanning an electron beam in a SEM at the attachment site between a CNT and an AFM tip. Dissociation of hydrocarbon gases in the chamber causes amorphous carbon to deposit at the joint, bonding the CNT to the AFM tip [20, 75]. Tensile tests performed by Yu et al. on MWCNTs attached to AFM tips using carbonaceous deposits showed that the attachment site is strong since in most cases the MWCNTs could be loaded and broken before the attachment site failed [20]. These encouraging results suggest that good attachment is indeed possible.

An important disadvantage of attachment using amorphous carbon deposits is that only the outer shell in the case of a single MWCNT and the outer, perimeter SWCNTs in the case of a SWCNT bundle come into contact with the carbon deposits, and consequently these are the only structures that are bonded to the surface [2, 20]. Little load transfer between tubes means that the inner shells of a MWCNT and the inner SWCNTs in a bundle will contribute little to

carrying an applied load. This has important implications for springs, in which even load transfer between all shells and all tubes is critical.

2.6.1. Design Recommendations

Due to the limitations of previously demonstrated attachment methods, several alternatives attachment techniques are proposed for loading CNTs in tension. If long bundles using the structure proposed by Yakobson et al. shown in Figure 2.6 can indeed be built with long overlaps between adjacent tubes and excellent load transfer, then the attachment methods shown in Figure 2.7 may be feasible. Figure 2.7 (a) shows a bundle wrapped around a post. Here, the attachment no longer relies on the strength of the attachment material or the attachment site but on the strength of the bundle itself, as long as a sufficiently sturdy post can be fabricated. Figure 2.7 (b) shows how a bundle can be secured around a post by tying knots [76]. The ability to tie knots has already been demonstrated in 30 μm diameter fibres [77]. Figure 2.7 (c) shows how splicing of individual CNTs within a bundle [76] can be used to create continuous structures with junctions for attachment purposes. These attachment methods rely on load transfer between tubes rather than on the strength of a single attachment site.

Another attachment design is proposed that makes use of friction and the capstan effect. Wrapping a rope around a shaft increases the load that can be carried because of friction between the rope and the shaft. The force required to carry a load decreases exponentially with the number of turns of the rope around the shaft, according to the relation $T_1 = T_2 e^{-\mu\theta}$, where T_2 is the force of a load, T_1 is the force required to carry the load, μ is the coefficient of friction between the rope and the shaft, and θ is the angle corresponding to the number of turns of the rope around the shaft, as shown in Figure 2.8 (a). One can take advantage of this effect to create a stronger attachment between CNTs and a surface. The CNTs are attached to the surface of the shaft using a conventional technique, such as a wetting epoxy that ensures that all tubes are firmly affixed to the surface. The CNTs are then wrapped around the shaft, as shown in Figure 2.8 (b). In this case, T_1 corresponds to the reaction force of the attachment site and T_2 corresponds to an applied tensile load. The applied load can be considerably larger than the reaction force of the attachment site because of the effect of friction along the contact

surface. For sufficiently long CNTs or bundles, this would be a useful technique to reinforce the attachment site and ensure that loading a CNT in tension is not limited by failure at the attachment site. Calculations based on this technique are limited by uncertainty in the value of the coefficient of friction between a CNT and a substrate surface, with reported values falling in the range of 0.01-0.09 [78, 79].

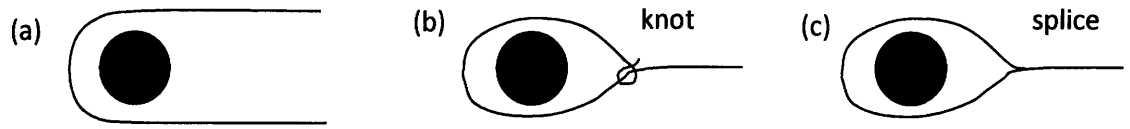

Figure 2.7: Alternative proposed methods for attachment.

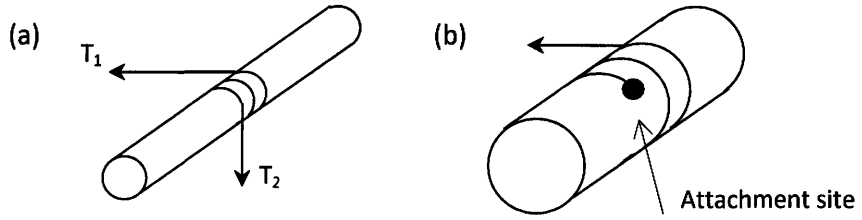

Figure 2.8: Attachment method using the capstan effect.

3. Energy storage estimates

Estimates of the energy that can be stored in springs made of carbon nanotubes under a mechanical deformation were used to evaluate the potential utility of this method of energy storage. First, simple estimates are presented of the total elastic strain energy and average energy density that can be stored in CNTs subject to four modes of mechanical deformation: axial tension, axial compression, pure bending and torsion. Advantages and disadvantages of each deformation mode are discussed. Once a CNT is deformed, a support structure is needed to carry the load of the spring prior to its discharge. The effects of support systems on the overall energy density of the spring system are presented next. Combined loadings are then presented to determine whether these deformations offer additional energy storage gains. Finally, implementation issues are addressed and the energy density estimates of CNT springs are compared to other common energy sources to evaluate whether energy storage in CNTs is worth further investigation.

Springs for energy storage would most likely be made of SWCNTs or MWCNTs arranged into dense bundles of long, aligned tubes. Energy density estimates will be generated for individual SWCNTs and MWCNTs as well as bundles of these structures.

When sufficiently large strains are applied to CNTs in torsion, bending and compression, they will buckle. Permanent defects to the atomic structure are more likely to form at these locations and buckling is a dominant failure mode [80]. In addition, buckling limits the total energy storage density so it is preferable to avoid applying strains to the mechanical springs above the buckling limit. Strain energy will only be calculated in SWCNTs and MWCNTs loaded up to their buckling point in compression, bending and torsion. Loading in tension will be up to the estimated failure strain.

To determine the pre-buckling mechanical behaviour of CNTs subject to external loads, CNTs are treated as linear elastic isotropic beams, with a thickness assigned to each CNT shell based on the continuum assumption [3, 25, 40]. The amount of energy that can be stored in mechanically deformed CNTs under reversible strains is estimated using this model. Each CNT layer is treated as a homogenous cylindrical shell, as shown in Figure 3.1. SWCNTs are assigned

an effective shell thickness of 0.34 nm, the distance between adjacent graphene sheets in graphite, and an effective Young's modulus of 1 TPa, the in-plane Young's modulus of graphite [2, 8, 81, 82]. The shell thickness of a MWCNT with n shells is $n \cdot 0.34$ nm. Treating a CNT as a beam is a simple model that does not account for the nested tube structure, the van der Waals forces, shear interactions between the layers, or non-linear post-buckling behaviour [13], but it provides reasonable strain energy density estimates. The calculations that follow rely on simple models of carbon nanotubes and make approximations about the behaviour of individual CNTs as well as CNTs grouped into bundles. However, the calculations provide a means of comparing the energy stored in different deformation modes and yield reasonable estimates of the order of magnitude of the energy density that is expected to be stored in these springs.

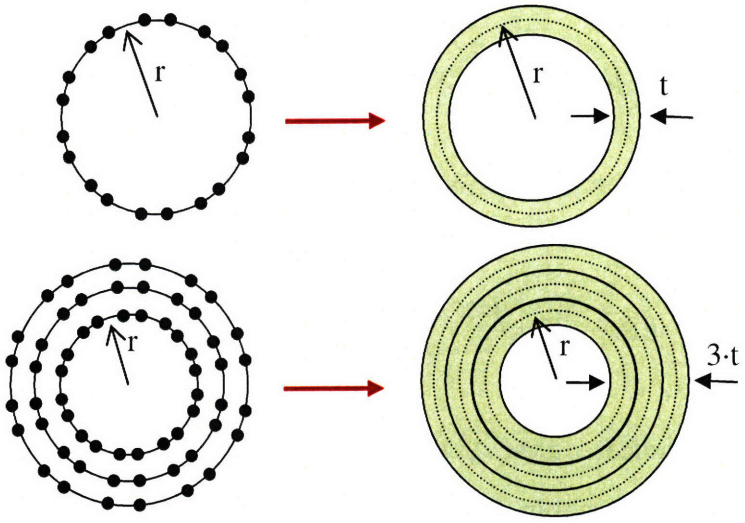

Figure 3.1: Equivalent continuum structure of SWCNT and MWCNT cross-sections, modeled as hollow cylindrical beams [83].

3.1. Axial tension

The equivalent continuum structure of a CNT of length L and diameter d under axial tension is shown in Figure 3.2. The hollow cylindrical tube has a thickness $n \cdot h$, where n is the number of layers in a CNT and h = 0.34nm is the thickness of one shell. For SWCNTs, n=1, and n is greater than 1 for MWCNTs. The tube has a mean radius r and diameter d, and a Young's modulus E.

The cylinder has inner and outer radii of $r_i = r - \frac{nh}{2}$ and $r_o = r + \frac{nh}{2}$. The cross-sectional area of the cylindrical tube is $A = \pi(r_0^2 - r_i^2)$ and the total enclosed area is $A_{encl} = \pi r_o^2$.

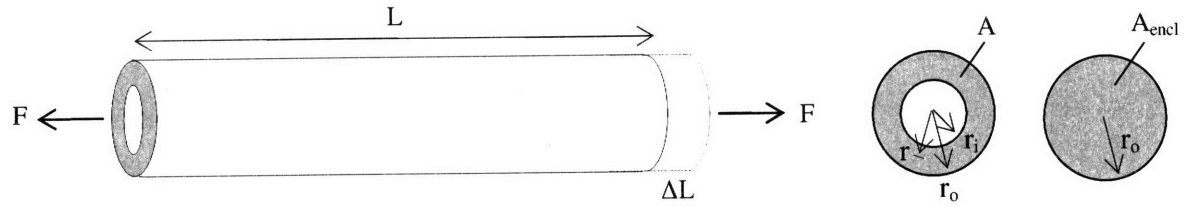

Figure 3.2: Equivalent continuum structure of a CNT with an applied load in axial tension.

Assuming that all shells are loaded equally, the strain energy of the axially loaded cylinder to an elastic strain of ε is

$$U = \frac{1}{2}\int\int\int(\sigma_x \varepsilon_x)dxdydz = \frac{1}{2}E\varepsilon^2 AL = \frac{1}{2}E\varepsilon^2\pi(r_o^2 - r_i^2)L \tag{3.1}$$

The strain energy density is the strain energy divided by the enclosed volume:

$$u = \frac{\frac{1}{2}E\varepsilon^2 AL}{A_{encl}L} = \frac{1}{2}E\varepsilon^2\frac{A}{A_{encl}} = \frac{E\varepsilon^2\pi(r_o^2 - r_i^2)}{2\pi r_0^2} = \frac{E\varepsilon^2\left[(r+\frac{nh}{2})^2 - (r-\frac{nh}{2})^2\right]}{2(r+\frac{nh}{2})^2} \tag{3.2}$$

The expression in (3.2) indicates that A/A_{encl} should be large for high energy density, so there should be little empty space within each CNT. Consequently, a spring in axial tension should consist of either SWCNTs with small diameters or uniformly-loaded MWCNTs with densely packed shells to maximize A/A_{encl}.

If CNTs are arranged in groupings, such as bundles, the strain energy density must be reduced by a fill factor k to account for the spacing between the individual CNTs in the grouped structure. For bundles of SWCNTs or MWCNTs under tension, the expression for energy density is rewritten as $u = \frac{1}{2}E\varepsilon^2 k\frac{A}{A_{encl}}$. Consider the cross-section of a bundle of closely-packed SWCNTs of radius r, arranged into a two-dimensional triangular lattice with a lattice constant of $2r+h$, as shown in Figure 3.3. Ideal packing is assumed with graphitic spacing of h=0.34 nm between the tubes [56], a bundle structure that has previously been observed experimentally

and studied using models [57, 62, 84]. It is assumed that MWCNTs are also arranged in similar bundle configurations, with spacing of 0.34 nm between adjacent MWCNTs.

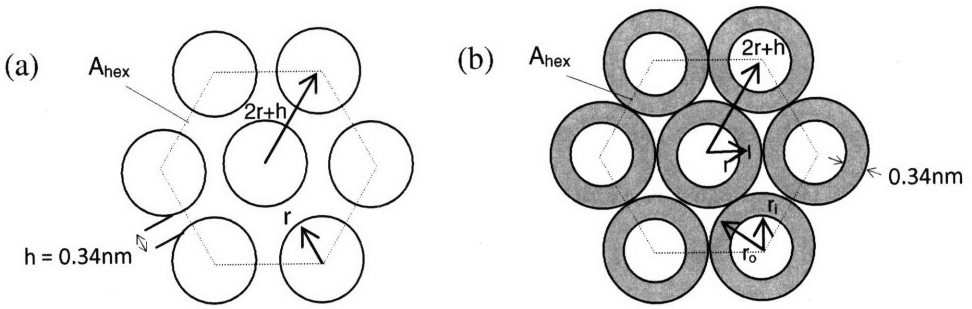

Figure 3.3: Geometry of the cross-section of a bundle of SWCNTs with a lattice constant of $2r+h$. The equivalent continuum structure is shown on the right.

The hexagonal shape shown as a dotted line in Figure 3.3 with an area of A_{hex} is taken to be the repeating geometrical unit in the bundle lattice. Then $k = \frac{3\pi r_o^{\,2}}{A_{hex}} = \frac{\pi\left(r+\frac{nh}{2}\right)^2}{\frac{\sqrt{3}}{2}(2r+nh)^2}$ = 91% and $\frac{A}{A_{encl}} = \frac{\pi r_o^{\,2} - \pi r_i^{\,2}}{\pi r_o^{\,2}}$, so a bundle cross-section consists of a fraction $k \cdot \frac{A}{A_{encl}}$ of CNT shells by area. Assuming that the cross section is uniform along its length, the bundle also consists of a fraction $k \cdot \frac{A}{A_{encl}}$ of solid CNT shells by volume. In reality, there may not be ideal packing within a bundle, so the actual fraction k may be lower than the values calculated here.

For example, a bundle of SWCNTs with diameter d=1.36 nm and ideal packing has $\frac{A}{A_{encl}}$=0.64 and k=0.91, so the fraction of the bundle filled with solid shells is $k \cdot \frac{A}{A_{encl}}$ = 58% by volume. The lattice constant is 1.7 nm. For a MWCNT with an outer shell diameter of 20 nm, ideal packing results in a bundle of MWCNTs with k=91%. The total fraction of the bundle filled with solid shells depends on $\frac{A}{A_{encl}}$, which is determined by the number of inner shells. For 10 inner shells

with r_o=10.17 nm and r_i=6.77 nm, this yields $\frac{A}{A_{encl}}$=0.56, so the fraction of the bundle filled with solid shells is $k \cdot \frac{A}{A_{encl}}$ = 51% by volume.

The expression for strain energy density in (3.2) shows that it is advantageous to apply high tensile strains to the springs to maximize energy storage since energy density is proportional to the square of strain. Energy density is plotted against strain for a 1.02 nm diameter SWCNT in Figure 3.4 to show the quadratic relation between energy density and strain. Indeed, tensile strains are not limited by buckling behaviour, so large elastic strains can be applied to the springs. Theoretical models predict that reversible tensile strains as high as 15%-30% [5, 20, 85] could be reached in CNTs, although strains at failure of only 6% for SWCNTs [1, 20, 85] and 12% for MWCNTs [20] have been demonstrated experimentally to date.

Figure 3.5 shows the strain energy density of SWCNTs in tension with applied strains of 5% and 15% as a function of diameter. Each graph plots the energy density for a single SWCNT with k=1, and a bundle of SWCNTs with ideal packing and k=0.91. Clearly, higher energy densities are achieved with larger applied strains. CNTs of low defect densities are critical to fabricating springs that can sustain high strains of up to 15% reversibly and without inducing failure. The plot also demonstrates that smaller diameter SWCNTs store energy more densely because of less unused space within the tubes. Bundles have slightly lower energy density than single SWCNTs because of the extra spacing between each tube.

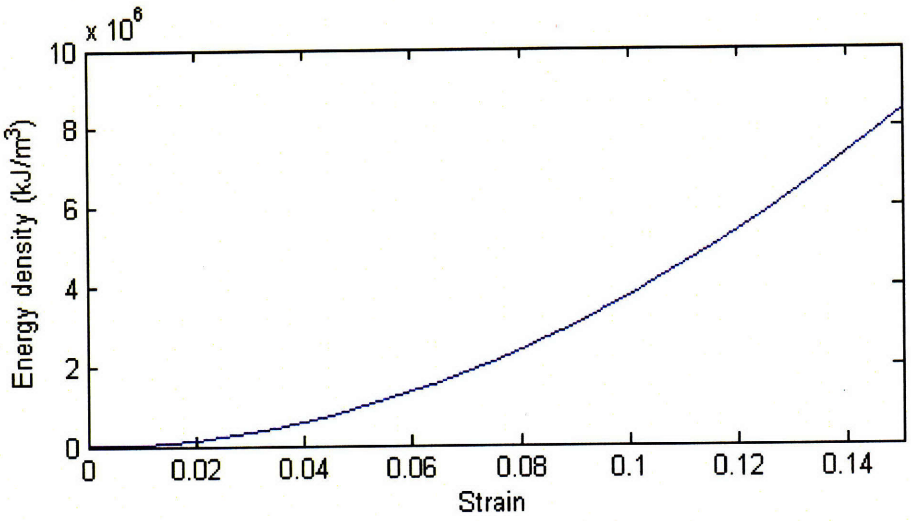

Figure 3.4: Energy density as a function of strain for a 1.02 nm diameter SWCNT.

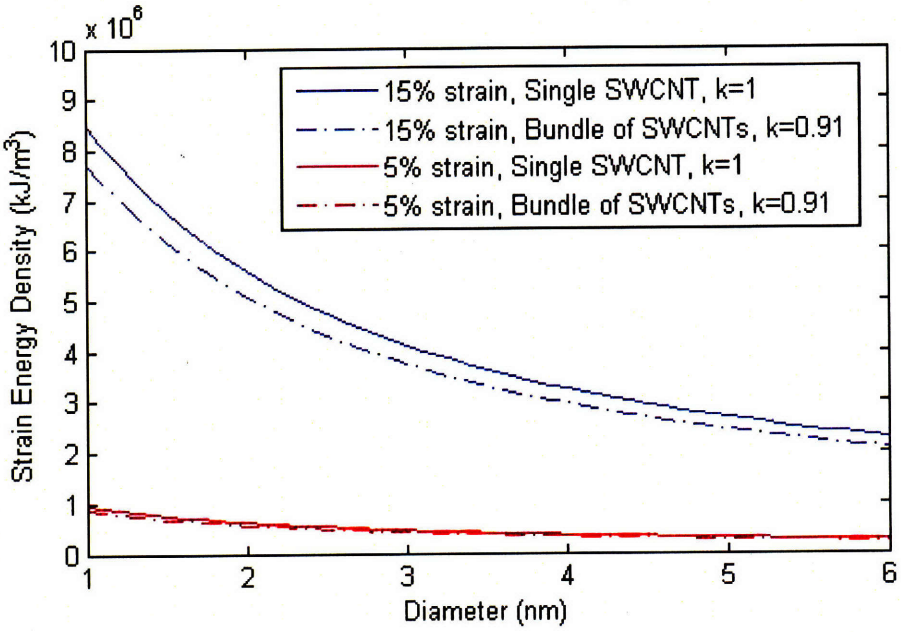

Figure 3.5: Strain energy density for SWCNTs as a function of diameter with applied strains of 5% and 15%, for individual SWCNTs with k=1 and ideally packed bundles with k=0.91.

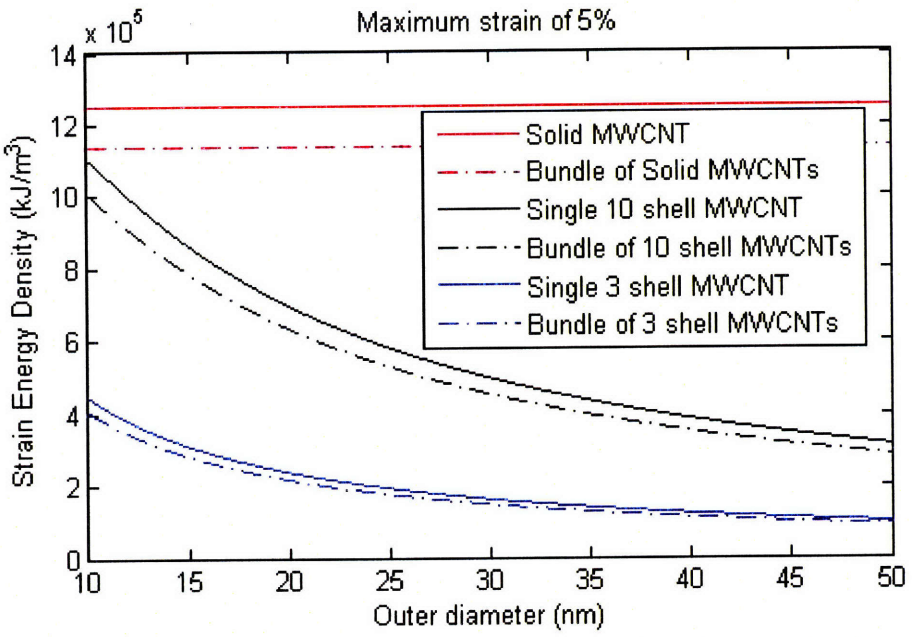

Figure 3.6: Plot comparing the strain energy density in MWCNTs as a function of outer diameter under an applied strain of 5%.

The graph in Figure 3.6 shows the strain energy density of MWCNTs as a function of outer diameter for nanotubes with 3 inner shells, 10 inner shells and solid shells, under an applied strain of 5%. Solid MWCNTs are considered as an approximation to the case of a very large number of shells. Ideal packing is assumed for MWCNTs, and k=0.91 is used for MWCNT bundles. The plot shows that higher energy density by volume can be reached in more densely packed MWCNTs because the greater number of nested inner shells reduces unused space inside the tubes. MWCNTs with nearly solid shells reach the maximum strain energy density, which becomes independent of the outer diameter. If the packing of MWCNTs in a bundle has spacing higher than the ideal inter-tube distance of 0.34nm, then the energy density of MWCNT bundles will be lower than what is shown in Figure 3.6.

An important challenge to the deformation of CNTs in tension is the difficulty of grasping the inner shells of a MWCNT. Tensile tests of MWCNTs attached to AFM tips at both ends show that fracture occurs at the outer shell by a sword-in-sheath mechanism, indicating loading of the outer shell and little load transfer to the inner shells [20, 57]. One effect is a lower stiffness and strength for MWCNTs than would be observed if all shells were equally loaded [57]. The results for strain energy density in Figure 3.6 assume that all shells of the MWCNTs are equally

loaded in axial tension, which may in fact not be the case. If the outer shell carries most of the load, then the strain energy density for MWCNTs will be significantly reduced. Unless a method of loading all shells equally in tension is developed, the inability to grasp the inner shells represents a significant limitation to storing energy by stretching MWCNTs. For that reason, bundles of SWCNTs are likely the better structure out of which to build springs that will be deformed in axial tension. Both the radial deformation of SWCNTs with larger diameter and the relationship between diameter and energy density suggest that bundles of SWCNTs with very small diameters would be the ideal structure for springs stretched in tension.

SWCNT ropes that have twisting between the tubes may be used instead of bundles. The tensile stiffness of ropes is expected to be similar to that of individual SWCNTs [21]. Ropes are more stable than loosely packed bundles and provide better load transfer and structural reliability because of the tighter packing of the tubes, as described in section 2.5. As a result, SWCNT ropes may have higher tensile strength than bundles and could be an excellent structure for springs in tension.

3.2. Axial compression

A similar analysis is performed on CNTs subject to compressive loads. A CNT is modeled as a hollow cylindrical beam of length *L*, Young's modulus *E*, and thickness *n·h*, where *n* is the number of layers in a CNT and *h* = 0.34 nm is the thickness of one shell, as shown in Figure 3.7. The continuum tube has a mean radius *r* and diameter *d*. The cylinder has inner and outer radii of $r_i = r - \frac{nh}{2}$ and $r_o = r + \frac{nh}{2}$. The shell's cross-sectional area is $A = \pi(r_0^2 - r_i^2)$ and the total enclosed area is $A_{encl} = \pi r_o^2$.

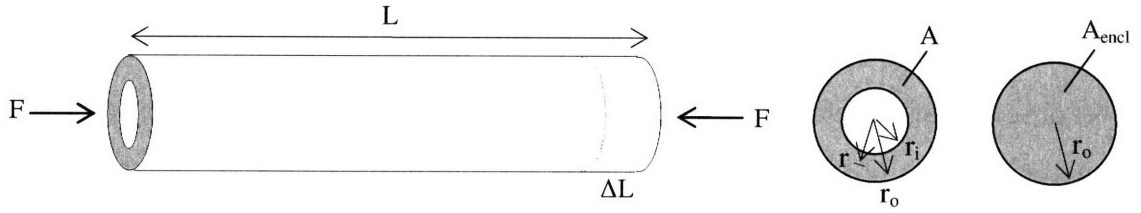

Figure 3.7: Equivalent continuum structure of a CNT with an applied load in axial compression.

The strain energy that can be stored in the bar under axial compression to a strain of ε is

$$U = \frac{1}{2}\int\int\int(\sigma_x\varepsilon_x)dxdydz = \frac{1}{2}E\varepsilon^2 AL = \frac{1}{2}E\varepsilon^2\pi\left(r_o^2 - r_i^2\right)L \tag{3.3}$$

The strain energy density is the strain energy divided by the enclosed volume:

$$u = \frac{\frac{1}{2}E\varepsilon^2 AL}{A_{encl}L} = \frac{1}{2}E\varepsilon^2\frac{A}{A_{encl}} = \frac{E\varepsilon^2\pi\left(r_o^2 - r_i^2\right)}{2\pi r_0^2} = \frac{E\varepsilon^2\left[(r+\frac{nh}{2})^2 - (r-\frac{nh}{2})^2\right]}{2(r+\frac{nh}{2})^2} \tag{3.4}$$

Once again, the strain energy density is reduced by a fill factor k to account for the spacing between the individual CNTs in groupings, and the energy density is rewritten as $u = \frac{1}{2}E\varepsilon^2 k\frac{A}{A_{encl}}$ for bundles. Just as in tension, high energy densities are achieved with a high A/A_{encl} ratio, so a spring in axial compression should consist of SWCNTs with small diameters or MWCNTs with densely packed shells.

It is advantageous to apply large strains to reach high energy densities since energy density is proportional to the square of the strain. To avoid buckling in the spring, the strain that can be applied to a CNT in compression is limited by the critical buckling strain in compression. Chang et al. used molecular mechanics to develop an expression for the critical buckling strain ε_{cr} of individual SWCNTs under compression [86]

$$\varepsilon_{cr} = \frac{4}{d}\sqrt{\frac{D_o}{Et}\left(1+\frac{t}{d}\right)}, \tag{3.5}$$

where d is the SWCNT diameter, t=0.339 nm is the effective wall thickness, D_o= 0.85 eV is the bending stiffness and Et = 360 J/m^2 is the in-plane stiffness of the SWCNT. The relation shows that SWCNTs with smaller diameters begin to buckle at higher strains. Higher buckling strains are advantageous for energy storage. Using molecular dynamics and the Tersoff-Brenner potential, Yakobson et al. developed another relation between the critical buckling strain and SWCNT diameter [22], $\varepsilon_{cr} = (0.077nm)d^{-1}$, where d is the tube diameter. Both relations for the critical buckling strain of SWCNTs are plotted against diameter in Figure 3.8, which shows good agreement between the two models.

Liew et al. used molecular dynamics to study the buckling behaviour of bundles of SWCNTs in compression [87, 88]. Their results showed that the van der Waals interactions between the tubes in a bundle were a strengthening mechanism which increased the critical buckling strain of the bundle by about 5% over the buckling strain of the individual SWCNTs.

Chang et al. found that the critical buckling strain for thick MWCNTs is insensitive to the inner diameter d_i and depends only on the outer diameter d_o, and proposed the relation $\varepsilon_{cr} = 0.0985nm/d_o$ [86]. Thick MWCNTs are defined as having a ratio of d_i/d_o less than 0.62. Critical buckling strain is plotted against outer diameter for thick MWCNTs in Figure 3.8 along with the critical buckling strain of SWCNTs. The plot shows that critical buckling strain decreases with the outer diameter of thick MWCNTs, similar to the trend of SWCNTs. Since thick MWCNTs generally have larger outer diameters than SWCNTs, MWCNTs will generally have lower critical buckling strains than SWCNTs.

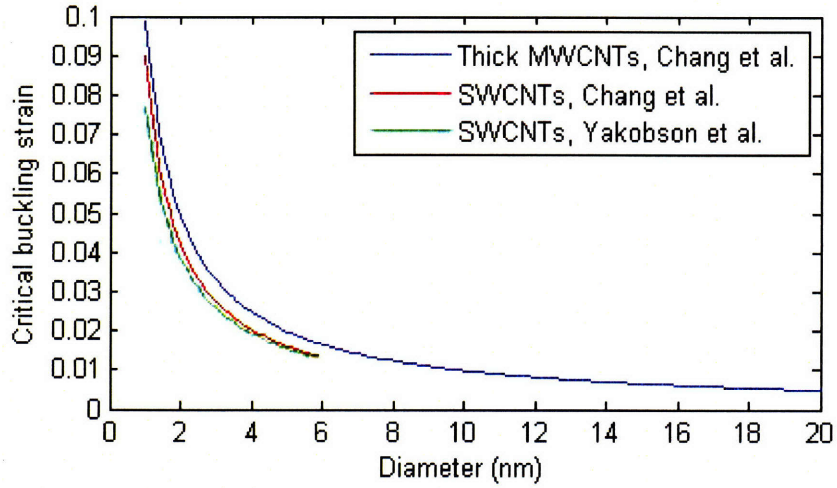

Figure 3.8: Critical compressive buckling strain plotted against diameter for SWCNTs and outer diameter for thick MWCNTs, using the models from Chang et al. [86] and Yakobson et al. [22].

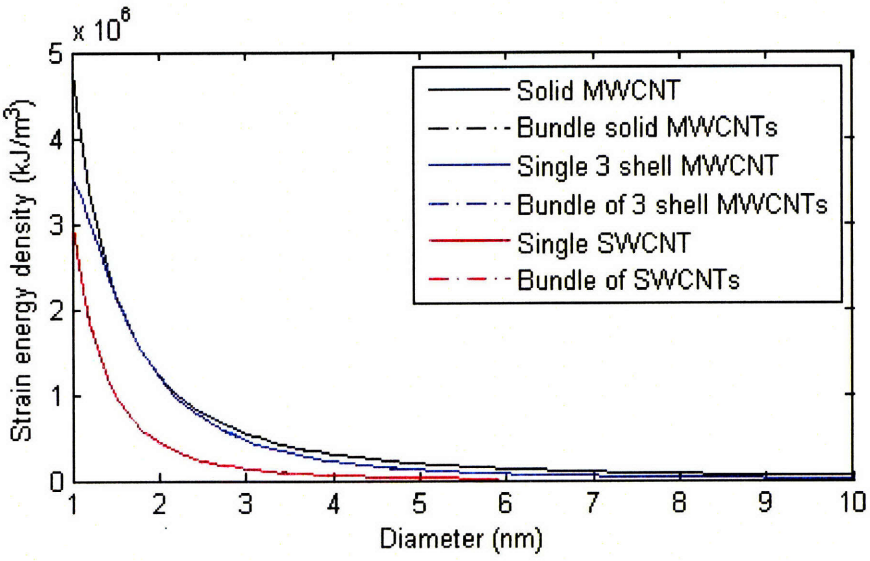

Figure 3.9: Maximum strain energy density plotted against diameter for SWCNTs, MWCNTs with 3 shells and solid MWCNTs, as well as bundles of these structures.

Strain energy density is plotted against tube diameter in Figure 3.9 for SWCNTs, MWCNTs with 3 shells and solid MWCNTs, along with bundles of each of these structures. For the purposes of this calculation, bundles of SWCNTs and MWCNTs are assigned a critical buckling strain 5% higher than their individual structure of the same diameter. The combination of higher critical buckling strain of bundles and lower packing density results in curves for the bundles that are nearly coincident with the curves of the individual structures. At low diameters, the strain energy density for compression is on the same order of magnitude as tension. Solid MWCNTs have higher energy density than thinner MWCNTs and SWCNTs for the same outer diameter because of their dense inner shells, but since SWCNTs generally have smaller diameters, their energy density will typically be higher. There is a more rapid decay in energy density as the diameter gets larger in compression than in tension because both empty space inside the tubes and critical buckling strain contribute to reducing the energy density. Strain energy density of solid MWCNTs is a function of diameter in compression, while it was independent of diameter in tension, because of the critical buckling strain. An important advantage of compression over tension is that it will affect all of the inner shells of a MWCNT. Consequently, deformation in compression would be better suited than tension for a spring

made of MWCNTs. However, overall, SWCNTs would be a better structure than MWCNTs for a spring in compression because their smaller diameters ensure high energy densities.

3.3. Bending

To estimate the strain energy of a carbon nanotube of diameter *d* in bending, an external moment *M* is applied to a hollow cylindrical beam of length *L*. The tube has a Young's modulus *E*, and thickness *n·h*, where *n* is the number of layers in a CNT and *h* = 0.34nm is the thickness of one shell, as shown in Figure 3.10. The tube has a mean diameter *d* and mean radius *r*, an inner $r_i = r - \frac{nh}{2}$ and an outer radius $r_o = r + \frac{nh}{2}$. The shell's cross-sectional area is $A = \pi(r_0^2 - r_i^2)$ and the total enclosed area is $A_{encl} = \pi r_o^2$.

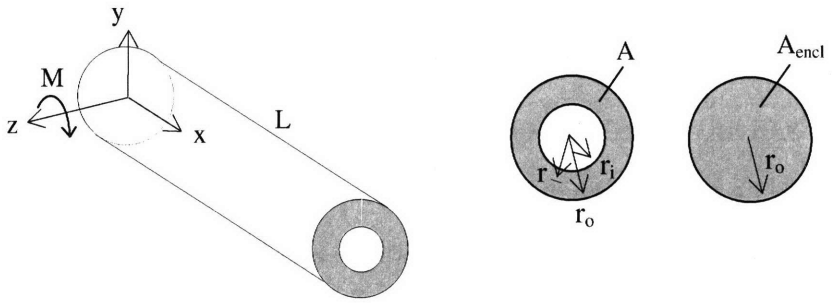

Figure 3.10: Equivalent continuum structure of a CNT in pure bending.

A moment *M* is applied about the z-axis, and the beam is bent to have a constant curvature. The axial strain in the beam is a linear function of the distance from the neutral axis along the y-axis, $\varepsilon_x = \frac{y}{r_o}\varepsilon$. The maximum strain of ±ε occurs at $y = \pm r_o$. The total strain energy of the beam is

$$U = \frac{E}{2}\iiint \varepsilon_x^{\,2}\,dxdydz = \frac{E\varepsilon^2 L}{2r_o^{\,2}}\iint y^2\,dydz = \frac{2E\varepsilon^2 L}{r_o^{\,2}}\int_{r=r_i}^{r=r_o}\int_{\theta=0}^{\theta=\pi/2} r^3(\sin\theta)^2\,d\theta dr$$

$$= \frac{1}{8}E\varepsilon^2 L\pi\frac{(r_o^{\,4} - r_i^{\,4})}{r_o^{\,2}} = \frac{1}{8}E\varepsilon^2 A_{encl} L\left[1 - \left(\frac{r_i}{r_o}\right)^4\right] \qquad (3.6)$$

The strain energy density is the strain energy divided by the enclosed volume:

$$u = \frac{\frac{1}{8} E\varepsilon^2 A_{encl} L\left[1-\left(\frac{r_i}{r_o}\right)^4\right]}{A_{encl} L} = \frac{1}{8} E\varepsilon^2\left[1-\left(\frac{r_i}{r_o}\right)^4\right] \quad (3.7)$$

The expression above indicates that high energy density can be reached when the ratio of inner to outer diameter, r_i/r_o, of the CNT is small, which implies that the highest energy densities are achieved in SWCNTs with small outer diameters or in MWCNTs with densely packed shells.

For SWCNTs or MWCNTs arranged into bundles, k represents the fraction of the grouping volume filled with CNTs, and the energy density of bundles is rewritten as $u = \frac{1}{8} E\varepsilon_o^2 k\left[1-\left(\frac{r_i}{r_o}\right)^4\right]$. This expression makes the assumption that when bending is applied to a bundle, individual CNTs in a grouping can slide against neighbouring tubes so that each CNT in the grouping develops a strain gradient of $-\varepsilon$ to ε.

The amount of bending that can be applied to a CNT is limited by the strain at which a CNT begins to buckle. In bending, buckling occurs along the compressed inner surface of the curved tube. Yakobson et al. modeled the critical buckling strain of a SWCNT under bending as $\varepsilon_{cr} = (0.077nm)d^{-1}$ [22], where d is the SWCNT diameter. In the continuum model, buckling occurs when the strain at the inner edge of the tube reaches ε_{cr}, so the critical radius of curvature at buckling of a SWCNT is approximated as $\rho_{cr} = d^2/0.155nm$. Chang et al. modeled the critical buckling strain of thick MWCNTs in bending as $\varepsilon_{cr} = \frac{0.111nm}{(d_o + t)}$, where d_o is the outer diameter and t=0.34 nm is the interlayer spacing [86]. The corresponding critical radius of curvature is $\rho_{cr} = \frac{d_o(d_o+t)}{0.222nm}$. These two expressions for critical buckling strain are plotted against diameter for SWCNTs and thick MWCNTs in Figure 3.11, showing an inverse relation between buckling strain and diameter. As in compression, deforming a CNT in pure bending has the advantage of deforming all shells of a MWCNT.

Few studies have compared the critical buckling strain in bending of individual SWCNTs to SWCNT bundles. For the purposes of these calculations, it is assumed that SWCNTs and

MWCNTs in groupings can slide amongst neighbouring tubes due to the weak interaction forces [68] so the buckling strain in bending of a grouping is the same as that of the individual tubes, although this may not necessarily be the case in practice.

The critical radius of curvature of SWCNTs is plotted against diameter in Figure 3.12. An important observation is that the critical radius of curvature is in the sub-micron range. If the assumption that CNTs within a bundle can slip with respect to each other is correct, then a bundle in bending must reach the critical radius of curvature of a single CNT to achieve the highest energy density. If CNTs are assembled into bundles with diameters on the order of microns, then applying such a small radius of curvature may be difficult. In that case, bending may not be the most practical mode of deformation for bundles.

Strain energy density as a function of diameter is plotted in Figure 3.13. The graph indicates that energy density decreases rapidly with diameter because of the limit on the applied strain due to buckling. For the same outer diameter, MWCNTs store energy with higher density than SWCNTs because of the dense packing of inner shells. However, SWCNTs generally have smaller diameters than MWCNTs so SWCNTs will tend to store energy with higher density. Consequently, SWCNTs with small diameters, less than 1-2nm, would be the best structure for a spring deformed in bending.

The strain energy density of CNTs in bending at small diameters is somewhat lower than in compression and tension. This is explained in part because of lower critical buckling strains. Another reason for lower energy density is that tension and compression load the whole structure to a uniform stress, while bending induces a stress gradient in the continuum structure so that the maximum stress is reached only at the outermost layer.

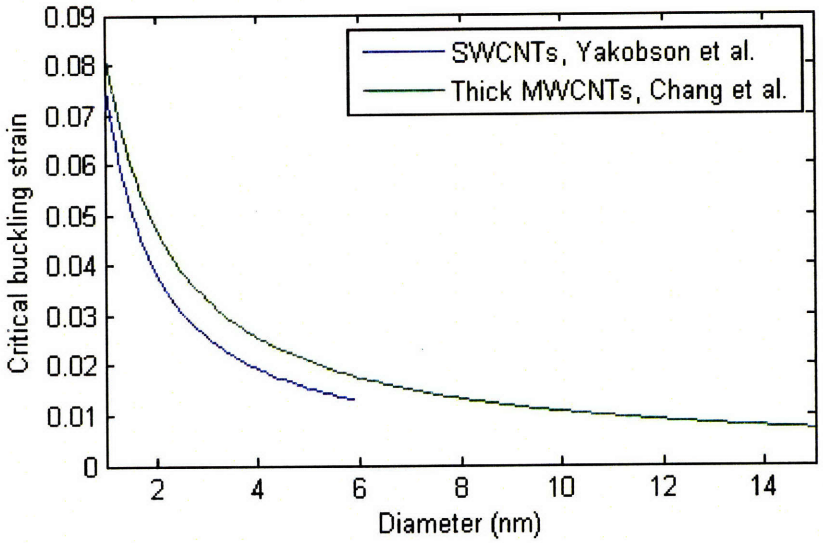

Figure 3.11: Critical buckling strain for SWCNTs and thick MWCNTs

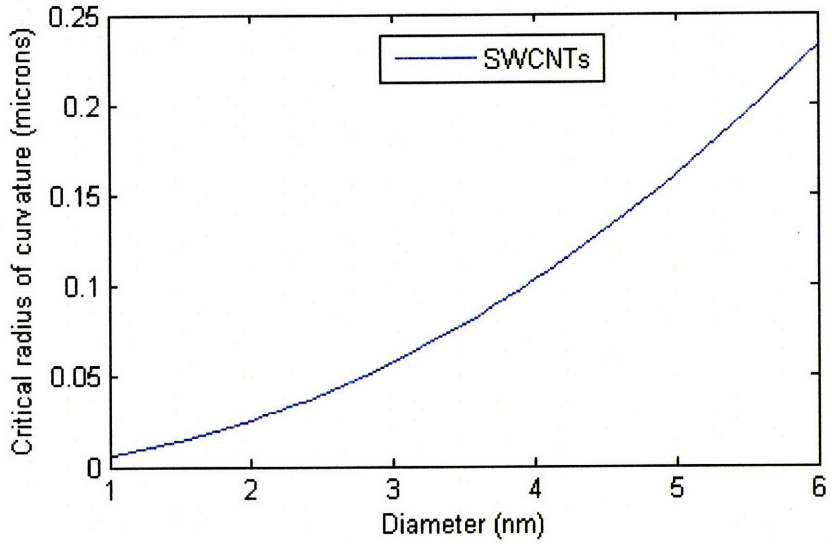

Figure 3.12: Critical radius of curvature for SWCNTs as a function of diameter.

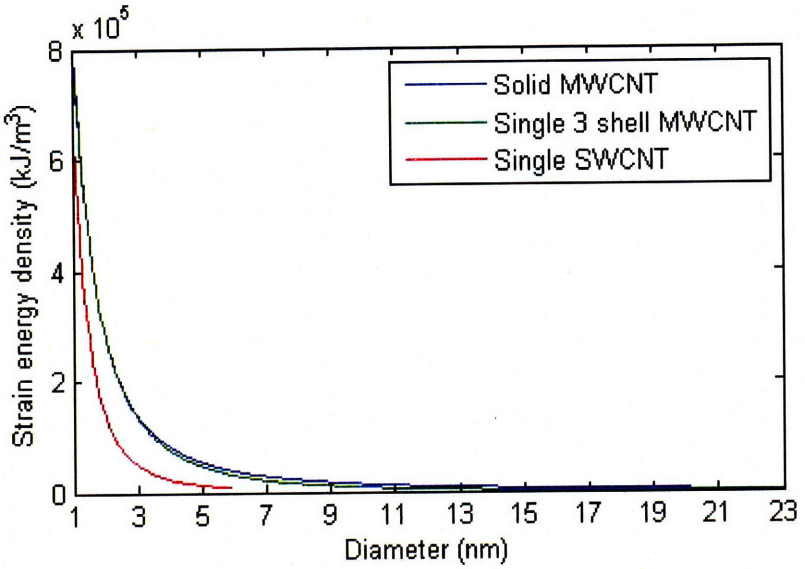

Figure 3.13: Strain energy density as a function of diameter for SWCNTs and outer diameter for MWCNTs with 3 shells and solid shells.

3.4. Torsion

To estimate the strain energy of a CNT under torsion, a moment *M* is applied to a hollow cylindrical tube with a uniform cross-section. For a CNT of length *L*, diameter *d*, radius *r* and shear modulus *G*, the equivalent continuum structure has a thickness *n·h*, where *n* is the number of layers in a CNT and *h* = 0.34nm is the thickness of one shell, as shown in Figure 3.14. The moment is applied about the *x*-axis. The mean radius and diameter of the tube are *r* and *d*, and the cylinder has an inner and outer radius of $r_i = r - \frac{nh}{2}$ and $r_o = r + \frac{nh}{2}$. The polar moment of inertia of the tube is $J = \frac{\pi}{2}({r_o}^4 - {r_i}^4) = \frac{\pi}{2}\left((r + \frac{nh}{2})^4 - (r - \frac{nh}{2})^4\right)$. The shell cross-sectional area is $A = \pi(r_0^2 - r_i^2)$ and the total enclosed area is $A_{encl} = \pi r_o^2$.

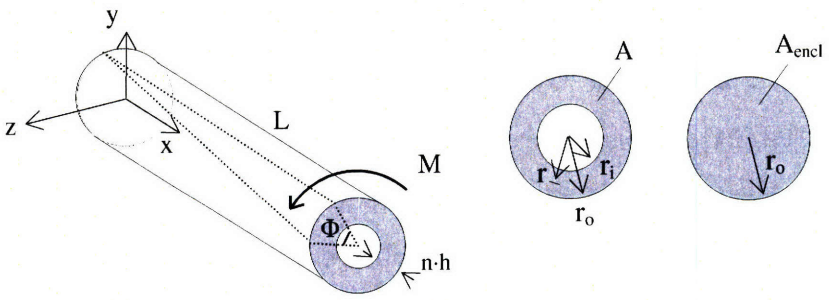

Figure 3.14: Equivalent continuum structure of a CNT under torsion.

The beam is fixed at one end and the torsional moment M is applied to the other end. The maximum stress at the outer edge is τ_{max}. The elastic strain energy is

$$U = \int_V \frac{\tau^2}{2G} dV = \int_A \frac{L}{2G}\left(\frac{Mr}{J}\right)^2 dA = \frac{M^2 L}{2GJ^2}\int_{r_i}^{r_o} r^2 2\pi r dr = \frac{M^2 L}{2GJ^2}\frac{\pi}{2}(r_o^4 - r_i^4) = \frac{M^2 L}{2GJ} \quad (3.8)$$

The strain energy density is the strain energy divided by the enclosed volume:

$$u = \frac{M^2 L}{2GJA_{encl}L} = \frac{M^2}{2GJ\pi r_o^2} = \frac{1}{4G}\tau_{max}^2 \frac{(r_o^4 - r_i^4)}{r_o^4} \quad (3.9)$$

The failure mode for a tube in torsion is buckling since the circular cross-section of a carbon nanotube collapses once a certain torsion angle is applied [27]. Buckling occurs when the maximum shear stress at the outer surface of the tube reaches a critical shear stress τ_{cr}. To avoid buckling in the energy storing spring, the shear stress developed in the continuum structure should not exceed the critical shear stress. To find the maximum strain energy density that can be stored in the structure, a critical moment M_{cr} should be applied so that the stress at the outer surface of the tube is equal to the critical shear stress, $\tau_{cr} = \frac{M_{cr} r_o}{J}$. The critical shear strain γ_{cr} is then given by $\gamma_{cr} = \frac{M_{cr} r_o}{GJ}$.

The critical shear strain of a CNT has been shown to depend on the length, diameter, chirality, direction of loading and number of shells in a MWCNT [89, 90]. Wang et al. [23] propose a simpler model for the critical moment of long SWCNTs or MWCNTs based on a classical formula from Timoshenko and Gere [91] for the critical moment of long shells:

$$M_{cr} = \frac{4EJ}{d}\sqrt[4]{\frac{1}{3}\left(\frac{4D}{Ehd^2}\right)^3} \quad (3.10)$$

where d is the mean diameter of the tube, E is the Young's modulus, J is the polar moment of inertia of the tube's cross-section, h is the thickness of the tube, $D = \frac{Eh^3}{12(1-\nu^2)}$ is the bending rigidity of the cylinder, and ν is the Poisson's ratio. Wang et al. suggest the parameters h=0.076 nm for a single shell and E= 5.11 TPa [91]. A Poisson's ratio of ν= 0.21 [82] and a shear modulus of G=450 GPa are also used in the calculations that follow. Critical shear strain is plotted against diameter d for SWCNTs in Figure 3.15. Superposed on the graph are data points reported by Chang [89] for critical buckling shear strain using molecular dynamics simulations. The difference between the two curves suggests that the simple relation by Wang et al. may

overestimate the buckling strain at low diameters, which will in turn cause the strain energy density to be overestimated. Both results show that critical shear strain decreases with diameter.

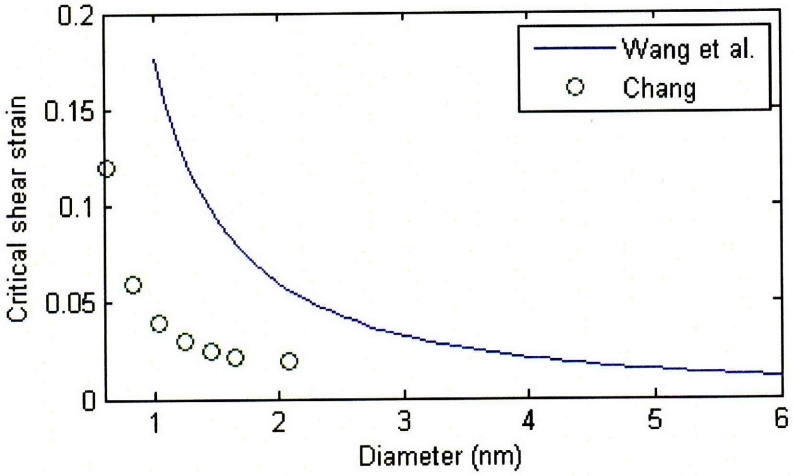

Figure 3.15: Critical shear strain for a SWCNT plotted against diameter *d* using the model from Wang et al. [23]. Superposed on the graph are the data points for critical buckling shear strain as reported by Chang [89].

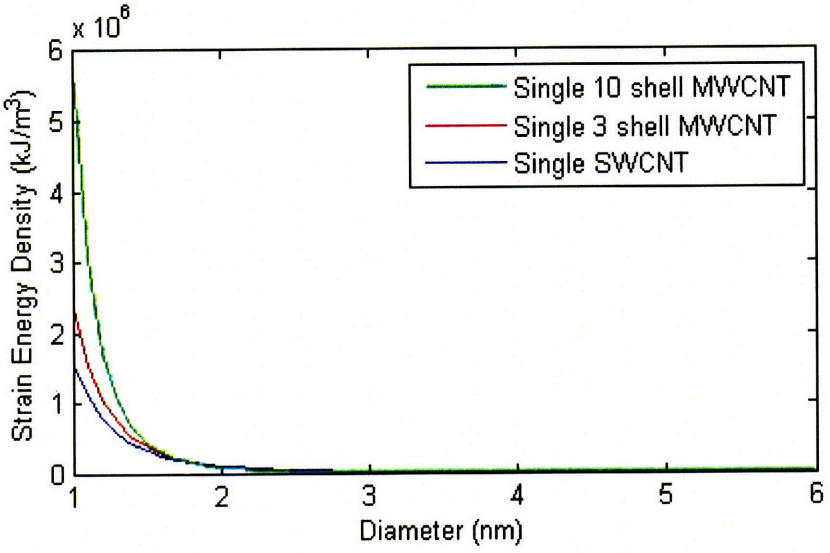

Figure 3.16: Strain energy density as a function of outer diameter for SWCNTs and MWCNTs with 3 and 10 shells.

The strain energy density of a SWCNT and a MWCNT with 3 and 10 shells is plotted against diameter in Figure 3.16 using the buckling strain model of Wang et al. [23]. This graph shows

that higher energy density is achieved with small diameters, and energy density decreases rapidly with diameter. For MWCNTs, it is assumed that all shells are equally affected by an applied moment, not just the outer shell, which may not necessarily be the case since it is challenging to grasp the inner shells [20]. MWCNTs have higher energy density than SWCNTs for the same outer diameter because of their dense inner shells. Indeed, Wang et al. [92] used a multiple-elastic shell model to study the torsional buckling of MWCNTs, assuming that all shells are equally affected by the applied moment, and observed that nearly solid MWCNTs with dense layers of shells can support higher torsional loading and have higher critical shear stresses than MWCNTs with fewer shells. If MWCNTs are used for energy storage, then they should have small diameters and densely packed inner shells. It is important to note, however, that the energy density advantage of MWCNTs is lost if all shells are not equally supporting the torsional load.

In general, SWCNTs will have a higher energy density than MWCNTs because of their smaller outer diameters. For energy storage in pure torsion, the plot in Figure 3.16 demonstrates that the highest energy densities are achieved in SWCNTs with small outer diameters of less than 2 nm.

3.5. Comparison of deformation modes

The previous sections have shown that there are advantages and disadvantages to each deformation mode and type of CNT structure. Deforming MWCNTs in axial tension or torsion comes with the challenge of grasping the inner shells, while compression and bending ensure that loading is applied to all inner shells. Torsion, bending and compression are limited by critical buckling stresses, while tension is limited only by the stress at which failure occurs. Energy density is highly dependent on the diameter of the nanotubes. MWCNTs with densely packed shells and SWCNTs with small diameters can reach the highest energy densities. For all loadings, the best performance is displayed by SWCNTs with diameters of 1 nm or smaller. Since SWCNTs naturally occur in bundles, densely packed bundles of SWCNTs would be an ideal structure for CNT-based springs.

Strain energy density in bundles of SWCNTs for all four deformation modes as a function of diameter is plotted in Figure 3.17. The energy density in units of kJ/kg is plotted on the graph in Figure 3.18. To convert the energy density from units of kJ/m^3 into units of kJ/kg, the density of the spring structure is needed. The density of a bundle of SWCNTs is estimated by multiplying the density of graphite, 2200 kg/m^3, by $k \cdot \frac{A}{A_{encl}}$ to account for empty space inside the CNTs and within the groupings.

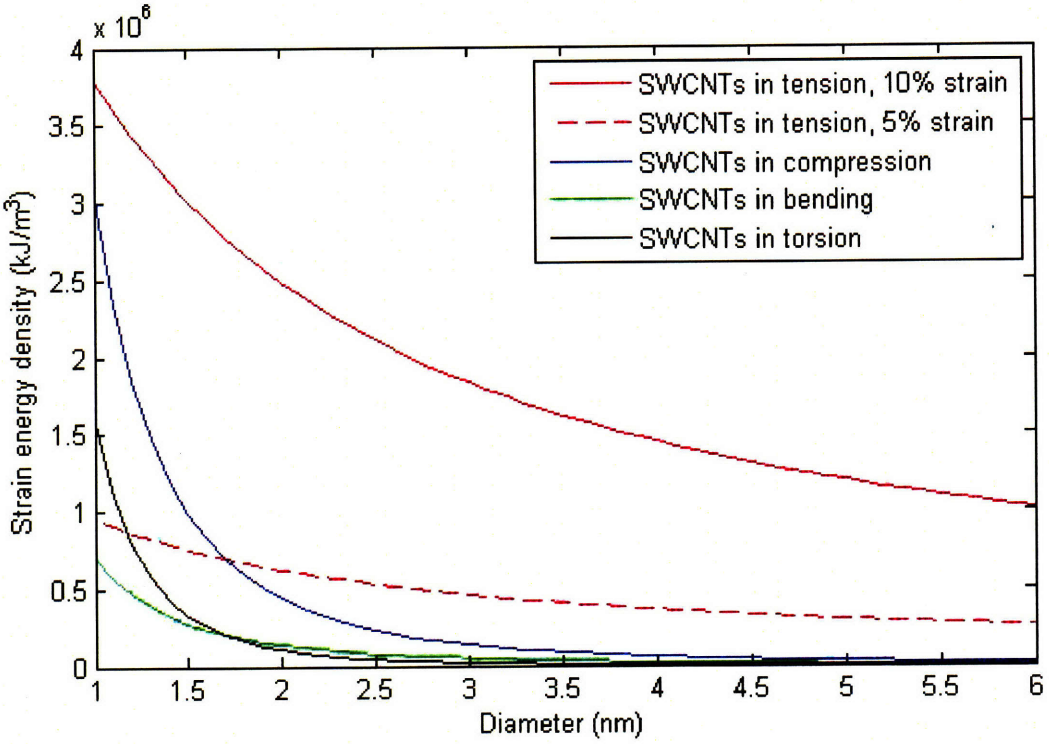

Figure 3.17: Strain energy density of SWCNT bundles as a function of diameter for four deformation modes in units of kJ/m^3.

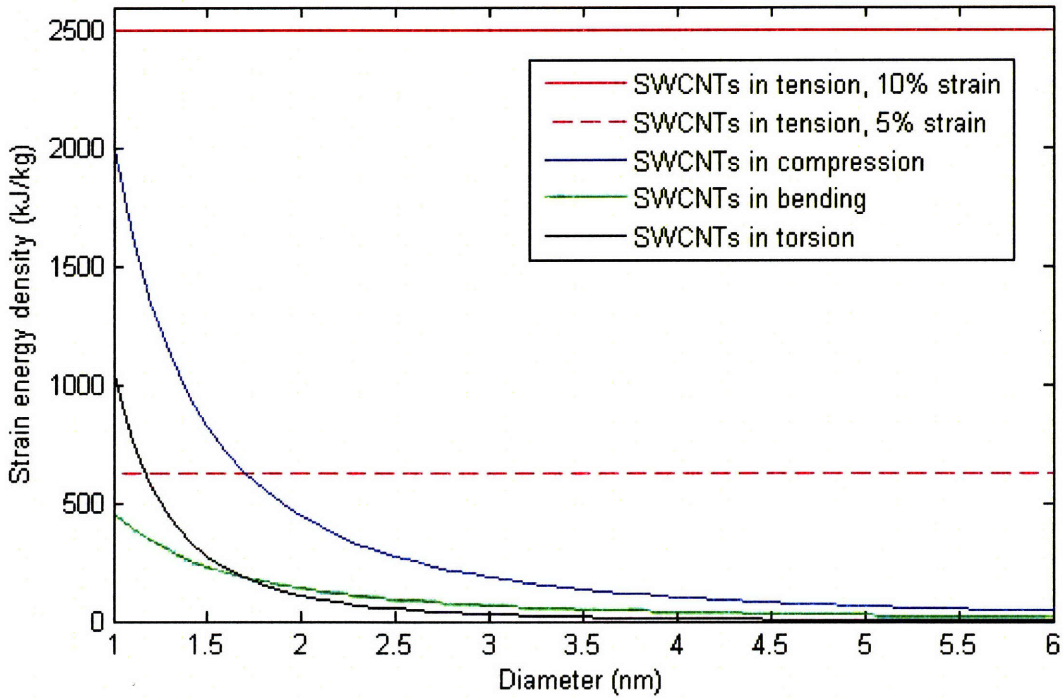

Figure 3.18: Strain energy density of SWCNT bundles as a function of diameter for four deformation modes in units of kJ/kg.

The plot in Figure 3.17 shows that there are advantages to storing energy in tension rather than compression, bending or torsion. This is particularly the case for SWCNTs with diameters greater than 2 nm since energy density drops off rapidly in compression, bending, and torsion because of the limits on applied strain due to buckling. For diameters smaller than 2 nm, the energy densities of all deformation modes are in the same range, so any of the deformation modes could be selected for a spring. Nevertheless, if strains of 10% or greater can be applied to CNTs in tension before failure, then tension would be the best choice. A distinction between Figure 3.17 and Figure 3.18 is that energy density in tension is no longer a function of diameter when the units are in kJ/kg because energy density decreases only due to limits on the applied strain and not due to empty space within the tubes. If energy per unit mass is the quantity of interest rather than energy per unit volume, then tension would be the deformation mode of choice for SWCNTs of any diameter, assuming large applied strains. All of these results confirm that a good choice for a spring would be a dense bundle of SWCNTs with diameters less than 2 nm, stretched in tension.

3.6. Coupling of deformation modes

The previous calculations show that considerable energy can be stored in CNTs under pure axial tension, compression, torsion and bending. The next step is to determine whether combined loadings offer any additional energy storage gains. Simple models are adopted to study energy density under coupled loadings.

For instance, energy can be stored in CNTs under combined stretching and twisting, stretching and bending, or compression and bending. Twisting, stretching and bending can all be combined by placing a bundle of CNTs between two supports and rotating one of the supports with respect to the other. In some cases, deforming CNTs with combined loading may simply be more convenient than one deformation mode alone. For instance, wrapping a stretched CNT around a support shaft, which combines bending and stretching, is a more compact way of storing energy than stretching a long CNT in pure axial tension.

Mohr's failure criterion is used to predict the failure of a CNT under combined loadings, with failure assumed to occur when the principal stresses at a point are greater than either the compressive buckling stress or tensile failure stress. The diagrams in Figure 3.19 show the allowable principal stresses and the failure boundary for normal and shear stresses in σ-τ space. In reality, CNTs are anisotropic and their complex failure modes depend on geometry, chirality, temperature, loading and defects [93], but this simple model can be used to generate order of magnitude energy density estimates. The ultimate tensile stress σ_t can range roughly between 50 GPa to 100 GPa, corresponding to maximum strains of 5% to 10% using a Young's modulus of 1 TPa. The relation developed by Yakobson et al. [22] is used to find the critical compressive buckling stress σ_C.

Wang et al. modeled MWCNTs under combined torsional and axial loading using a multiple shell model and found that the critical shear stress at which buckling first occurs in axial tension and torsion is higher than the critical shear stress of torsion and axial compression [90]. His results also showed that applying tension makes MWCNTs resist higher torsional loads. As long as the limiting compressive stress is smaller than the limiting tensile stress, these same results can be observed from Figure 3.19.

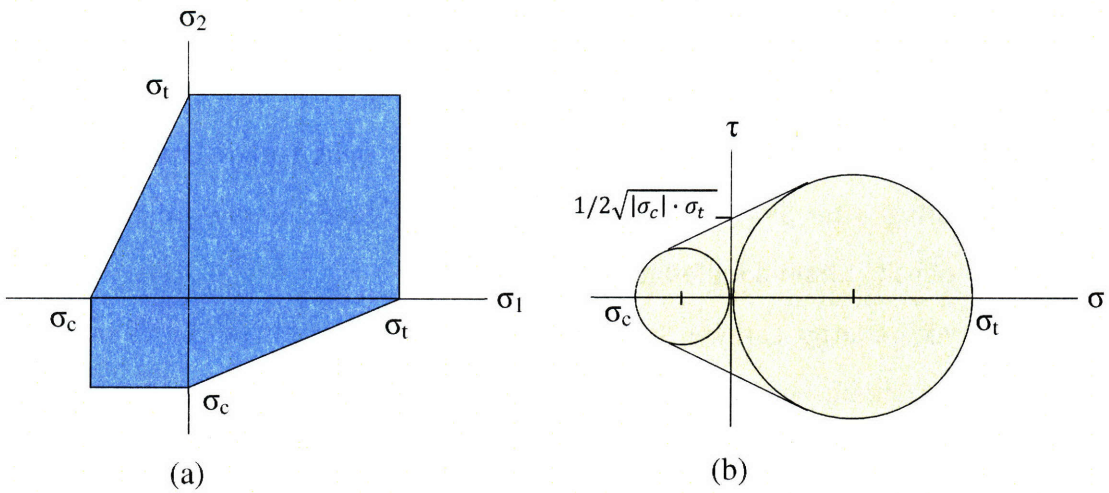

Figure 3.19: (a) Allowable principal stresses in the structure. (b) Allowable boundary for shear and normal stresses in σ-τ space.

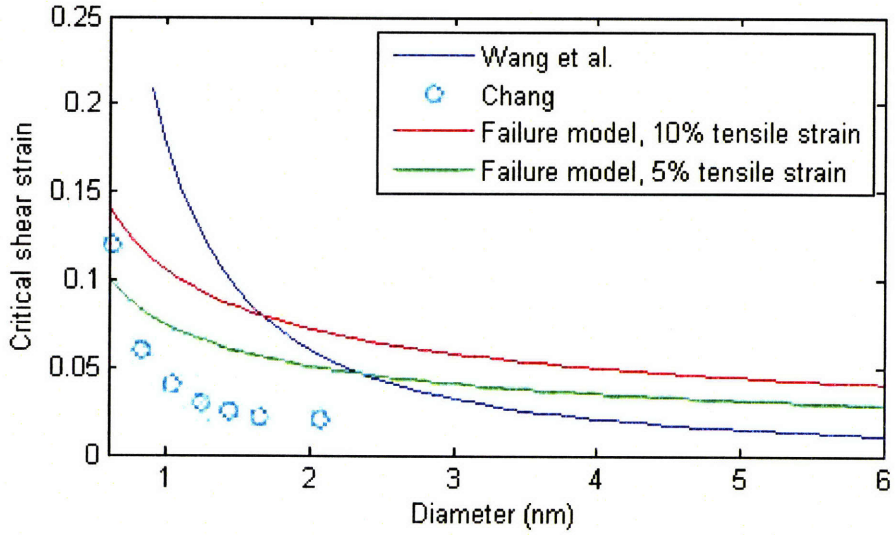

Figure 3.20: Predictions for critical shear strain of SWCNTs from the failure model are plotted along with the model from Wang et al. [23] and the data from Chang [89].

This model will accurately predict failure in pure compression and pure tension, so the next step is to evaluate the model by determining how well it predicts failure in pure torsion. If the limiting compressive stress is σ_C and the limiting tensile stress is σ_t, then the maximum pure shear stress that can be applied is $\frac{1}{2}\sqrt{|\sigma_c| \cdot \sigma_t}$ and the maximum shear strain is $\frac{1}{2G}\sqrt{|\sigma_c| \cdot \sigma_t}$. The critical shear strains for SWCNTs predicted by the failure model are plotted with the previous results of Figure 3.15 and are shown in Figure 3.20. The critical shear strain is plotted

using maximum tensile strains of both 5% and 10% and maximum compressive strains based on the relation from Yakobson et al., $\varepsilon_{cr} = (0.077nm)d^{-1}$ [22]. The graph shows that at small diameters, the curve for the predicted critical shear strain lies between the curves from Wang et al. [23] and the data from Chang [89], so it is assumed that critical shear strain is reasonably well predicted by the failure model for SWCNTs with small diameters, given a certain amount of uncertainty in all of the models.

Cylindrical coordinates r, θ, z are considered here, where z is the axial direction along the length of the CNT. The state of stress on an element under any combination of tension, compression or bending is shown in Figure 3.21 (a). Each of these deformation modes contributes only to σ_{zz}, so there is no energy gain in combining them. The state of stress from combining any of tension, compression or bending with torsion is shown in Figure 3.21 (b). Tension, bending and compression all contribute to σ_{zz}, while torsion contributes to $\tau_{z\theta}$, so there can be a gain from combining torsion with another deformation mode. It is important to note that this analysis focuses on a single CNT since pure torsion, without any bending, is difficult to apply to CNTs within a grouping. Radial compression due to interactions between neighbouring CNTs is neglected in the calculations.

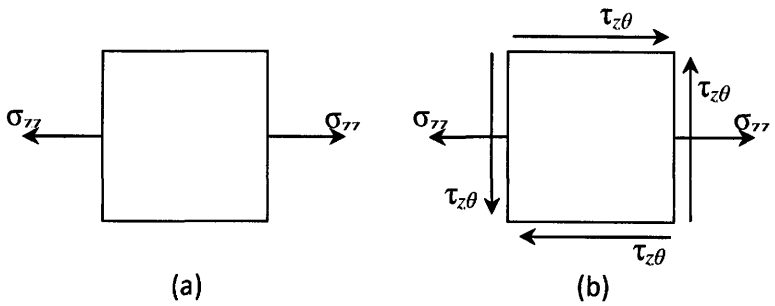

Figure 3.21: States of stress under combined loadings for (a) a combination of tension, compression or bending and (b) combining torsion with any of tension, compression or bending.

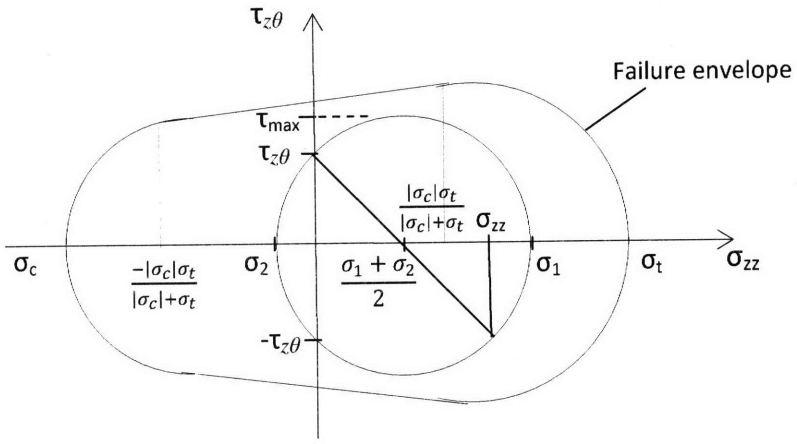

Figure 3.22: State of stress in the structure subject to a tensile stress σ_{zz} and a shear stress $\tau_{z\vartheta}$.

The strain energy density of a body under a general state of stress is

$$u = \frac{1}{V}\int_V \left[\frac{1}{2}\sigma_{zz}\epsilon_{zz} + \frac{1}{2}\sigma_{rr}\epsilon_{rr} + \frac{1}{2}\sigma_{\theta\theta}\epsilon_{\theta\theta} + \frac{1}{2}\tau_{rz}\gamma_{rz} + \frac{1}{2}\tau_{z\theta}\gamma_{z\theta} + \frac{1}{2}\tau_{r\theta}\gamma_{r\theta}\right] dV \quad (3.11)$$

If only stresses σ_{zz} and $\tau_{z\vartheta}$ are applied,

$$u = \frac{1}{V}\int_V \left[\frac{1}{2E}\sigma_{zz}^2 + \frac{1}{2G}\tau_{z\theta}^2\right] dV \quad (3.12)$$

Let $\tau_{z\vartheta,out}$ be the maximum shear stress at the outer surface of the cylinder. Using the continuum model of a CNT, the integral is evaluated and the energy density is rewritten as

$$u = \frac{1}{\pi r_o^2}\left[\int_{r_i}^{r_o}\frac{1}{2E}\sigma_{zz}^2 2\pi r dr + \int_{r_i}^{r_o}\frac{1}{2G}\frac{\tau_{z\theta,out}^2 r^2}{r_o^2}2\pi r dr\right]$$
$$= \frac{1}{2E}\sigma_{zz}^2\frac{r_o^2 - r_i^2}{r_o^2} + \frac{1}{4G}\tau_{z\theta,out}^2\frac{r_o^4 - r_i^4}{r_o^4} \quad (3.13)$$

While treating the strain energy density as a linear sum of the strain energies from the individual deformations is an approximation, Sears et al. used molecular dynamics models to show that this linear approximation is reasonable [82].

Finding the maximum shear and tensile stresses, or combination of σ_{zz} and $\tau_{z\vartheta}$, that can be applied without reaching failure is an optimization problem. The Mohr's circle for the plane stress in the structure is shown in Figure 3.22. The circle must lie within the failure envelope while maximizing energy density. The objective function to maximize is the equation for energy density rewritten in terms of the principal stresses σ_1 and σ_2,

$$u = \frac{1}{2E}(\sigma_1 + \sigma_2)^2\frac{r_o^2 - r_i^2}{r_o^2} + \frac{1}{4G}(-\sigma_1\sigma_2)\frac{r_o^4 - r_i^4}{r_o^4} \quad (3.14)$$

where $\sigma_{zz} = \sigma_1 + \sigma_2$ and $\tau_{z\theta,out} = \sqrt{-\sigma_1\sigma_2}$. The variables σ_1 and σ_2 must fall within the ranges $\sigma_c \leq \sigma_2 \leq 0$ and $0 \leq \sigma_1 \leq \sigma_t$. Additional constraints are applied so that the Mohr's circle of the stress state falls within the boundary imposed by the failure envelope. The centre of the circle is located at $\sigma = \frac{\sigma_1+\sigma_2}{2}$, with a maximum shear stress $\tau_{max} = \frac{\sigma_1-\sigma_2}{2}$. The following constraints apply:

For $\sigma_c \leq \frac{\sigma_1+\sigma_2}{2} \leq \frac{-|\sigma_c|\sigma_t}{|\sigma_c|+\sigma_t}$, $\frac{\sigma_1-\sigma_2}{2}$ must be less than or equal to $\sqrt{\left(\frac{|\sigma_c|}{2}\right)^2 - \left[\left(\frac{\sigma_1+\sigma_2}{2}\right) + \left(\frac{|\sigma_c|}{2}\right)\right]^2}$.

For $\frac{-|\sigma_c|\sigma_t}{|\sigma_c|+\sigma_t} \leq \frac{\sigma_1+\sigma_2}{2} \leq \frac{|\sigma_c|\sigma_t}{|\sigma_c|+\sigma_t}$, $\frac{\sigma_1-\sigma_2}{2}$ must be less than or equal to $\frac{1}{2}\frac{(\sigma_t-|\sigma_c|)}{\sqrt{\sigma_t|\sigma_c|}}\left[\frac{\sigma_1+\sigma_2}{2}\right] + \frac{1}{2}\sqrt{\sigma_t|\sigma_c|}$.

For $\frac{|\sigma_c|\sigma_t}{|\sigma_c|+\sigma_t} \leq \frac{\sigma_1+\sigma_2}{2} \leq \sigma_t$, $\frac{\sigma_1-\sigma_2}{2}$ must be less than or equal to $\sqrt{\left(\frac{\sigma_t}{2}\right)^2 - \left[\left(\frac{\sigma_1+\sigma_2}{2}\right) - \left(\frac{\sigma_t}{2}\right)\right]^2}$.

The optimization code is shown in Appendix 1. The results show that there is no gain in combining torsion and tension for SWCNTs with a maximum diameter of 3 nm and thick MWCNTs. In these cases, the maximum strain energy occurs when σ_{zz} is equal to σ_t and $\tau_{z\theta}$ is 0. The analysis is the same for compression and torsion, and bending and torsion. Using this simple model, the analysis has shown that based on the simplifying assumptions that were made, there is little to gain in energy density by combining two deformation modes.

While combining deformation modes contributes little to increasing the energy density, it is likely that the best choice will be a coupling of multiple modes for convenience and compactness. In the end, the type of deformation that is chosen depends not only on the highest energy density, but also on which mode can be practically implemented and offers the most straightforward integration with the rest of the system.

3.7. Support structures

The calculations used to estimate energy density in the previous sections omit an important consideration: a support structure for a fully loaded spring. A support structure is needed for energy to be stored in a spring for a period of time prior to its release. For instance, a support structure in compression can be used to maintain a bundle of CNTs in tension. There are no materials as strong in compression as carbon nanotubes are in tension, so the supporting structure must be sufficiently large to support the load without reaching failure itself. When

accounting for the support structure, the energy density that can be stored in the combined spring and supporting structure will necessarily be lower than the strain energy density of the spring alone because of the added volume and mass. New estimates for energy density must be generated when a support structure is taken into consideration.

While the support structure under a load stores energy itself, the conservative assumption is made that only the energy from the spring can be extracted to perform useful work. For this reason, the energy stored in the support structure is neglected when calculating the overall energy density of the combined spring and support system. In practice, an architecture could be designed in which the energy in the support structure is used to perform work as well, so it may be possible to reach higher energy density levels than the ones proposed in the calculations that follow.

In a simple model of CNTs in tension, the support structure must support a compressive force F_s equal to the tensile force F in the carbon nanotubes, as shown schematically in Figure 3.23.

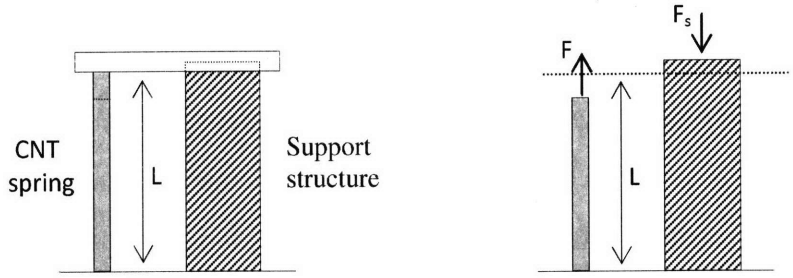

Figure 3.23: Schematic diagram of a support structure carrying the tensile load of a CNT spring.

The loaded spring and the support structure have a length of L. For the support structure, A_s is the cross-sectional area, E_s is the Young's modulus, ε_s is the maximum allowable strain, σ_s is the maximum allowable stress, and ρ_s is the density. For the spring, the CNTs are treated as continuum structures where A is the shell cross-sectional area, A_{encl} is the enclosed area of the CNTs, E is the Young's modulus, ε is the applied strain, σ is the stress in the spring, and ρ is the density. The compressive and tensile forces acting on the two structures in equilibrium are equal and opposite, so $F=F_s$ and $\sigma A = \sigma_s A_s$. Then, the minimum allowable cross-sectional area of the support structure can be expressed in terms of the cross-sectional area of the spring:

$$A_S = \frac{\sigma}{\sigma_s} A \tag{3.15}$$

The strain energy density of the combined spring and support is the strain energy in the spring divided by the enclosed volume of both the spring and the support:

$$u = \frac{\frac{1}{2} E\varepsilon^2 AL}{A_{encl} L + A_s L} = \frac{\frac{1}{2} E\varepsilon^2 AL}{A_{encl} L + \frac{\sigma}{\sigma_s} AL} = \frac{\frac{1}{2} E\varepsilon^2}{\frac{A_{encl}}{A} + \frac{\sigma}{\sigma_s}} \tag{3.16}$$

Strain energy was divided by the loaded volume rather than the unloaded volume because the difference between the two is small, and the loaded volume better reveals the trends. The fill factor *k* for bundles is neglected in this calculation, so *k* is set to 1. With no support structure, the energy density is given by $u = \frac{1}{2} E\varepsilon^2 \frac{A}{A_{encl}}$, the same result that was found in section 3.1.

The energy density by mass is calculated by dividing the strain energy by volume by the effective density of the combined spring and support structure. The effective density is calculated as:

$$\rho_{eff} = \frac{\rho V + \rho_s V_s}{V + V_s} = \frac{\rho AL + \rho_s A_s L}{L(A + A_s)} = \frac{\rho \frac{\sigma_s}{\sigma} + \rho_s}{\frac{\sigma_s}{\sigma} + 1} \tag{3.17}$$

Calculations are performed using bundles of 1.02 nm diameter SWCNTs, with A/A_{encl}=0.75. The density of the spring is estimated by multiplying the density of graphite, 2200 kg/m^3, by $k \cdot \frac{A}{A_{encl}}$, for a density estimate of ρ=1650 kg/m^3. Table 3.1 lists properties of several materials that could potentially be used to build a support structure, chosen for their high compressive strength. The plots in Figure 3.24 and Figure 3.25 show the strain energy density by volume and mass of a bundle of SWCNTs stretched in tension when a support structure made of different materials is taken into account.

Table 3.1: Mechanical properties of materials for a support structure [94-96]

Material	Young's modulus	Compressive yield strength	Compressive yield strain	Density
Single crystal silicon	160 GPa	7 GPa	0.044	2300 kg/cm^3
Single crystal SiC	450 GPa	21 GPa	0.047	3200 kg/m^3
Hot-pressed SiC-N	460 GPa	7 GPa	0.016	3200 kg/m^3
Single crystal diamond	1 TPa	53 GPa	0.053	3500 kg/m^3

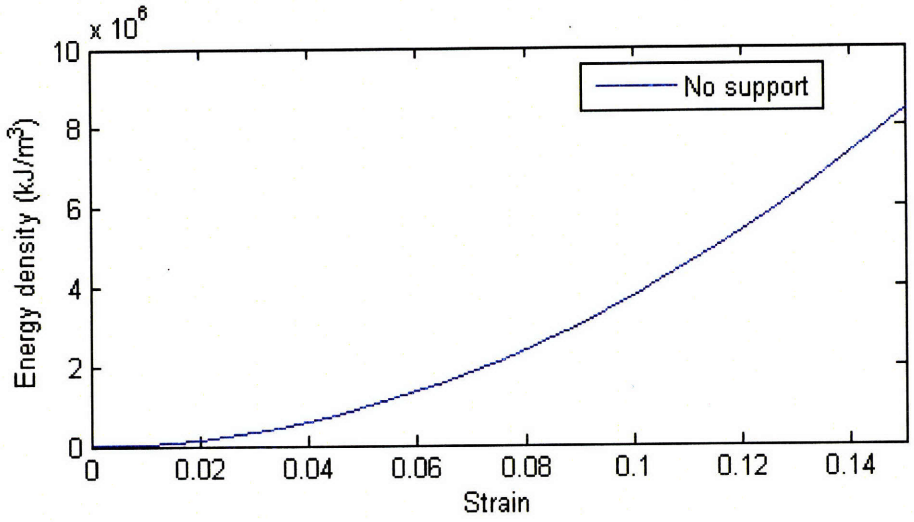

(a)

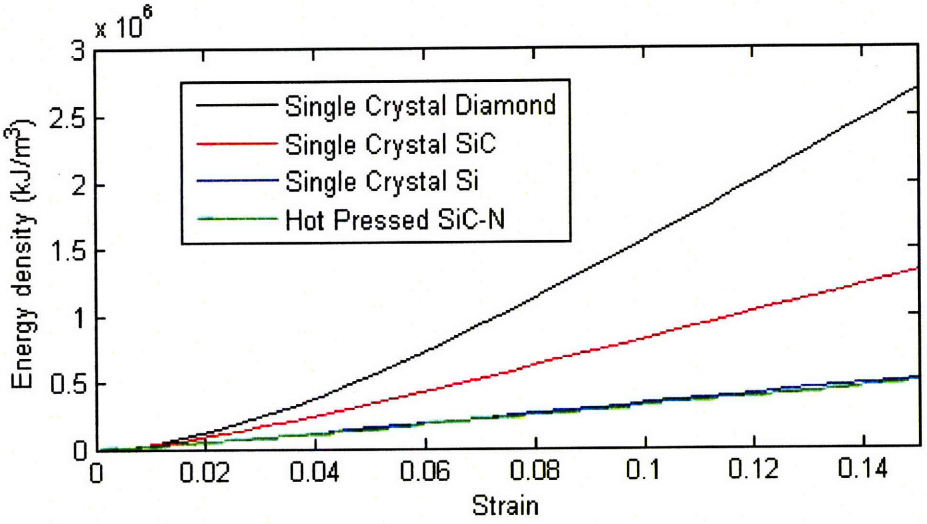

(b)

Figure 3.24: Strain energy density by volume for a bundle of SWCNTs with d=1.02 nm as a function of tensile strain (a) with no support structure and (b) with a support structure made of different materials.

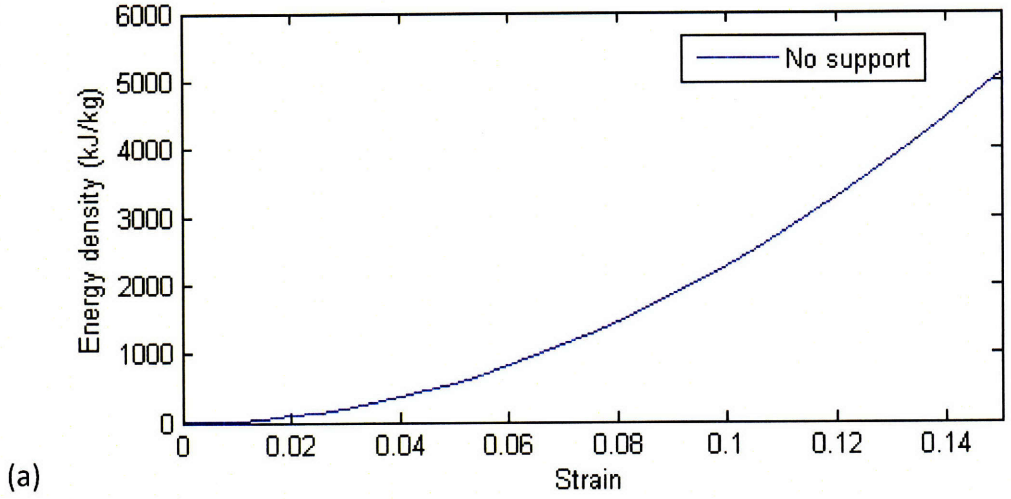

(a)

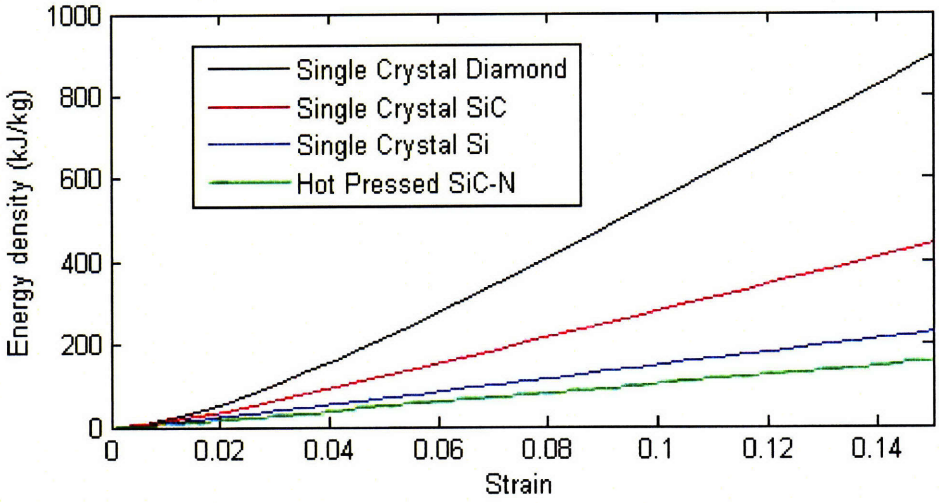

(b)

Figure 3.25: Strain energy density by mass for a bundle of SWCNTs with d=1.02 nm as a function of tensile strain (a) with no support structure and (b) with a support structure made of different materials.

The plots in Figure 3.24 and Figure 3.25 indicate that once a supporting structure is taken into consideration, the strain energy density is considerably reduced. The choice of material for the support structure is important because its properties have an important impact on the resulting energy density. The best material for the support structure is single crystal diamond, followed by single crystal silicon carbide. For example, at a strain of 0.1, a CNT spring under tension on its own can store 3.75 x 10^6 kJ/m^3. With a support made of diamond, the energy density is reduced by 59% to 1.55 x 10^6 kJ/m^3. For a support made of silicon carbide, the energy is reduced by 78% to 8.2 x 10^5 kJ/m^3. The reported energy density of lithium-ion batteries is in

the range of 1.08 x 10^6 to 1.44 x 10^6 kJ/m^3 [97], so the energy density of a spring at the highest strains with a support structure made of diamond is in the same range as the energy density of batteries. With a support made of silicon carbide, the energy density is lower than batteries. The energy density of the best large-scale carbon-steel springs available today is about 3000 kJ/m^3 [98] or 0.385 kJ/kg. With a strain of 0.1 in a CNT-based spring, the energy density by volume is 500 times greater with a diamond support and 270 times greater with a silicon carbide support than the energy density of a carbon-steel spring. These encouraging results indicate that CNTs can be used to make mechanical springs with far more energy storage capacity than the best mechanical springs currently available. Diamond would be a better choice than silicon carbide for the support structure, but its cost is a concern. There are some high-end applications, such as mechanical watches, where expensive components may be acceptable, so an analysis of the cost required to build a support structure made of diamond is performed in section 3.7.1.

The first support structure proposed for a CNT-based spring in tension was a support in pure compression, as shown schematically in Figure 3.23. An alternate support structure is proposed below. The second design is a circular shaft around which a stretched CNT spring is wrapped, as shown in Figure 3.26. When a CNT bundle with a stress of σ is wrapped around the circumference of the shaft, the pressure acting on the shaft is $P = \sigma t/R$, where t is the thickness of the CNT bundle and R is the radius of the shaft. For a solid circular shaft under a uniform pressure P, assuming plane stress, the radial stress is $\sigma_{rr} = -P$ and the tangential stress is $\sigma_{\vartheta\vartheta} = -P$, throughout the cylinder. This stress distribution results in a uniform Mises stress of P, so the maximum pressure that the shaft can support is equal to the compressive yield strength σ_y of the material. The maximum stress that can be applied to the CNT bundle wrapped around the shaft is $\sigma_{max} = \sigma_y R/t$. Single crystal silicon carbide has a high compressive yield strength σ_y of 21 GPa, so for the purposes of this discussion, silicon carbide is the material chosen for the shaft.

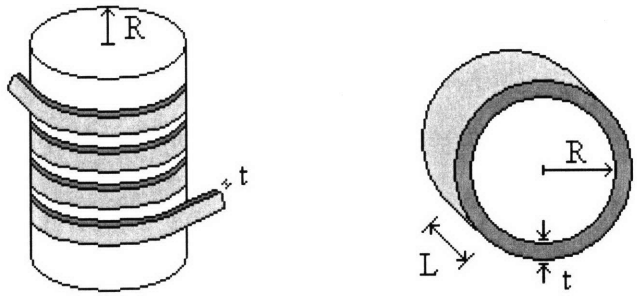

Figure 3.26: Shaft of radius *R* supporting a CNT spring stretched in tension.

A bundle of 1.02 nm diameter SWCNTs with A/A_{encl}=0.75 is modeled with *k* set to 1 in order to obtain values for the maximum energy density in this support configuration. The overall strain energy density is the strain energy in the spring divided by the enclosed volume of both the spring and supporting structure, and is modeled as

$$u = \frac{\frac{1}{2} E\varepsilon^2 \cdot 2\pi RtL \cdot A / A_{encl}}{2\pi RtL + \pi R^2 L} = \frac{E\varepsilon^2 t \cdot A / A_{encl}}{2t + R} \tag{3.18}$$

Parameters *t* and *R* are related by the expression $\sigma_{\max} = \sigma_y R/t$, or $\frac{R}{t} = \frac{E\varepsilon}{\sigma_y}$ where

ε is the strain applied to the spring and *E* is the Young's modulus of the CNT bundle. The expression for strain energy density is rewritten as

$$u = \frac{E\varepsilon^2 \cdot A / A_{encl}}{2 + R/t} = \frac{E\varepsilon^2 \cdot A / A_{encl}}{2 + \frac{E\varepsilon}{\sigma_y}} \tag{3.19}$$

For a shaft made of single crystal silicon carbide with a compressive yield strength σ_y of 21 GPa,

$$u = \frac{E\varepsilon^2 \cdot 0.75}{2 + \frac{E\varepsilon}{21\times10^9}} \text{ J/m}^3 \tag{3.20}$$

For a shaft made of single crystal diamond with a compressive yield strength σ_y of 53 GPa,

$$u = \frac{E\varepsilon^2 \cdot 0.75}{2 + \frac{E\varepsilon}{53\times10^9}} \text{ J/m}^3 \tag{3.21}$$

Strain energy density is plotted against strain in Figure 3.27 for a circular shaft as the support structure, for both silicon carbide and diamond. On the same graph, the strain energy density is shown for a supporting structure in pure axial compression, to compare the two results.

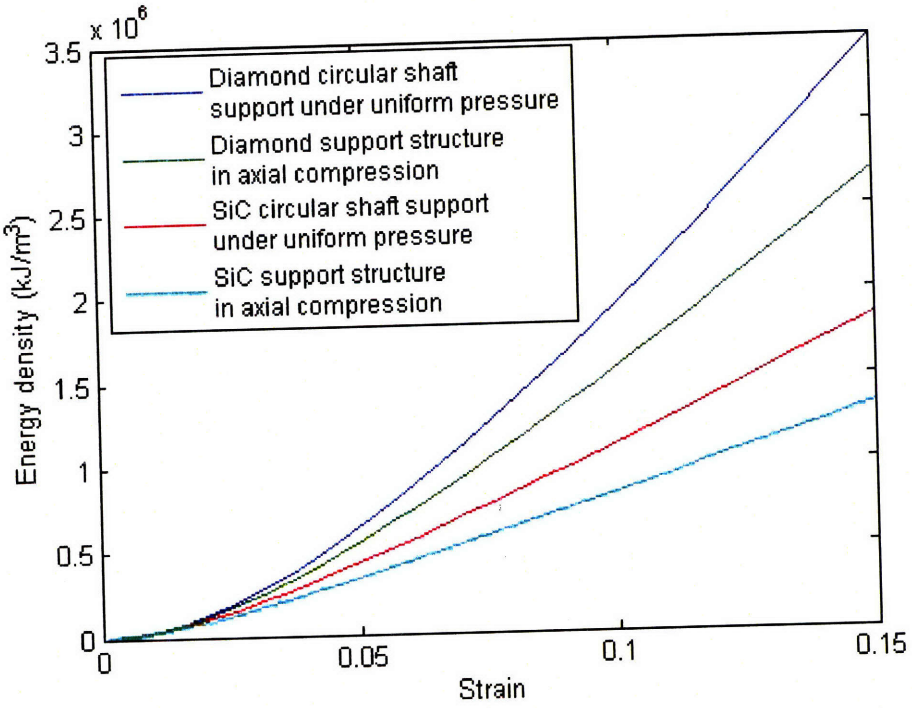

Figure 3.27: Energy density as a function of strain for single crystal diamond and silicon carbide support structures in axial compression and a circular shaft support under uniform pressure.

The graph in Figure 3.27 shows that higher strain energy density can be reached with a circular shaft support than with a support in axial compression, though the difference between the two support structures is relatively small. The choice of support structure type will likely depend on the best way to integrate a support structure with the rest of the system architecture.

3.7.1. Cost analysis of a diamond supporting structure

It is useful to estimate the cost of a diamond support structure for a CNT spring used to power a mechanical watch, since single crystal diamond is the best choice of material for a support structure. The support structure is a cylindrical shaft made of diamond around which a CNT bundle is wrapped. It is reported that a mechanical watch requires 1 to 2 μW to operate

[99]. Using the upper limit of 2 μW, a mechanical watch requires E_{mw}=0.1728 J to operate for one day. The energy required for y days is $y \cdot E_{mw}$ J. Let the diamond shaft have a radius R and a length L. The thickness of the CNT spring wrapped around the circumference is t, as shown in Figure 3.28.

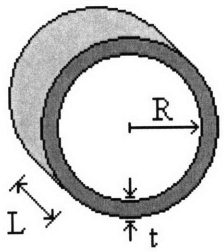

Figure 3.28: Schematic diagram of a CNT-based spring wrapped around a supporting shaft.

When a CNT bundle with a stress of σ is wrapped around the circumference of the shaft, the pressure acting on the shaft is

$$P = \sigma t / R = E\varepsilon t / R, \tag{3.22}$$

where E and ε are the Young's modulus and strain in the bundle. For a solid circular shaft under a uniform pressure, the Mises stress in the cross-section of the shaft is uniformly equal to the applied pressure, so the maximum pressure that the post can support is equal to the compressive yield strength σ_y of the material. The expression for pressure acting on the shaft is rewritten as

$$\frac{R}{t} = \frac{E\varepsilon}{\sigma_y} \tag{3.23}$$

The strain energy that is stored in the spring is

$$U = \frac{1}{2} E\varepsilon^2 2\pi RtL \frac{A}{A_{encl}} \text{ J} \tag{3.24}$$

Let A/A_{encl} = 0.75. The energy that is extracted from the spring will be less than the energy that can be stored because of the losses in the watch mechanism, and let the efficiency of the energy conversion be η. The strain energy extracted from the spring must be equal to the required energy to operate over y days. Then,

$$\frac{1}{2} E\varepsilon^2 2\pi RtL \frac{A}{A_{encl}} \eta = E_{mw} \cdot y \text{ J} \tag{3.25}$$

An expression for the length of the spool needed to support a spring of strain ε is

$$L = \frac{E_{mw} y}{\frac{A}{A_{encl}} \eta \pi E^2 \varepsilon^3 t^2 / \sigma_y} \text{ m} \tag{3.26}$$

The corresponding volume of the spool is

$$V = \frac{\pi R^2 E_{mw} y}{\frac{A}{A_{encl}} \eta \pi E^2 \varepsilon^3 t^2 / \sigma_y} = \frac{E_{mw} y}{\frac{A}{A_{encl}} \eta \varepsilon \cdot \sigma_y} \text{ m}^3 \tag{3.27}$$

If the density of the spool is ρ, then the mass of the spool is given by

$$m = \rho \cdot \frac{E_{mw} y}{\frac{A}{A_{encl}} \eta \varepsilon \cdot \sigma_y} \text{ kg} \tag{3.28}$$

The cost of diamonds in dollars/kg is C. Then the cost of the spool is

$$cost = C \cdot \rho \cdot \frac{E_{mw} y}{\frac{A}{A_{encl}} \eta \varepsilon \cdot \sigma_y} \tag{3.29}$$

The estimated cost per unit mass of single crystal diamond is C= 25 $\times 10^6$ dollars/kg, the density of diamond is ρ=3500 kg/m^3, and the yield stress of diamond is 53 GPa. Substituting all values, the total cost of the spool becomes

$$cost = \$\,25 \times 10^6 \cdot 3500 \frac{0.1728y}{0.75\eta\varepsilon \cdot 53 \times 10^9} \tag{3.30}$$

This result indicates that the cost depends on the strain in the spring, the efficiency of the energy conversion and the number of days that the spring should operate. The higher the strain applied to the CNT spring, the lower the cost of the diamond shaft. The cost is inversely proportional to the efficiency, so a high efficiency is needed for a low cost. The cost of the diamond spool needed to support a spring that stores enough energy to run a mechanical watch for 30 days is plotted against strain in Figure 3.29, for a watch mechanism that operates with 50% and 100% efficiency.

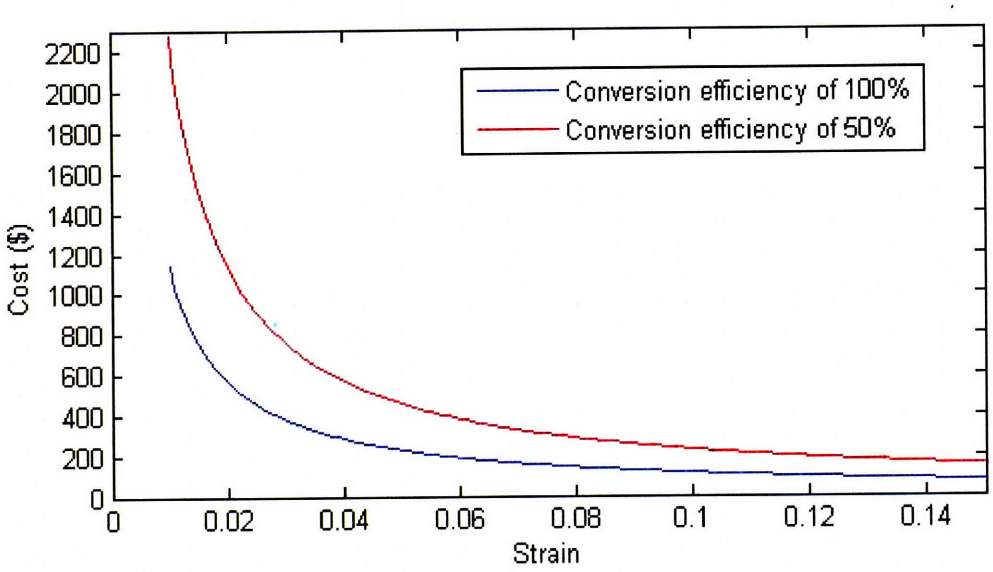

Figure 3.29: Cost of the diamond spool plotted against strain for a watch mechanism that stores enough energy for 30 days and operates with 100% efficiency and 50% efficiency.

The cost of the diamond support structure decreases with the strain in the spring, so it is advantageous to apply high strains to the CNT spring. Even at the highest strains, the cost of the material for the support structure remains large, so such a support could only be used in applications such as mechanical watches where this high cost is acceptable.

3.8. Implementation Issues

In an actual device, the energy density will be lower than the theoretical estimates. Any additional mechanisms coupled to the spring add mass and volume to the system and lower its overall energy density. A support structure reduces the energy density, as would the optional addition of a generator, motor or energy release rate regulation mechanism. Since energy cannot be extracted from the springs with 100% efficiency, the extractable energy density will be lower than what is stored.

The mechanical properties of carbon nanotubes are sensitive to defects and impurities which lower their Young's modulus and failure strength [64, 100]. CNTs of high purity and low defect density are needed for the springs to be able to reach the largest theoretically predicted strains reversibly and without inducing fracture or plastic deformation.

Strong attachment methods are important for large strains to be applied to CNTs or CNT groupings without inducing failure at the attachment site. The attachment site must also ensure that all tubes and all shells are well gripped so that loading is evenly distributed among all tubes in the structure. Otherwise, the strength of the spring will be lower than the predicted values.

Previous research has demonstrated that it is possible to fill the inside of CNTs with atoms. Filling CNTs has been shown to provide reinforcement to the CNTs in the radial direction, which may help prevent buckling in torsion and bending [8]. This could be a valuable technique for building CNT springs because it would allow CNTs to withstand higher stresses without buckling and extend the limits of energy storage.

3.9. Comparison of energy sources

In this section, the estimates of energy density of carbon nanotube springs are compared to the energy density of common micro-scale and macro-scale energy sources.

3.9.1. Steel watch springs

The energy density that can be reached in a carbon-steel spring is modeled so that it can be compared to estimates for CNT springs. Watch springs, also called mainsprings, are torsional springs made of a long strip of hardened steel wound into a tight coil. This type of spring is used to power mechanical watches because of its compact shape and the high energy density of steel. The thin strip of steel has a rectangular cross-section. One end of the steel strip is attached to and coiled around an inner shaft while the other end is attached to a fixed outer casing, as shown in Figure 3.30. Rotating the shaft in one direction winds the steel strip around the shaft. The elastic deformation in the steel results in energy storage. When the shaft is released, the steel strip unwinds, driving the shaft to spin in the opposite direction, which is used to drive external gears. The energy stored in the spring is equal to the elastic strain energy of the spring in its fully wound state.

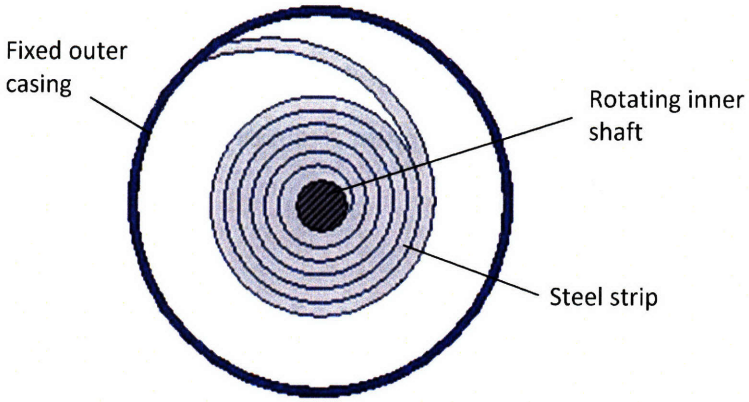

Figure 3.30: Illustration of a fully wound steel mainspring.

A maximum strain of ε can be applied to the steel, above which bending is no longer elastic and the spring becomes permanently deformed. For maximum elastic energy storage, the strain should be just below ε at the outer surfaces of the coil along the entire length of the strip. For a shaft with a small radius, the strip requires an initial curvature so that the steel can be bent to the required curvature without exceeding its elastic limit. Indeed, the initial curvature of the steel varies along the length of the strip since the radius of curvature of the fully wound spring also varies along the length of the strip. When bending is applied to a beam with an initial curvature, the strain varies hyperbolically throughout the thickness of the beam, and the strain energy in the spring will depend on the dimensions of the steel strip and the diameter of the shaft. To estimate the amount of energy in a carbon steel spring independently of the dimensions of the spring and the shaft, the simplifying assumptions are made that the neutral axis is located at the centre of the beam and that the strain varies linearly through the thickness of the beam. It is assumed that the strip of carbon-steel has an initial curvature that varies along its length such that a maximum strain of ε is reached at the inner and outer surfaces throughout the coil.

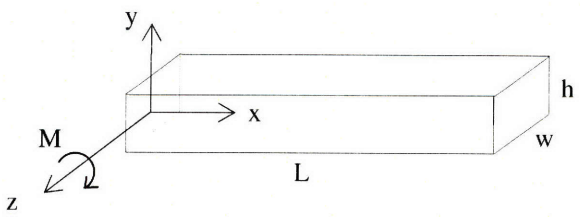

Figure 3.31: Beam with a rectangular cross-section

For a beam in bending with a moment applied about the z-axis, a rectangular cross section and a linear distribution of strain with a maximum strain of ε at the outer surfaces, the strain in the beam is

$$\varepsilon_x(y) = \frac{y}{h/2}\varepsilon \tag{3.31}$$

The elastic strain energy of the beam is

$$U = \frac{1}{2}\int\int\int(\sigma_x\varepsilon_x)dxdydz = \frac{EwL}{2}\int_{-h/2}^{h/2}\frac{y^2}{h^2/4}dy = \frac{1}{6}EwLh\varepsilon^2 \tag{3.32}$$

The estimate for the strain energy density in the coil is then

$$u = \frac{1}{6}E\varepsilon^2 \tag{3.33}$$

With a maximum allowable strain of 0.005 for carbon steel and a Young's modulus of 210 GPa, the strain energy density that can be stored in such a spring is 875 kJ/m^3. With a density of carbon-steel of 7800 kg/m^3, this corresponds to an energy density by mass of 111 J/kg. The current maximum energy density of a watch spring is reported to be between 1080 kJ/m^3 [99] and 3000 kJ/m^3[98], presumably using higher strength steel, so the simple estimate made here is reasonable.

3.9.2. Energy density comparisons

On-board energy sources available to MEMS devices include batteries, fuel cells, internal combustion engines and capacitors. The energy densities of MEMS energy sources are listed in Table 3.2. The energy density and conversion efficiency of energy sources for larger scale applications are listed in Table 3.3.

Table 3.2: Energy density of energy sources for MEMS applications [99, 101]

Energy source	Energy density by volume
Power capacitor	4 kJ/m^3
Fuel cell	6.5 x10^3 kJ/m^3
Thick film battery	1 x10^6 kJ/m^3
Thin film battery	2.5 x10^6 kJ/m^3
Hydrocarbon fuel (gasoline)	35 x10^6 kJ/m^3

Table 3.3: Energy density of energy sources for large-scale applications [97, 102-104]

Energy source	Energy density by volume	Energy density by weight	Conversion efficiency
Carbon-steel springs	3 x10^3 kJ/m^3	0.38 kJ/kg	
Ultracapacitor		10-20 kJ/kg	90-95%
Fuel cells	10.8 - 18 x10^6 kJ/m^3	720-900 kJ/kg	25-35%
Lithium-ion batteries	1.08-1.44 x10^6 kJ/m^3	468 kJ/kg	near 100%
Gasoline	32 x10^6 kJ/m^3	40-50 x10^3 kJ/kg	20%

A CNT spring made of bundles of densely packed 1.02 nm diameter SWCNTs stretched to a 10% strain is predicted to hold 3.4 x10^6 kJ/m^3 or 2272 kJ/kg, with A/A_{encl}=0.75, k=0.91 and a density of 1501.5 kg/m^3. When taking into consideration a support structure made of single crystal silicon carbide, this energy reduces to 1 x10^6 kJ/m^3 or 672 kJ/kg. Without accounting for the volume and weight of any additional energy extraction hardware, the energy density of carbon nanotube springs is greater than that of mechanical springs and ultracapacitors and in the same range as the energy density of batteries. The energy density of CNT springs is still far lower than the energy density of hydrocarbon fuels.

Once energy extraction mechanisms are taken into account, the energy density of a power source incorporating CNT springs will likely be lower than that of batteries. An exact value of the energy density depends on the extraction hardware and choice of material for the support structure. In general, CNT springs may not be a viable alternative to batteries strictly in terms of energy density. However, CNT springs have the potential to significantly improve upon the energy density limits of current mechanical springs. A CNT spring stretched to a 10% strain holds more than 330 times by volume and 1200 times by weight the energy of a steel spring, a result that suggests that macroscopic assemblies of carbon nanotubes could be used to

fabricate high performance mechanical springs with far greater energy storage capabilities than what is currently available.

The energy density of a bundle of 1.02 nm diameter SWCNTs under tensile loading is summarized in Figure 3.32, once a cylindrical shaft support structure of different materials is taken into account. The energy density of lithium-ion batteries and steel springs are plotted on the same graph for comparison. The maximum achievable overall stored energy density is predicted to be comparable to lithium-ion batteries as long as high elastic strains can be applied to the CNTs and a high quality material is used for the support structure.

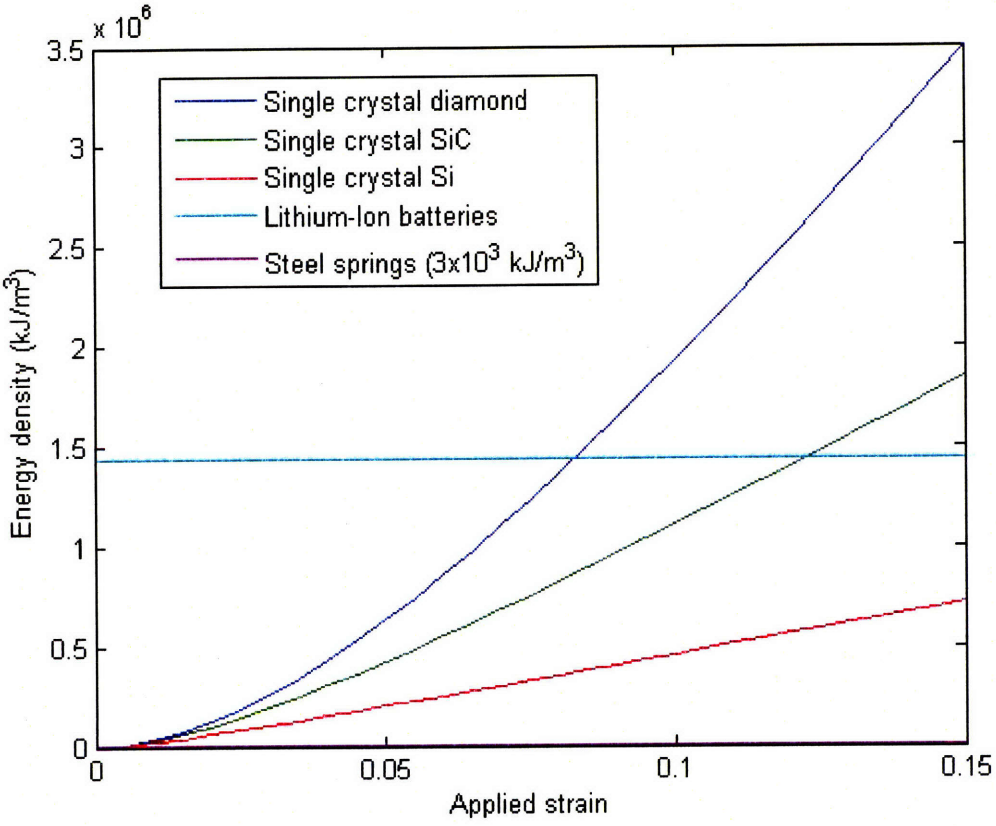

Figure 3.32: Energy density of a bundle of SWCNTs under tensile loading with a cylindrical shaft support structure made of single crystal diamond, single crystal silicon carbide and single crystal silicon, compared to the energy density of conventional energy storage technologies.

A number of applications have been identified that would benefit from improved mechanical springs. At the microscale, CNT springs could be used as an energy source for MEMS, particularly for devices that require energy supplied in the mechanical domain. The

weight and volume of on-board power sources for MEMS tend to be disproportionately large compared to the rest of the device [99]. With sizes on the microscale and a low density, CNT springs would offer an alternative to MEMS batteries and capacitors. In applications where kinetic energy is available, the motion of an eccentrically rotating mass could be used to create a CNT spring that is self-winding. At the macroscale, CNT springs can be used to build an improved mechanical watch spring. The use of CNTs would enable watch springs that store more energy and require less frequent windings than current steel mainsprings. Regenerative braking systems convert the kinetic energy of a vehicle during braking into stored energy that can be later used to accelerate the vehicle. In bicycles, these mechanical regenerating braking systems typically use either metal springs, which have low energy storage capacity, or generator/motor systems for storing energy during braking, making the systems heavy and unwieldy [105]. Regenerative braking could be improved by using lightweight, high energy density CNT springs.

CNT springs are added to the Ragone plot in Figure 3.33 [106] to illustrate how CNT springs compare to other energy sources. The estimated energy density of a CNT spring with a single crystal silicon carbide support of 672 kJ/kg corresponds to 187 Wh/kg, in the same range as the energy density of lithium ion batteries. The power density of the spring is dominated by the mechanism used to extract the energy. A spring coupled to a generator may release its energy on a timescale of seconds to minutes, or longer. A spring coupled to a mechanism analogous to a catapult may release its energy in a timescale on the order of milliseconds. Discharge times of 50 ms and 1 minute result in a power densities of 13 MW/kg and 11 kW/kg respectively. The ability of springs to discharge very rapidly indicate that they may be able to reach similar power density levels as capacitors, or potentially even higher, which places CNT springs in the top right corner of the graph.

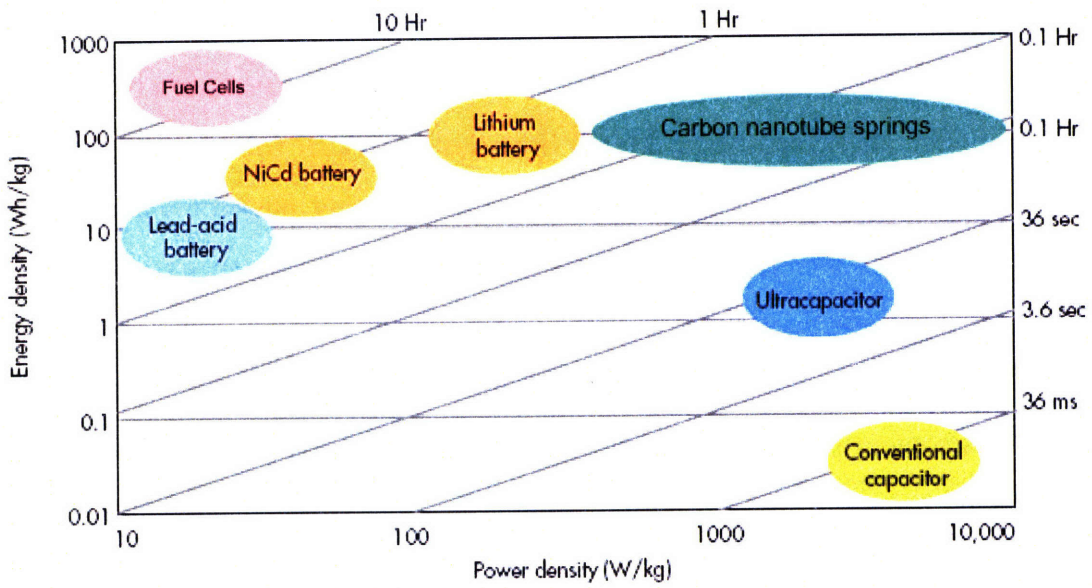

Figure 3.33: Ragone plot [106] with the expected energy density and power density of carbon nanotube springs.

In addition to their high energy density and potentially high power density, CNT springs may improve upon the limitations of other energy storage media. Electrochemical batteries must operate within a specific temperature range for acceptable performance. The operating range of lithium-ion batteries is -20°C to 60°C, with limited performance at cold temperatures and rapid discharge at high temperatures. CNT springs would have a much wider range of operating temperatures, with structural stability up to 2000°C [107, 108]. Temperature insensitive springs made of CNTs could operate far above 60°C where batteries cease to be operational.

Self-discharge of batteries, due to electrochemical reactions taking place inside the battery even when not in use, can result in discharge rates as high as 20% per month. Since elastic energy storage relies on stretching bonds rather than on chemical reactions, CNT springs are expected to have little or no self-discharge. Self-discharge of batteries is particularly detrimental in battery-powered devices that are used infrequently or only in emergency situations. Another drawback of chemical batteries is their limited number of charge-discharge cycles. If the strains applied to CNT springs can remain elastic and reversible, then their number of charge-discharge cycles is potentially infinite. With their short lifetime, batteries require continual disposal and replacement. A power source with a potentially infinite lifetime would help to alleviate the waste generation problem of batteries.

Energy storage based on CNT springs can offer a safer alternative to batteries. Leaks or degradation of battery packaging can lead to exposure to toxic chemicals. Risks include explosion or pyrolysis if battery casing is damaged, dismantled or heated. In contrast, CNT springs contain no toxic, poisonous or carcinogenic chemicals so their operation is expected to be safer.

In summary, CNT springs offer the potential to provide a reliable method for high density energy storage that offers rapid discharge, unlimited charge-discharge cycles, no self-discharge, safer operation, and no degradation at high temperatures or under harsh conditions. For applications where these criteria are important, CNT springs for energy storage may provide a valuable alternative to electrochemical batteries.

4. Energy storage mechanisms

4.1. Basic system architecture of a power source

A mechanical spring must be coupled to external mechanisms to build a power source that is functionally useful. On its own, a spring stores potential energy when an external force is applied to it but releases the energy in a single rapid burst once the force is removed. An effective power source needs to store energy over a period of time, release the energy only when needed and discharge the energy at a desired power level. A CNT-based portable power source should have a basic architecture made of four main components: a CNT spring, a supporting structure for the spring, a generator-motor combination, and a coupling mechanism between the spring and the generator.

Before considering the components required for a power source, the scale of the system must be addressed. The size of the spring is flexible and can be chosen to meet the energy requirements of the system being powered. Individual or small bundles of nanotubes have nanometer-scale diameters and lengths on the order of microns. With low defect densities and excellent mechanical properties, these structures are well-suited for use as mechanical storage elements for nanoscale or microscale systems, particularly devices that require a rapid discharge of energy in the mechanical domain. At this scale, manipulating, positioning, and attaching the springs to a substrate are considerable challenges. Any external components coupled to the spring to provide enhanced functionality to a power source must be designed with low complexity since micro structures can be fabricated with considerably less accuracy relative to their size than macroscale structures. Simple and error-insensitive components are needed with few moving parts because of wear and friction at the microscale.

Macroscale CNT assemblies tend to have inferior properties than their nano or microscale counterparts, but as springs they have a larger capacity for energy storage and are easier to manipulate. Applying a deformation to a macroscale assembly enables thousands of CNTs to be loaded to their elastic limit at once. Complex mechanisms such as gears, generators and motors can be coupled to the spring to build a power source with enhanced functionality.

Another scaling alternative is to build power generating "unit cells". Each unit cell would be an energy generating unit containing a spring along with some extraction hardware, built at a scale that facilitates fabrication and optimizes efficiency and energy density. A larger power source with longer lasting operation or higher power levels can be built from an array of unit cells that are activated in parallel or in series. This would be an efficient way of storing large amounts of energy while keeping the spring at an optical scale for energy density.

The objective of a power source is to store and deliver a large amount of energy, so high conversion efficiencies throughout the design are essential. The design of a power source should be made within the context of optimizing performance, manufacturability, cost effectiveness, reliability and system complexity. The entire device should be composed of a large percentage of CNTs by volume and mass to maximize its storage capacity and energy density. Any additional mechanisms coupled to the spring reduce the overall energy density of the system.

The first component of the architecture for the power source is the CNT spring; its design is informed by the analyses of Chapter 3. The spring can be made of a single CNT or CNTs arranged into microscale or macroscale groupings with a range of diameters, lengths and numbers of shells. How best to build the spring depends on the scale at which the highest energy density and extraction efficiency can be achieved as well as on the amount of energy the power source is expected to store. If CNTs are arranged in groupings, then tight packing and good alignment are needed between the tubes to achieve a high density. Good load transfer and effective attachment techniques are required so that all shells in the case of MWCNTs, and all tubes in the case of bundles, can be loaded to near their elastic limit. If the springs are made of bundles of discontinuous CNTs, then long overlaps on the order of 100 μm [57] between the tubes are needed to ensure that the bundle's performance is similar to that of individual CNTs. Most importantly, the size and mass of the spring must be significant compared to the rest of the mechanism to ensure that the overall energy density remains high. The results of the previous chapter suggest that the poor load transfer between MWCNT shells makes these structures largely unsuitable for energy storage, while bundles of highly aligned continuous or discontinuous small diameter SWCNTs in densely packed lattices show considerable promise as

a material for springs. A deformation mode is needed to store energy in the spring, which can be any combination of axial tension, axial compression, torsion or bending. The choice depends not only on energy density but also on which of the deformation modes can be most easily applied in practice and how the deformed spring will integrate with the rest of the system. The highest energy densities are expected to be achieved with deformation in axial tension, though loading primarily in tension can be combined with bending to increase the compactness of the spring. Loading in tension is not limited by buckling strains and can achieve uniform loading throughout the entire structure. A final consideration is that the power conversion mechanism must match the scale of the spring. This requires either the ability to couple large numbers of CNTs to a single power conversion mechanism, or the ability to couple small numbers of CNTs to very small power conversion mechanisms. Since the technology for creating CNT groupings is more mature than the technology for very small, efficient generators, a more practical approach at this point is to use springs composed of large numbers of CNTs in conjunction with a larger generator.

A support structure is required to hold the spring in its fully loaded state prior to its release, as described in section 3.7. The design of the support structure will depend on the scale of the spring, the deformation mode and the architecture of the rest of the system. The material selected for the structure should have high strength because the added mass and volume of the support contribute to reducing the energy density of the entire system. Single crystal silicon carbide and diamond were previously identified as good materials for this structure. Support structures may be superior at the microscale because of the sometimes higher strengths of microscale materials as compared with bulk materials.

A generator is used to convert the mechanical work from the spring as it discharges into the electrical domain. To build a rechargeable power source, the generator should operate in reverse as a motor so that an electrical input to the system recharges the power source by rewinding the spring. Certainly, simpler systems can be designed without the need of a generator or a motor; the mechanical work from a spring can drive a mechanical load directly, and a motor can be eliminated from a device that is recharged using a mechanical input or that is intended for only a single use. The type of generator used depends on the scale of the

system, the amount of energy stored in the spring and rate of energy discharge from the spring. At the microscale, magnetic, electrostatic, and piezoelectric MEMS generators [109-114] would be feasible for implementation. The conversion efficiency of any motor or generator must be high to minimize energy losses. Generators and motors of reduced size and complexity are best since all mechanisms external to the spring reduce the energy density of the system.

The last component of the architecture is a method of coupling the spring to the generator. The role of the coupling mechanism is to convert the mechanical work of the unwinding spring into a form of work with an acceptable frequency and amplitude of motion for input into the generator. For instance, a simple coupling mechanism will allow the energy from the spring to be released in a single, rapid burst. A more complex coupling mechanism composed of a set of gears can be used to control the discharge of energy from the spring so that energy is released gradually over time to match a generator that operates at a lower frequency and handles smaller amounts of energy. In general, a tradeoff exists between the functionality provided by the coupling mechanism and the size and complexity that it adds to the system.

4.1.1. Examples

Simple schematic examples of power sources that store energy in CNT springs demonstrate the architecture needed to transform a simple spring into a useful power source. Figure 4.1 shows a power source that stores energy in a bundle or grouping of bundles of CNTs stretched in tension. Rack and pinion gears are used to convert the linear motion of the spring as it stretches and contracts into a rotational motion appropriate for input into a generator. These gears form the coupling mechanism. One end of the CNT grouping is attached to a fixed support and the other end is attached to the rack. The spring is stretched by turning the pinion in the clockwise direction, which can be done either mechanically or with an electrical input via a motor. A ratchet prevents motion of the pinion in the counter-clockwise direction so that the stretched spring cannot contract and energy can be stored in the spring prior to its release. The ratchet is the support structure, and it must be able to support the load of the fully stretched spring; the gear teeth must also be able to support the load. To release energy from the spring, the ratchet is disconnected from its gears, permitting the spring to contract, which drives the

rotation of the pinion in the counter-clockwise direction. The contraction of the spring will happen very rapidly. The rotation of the pinion can be used to drive either a mechanical load directly or a generator to obtain an electrical output.

A disadvantage of the design is the rapid contraction of the spring after its release. Most applications require an even input of energy over a period of time rather than a rapid burst of energy. Additional components may be added to the design to demonstrate how a more complex coupling mechanism can be used to control the rate of energy release from the spring. The design shown in Figure 4.2 is still made of groupings of CNT bundles stretched in tension, a rack, pinion and ratchet. An escapement mechanism, comprising an escape wheel, a pallet and a torsional spring are added to control the unwinding of the CNT spring. Escapement mechanisms are described in more detail in Chapter 5, but their operation is described here in brief. The pallet is driven by the torsional spring to have an oscillating motion. The periodic, oscillating motion of the pallet allows the escape wheel to rotate only in small increments at a time. The incremental rotations of the escape wheel in turn constrain the rotation of the pinion to be gradual, which slows the contraction of the CNT spring. To wind the spring, the gears of the escapement mechanism should be disconnected from the pinion. The ratchet acts as the support structure, ensuring that energy is stored in the spring until it is disengaged. A generator and motor may be coupled to the pinion for the system to deliver an electrical output and be wound using an electrical input.

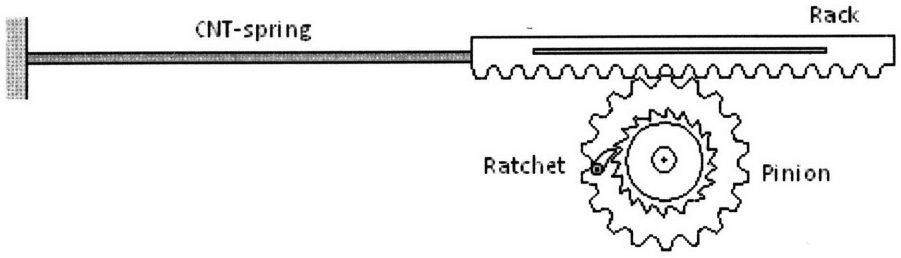

Figure 4.1: Conceptual design of a power source using a CNT spring stretched in tension, a rack and a pinion.

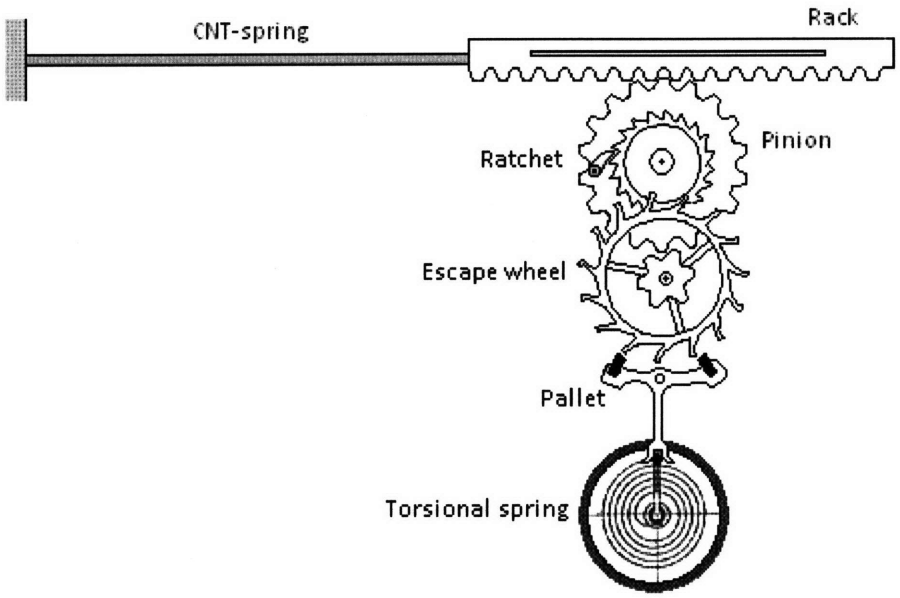

Figure 4.2: Conceptual design of a power source using a CNT spring stretched in tension, a rack, pinion, and an escapement mechanism.

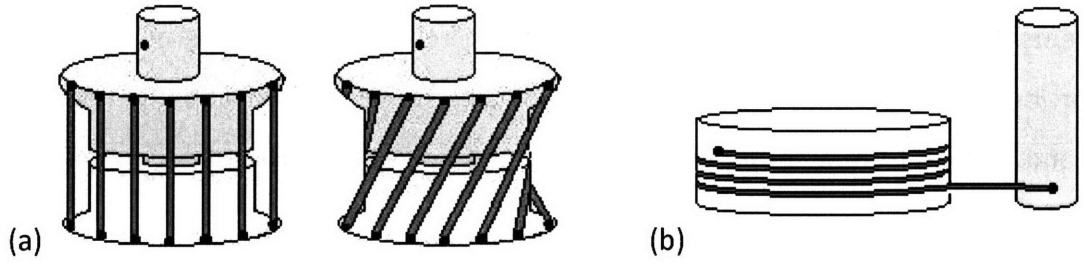

Figure 4.3: Designs of power sources using CNT-based springs.

Two additional schematic designs are shown in Figure 4.3. Figure 4.3 (a) shows CNT groupings attached to a cylindrical structure made of a fixed base and a top rotating shaft. In the diagram on the left, the CNTs are fully extended but unstrained. Rotating the top shaft with respect to the base stretches the CNTs in tension. The upper shaft is latched in place to keep the energy stored in the device. A motor and generator may be coupled to the upper shaft so that energy can be input to and removed from the system via the electrical domain. An advantage of this device is the ability to stretch many grouped CNTs at once, and the shaft and base serve as support structures in compression. Figure 4.3 (b) shows an alternative design in which a long CNT grouping is wound around a fixed shaft so that it is taut. One end of the grouping is attached to the fixed shaft while the second end is attached to a second rotating

shaft. The diameters of both shafts are sufficiently large so that deformation in bending is small and buckling due to bending will not occur. Both shafts serve as support structures. Winding the rotating shaft stretches the grouping in tension. Lubrication is needed to achieve minimal friction between the spring and the shaft surfaces since without lubrication, only a short segment of the grouping will become strained in tension due to the capstan effect. As with the other designs, a generator and motor pair could be integrated into the device. The advantage of this design is that it permits large amounts of energy to be stored in a single compact spring, whose scale can range from the microscale to the macroscale. All CNTs in the spring can be deformed using a single loading mechanism. A drawback is that radial deformation of the tube cross-sections will occur as the stretched grouping becomes compressed against the shaft surfaces.

As these conceptual designs demonstrate, there are many ways to design and build a mechanism to store and extract energy from CNTs. The scale of the spring and the choice of components to integrate with the spring can be selected with a high degree of flexibility. A good starting place is to build a simple proof of concept device that would demonstrate energy storage and release from a spring before more complex designs focused on optimization are untaken.

5. Power source with controlled energy release

5.1. Conceptual design of a unit cell

In this chapter, a design is presented of a conceptual microscale power source that stores energy in the elastic deformation of CNTs. The device is intended as a single unit cell that could be arrayed to form a larger power system. The design is proposed as a conceptual model to study the operation of a microscale unit cell and identify the challenges and limitations associated with designing such a system. The objectives for the unit cell are to achieve high energy conversion efficiency, a high percentage of CNTs by mass and volume, and the ability to control the rate of energy release from the spring. The system architecture is presented along with an analysis and discussion of each of the components. A model of the system was built in Simulink to simulate the system's performance. The simulation results are used to determine how scaling affects the power output, overall system efficiency, operating frequency of the energy regulation mechanism, and energy discharge time. Finally, the advantages and drawbacks of the system are discussed to assess the feasibility of building such a power source and to determine how the design may be improved.

One of the design objectives for the power source is the ability to control the rate of energy release from the spring. While the simplest way to release energy from a loaded spring is in a rapid burst, most applications require a steady flow of input power over a longer period of time. In a mechanical watch or clock, a single winding of a torsional spring can power the device for hours or days by means of an escapement mechanism. An escapement mechanism is a set of carefully designed gears whose rotation is controlled by an oscillator. In a watch, the oscillator is a torsional spring called a balance spring, and in a clock it is a pendulum. Two escapement designs are shown in Figure 5.1. The deadbeat escapement is used in pendulum clocks while the lever escapement is made for mechanical watches. Both designs have three main components: an oscillator, an escape wheel and a pallet.

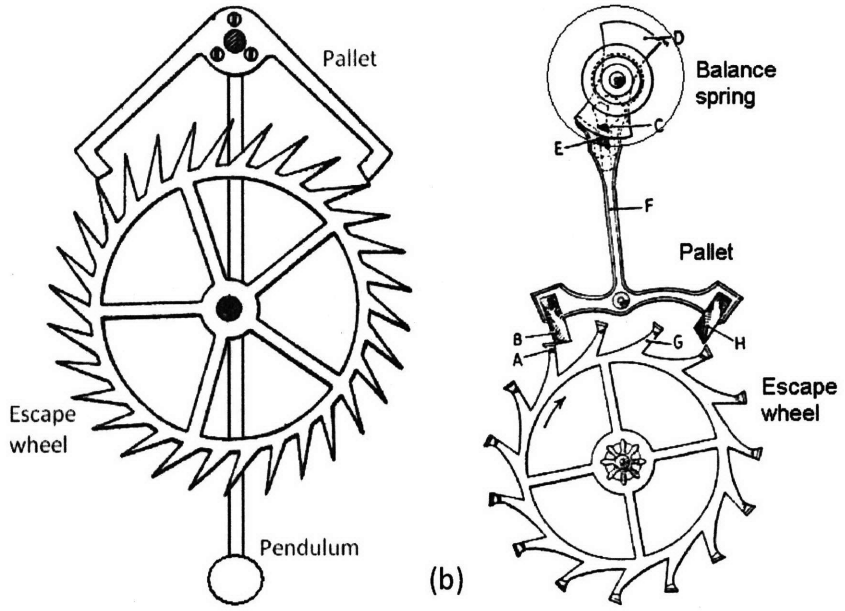

Figure 5.1: (a) A deadbeat escapement for a clock and (b) a lever escapement for a mechanical watch. Both escapements have three main components: an oscillator (pendulum or torsional spring), an escape wheel and a pallet [115].

Energy is stored in a watch or clock by winding a steel torsional spring called a mainspring. As the mainspring unwinds, it drives the escape wheel, a gear with specially designed gear teeth, to rotate. The pallet is a gear that is used to control the mainspring's rate of unwinding via the escape wheel. The motion of the pallet is driven by the oscillator. Through precise interlocking of the pallet and escape wheel teeth, each successive oscillation of the pallet allows the escape wheel to advance by an angle corresponding to a single gear tooth. The pallet has two locking faces and two impulse faces, as shown in Figure 5.2 (a). When a locking face of the pallet is in contact with an escape wheel tooth, the escape wheel is held stationary and prevented from rotating. As the pallet continues its rotation, an impulse face of the pallet comes into contact with an escape wheel tooth and the escape wheel becomes free to rotate. As the escape wheel rotates, it pushes against the impulse face of the pallet, and the elastic energy released from the spring gets transferred through the escape wheel and the pallet to the oscillator. This event is called an impulse. The motion of the components of an escapement mechanism is illustrated in more detail in Figure 5.2 (b).

The incremental rotations of the escape wheel allow the mainspring to correspondingly unwind by only a small increment with each pallet oscillation. Adjusting the period of the

oscillator, the size of the gears and the spacing of the teeth on the escape wheel provides a means of controlling the rate at which energy is released from the spring. The small boost of energy that the oscillator receives from the spring during each impulse replaces the energy it lost to damping during that period. Models of clock escapements show that if the frictional losses and the driving force of the impulses are constant, then the oscillator will maintain motion with a constant amplitude over an extended period of time and be stable to external disturbances [116, 117]. The regular motion of the oscillator results in motion of the pallet and incremental rotations of the escape wheel that also remain regular over time. The small, periodic rotations of the escape wheel allow a mechanical watch or clock to keep accurate time. The ability of the escapement to carefully control the rate of energy release from a mechanical spring has motivated its implementation into the power source design.

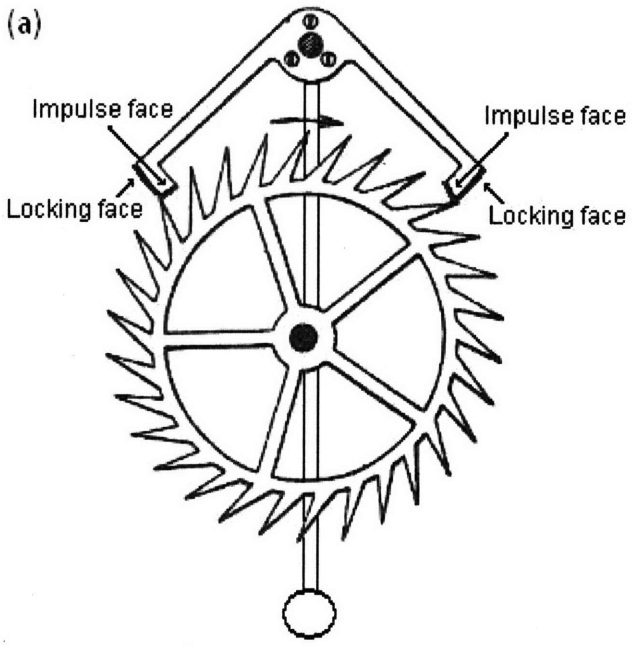

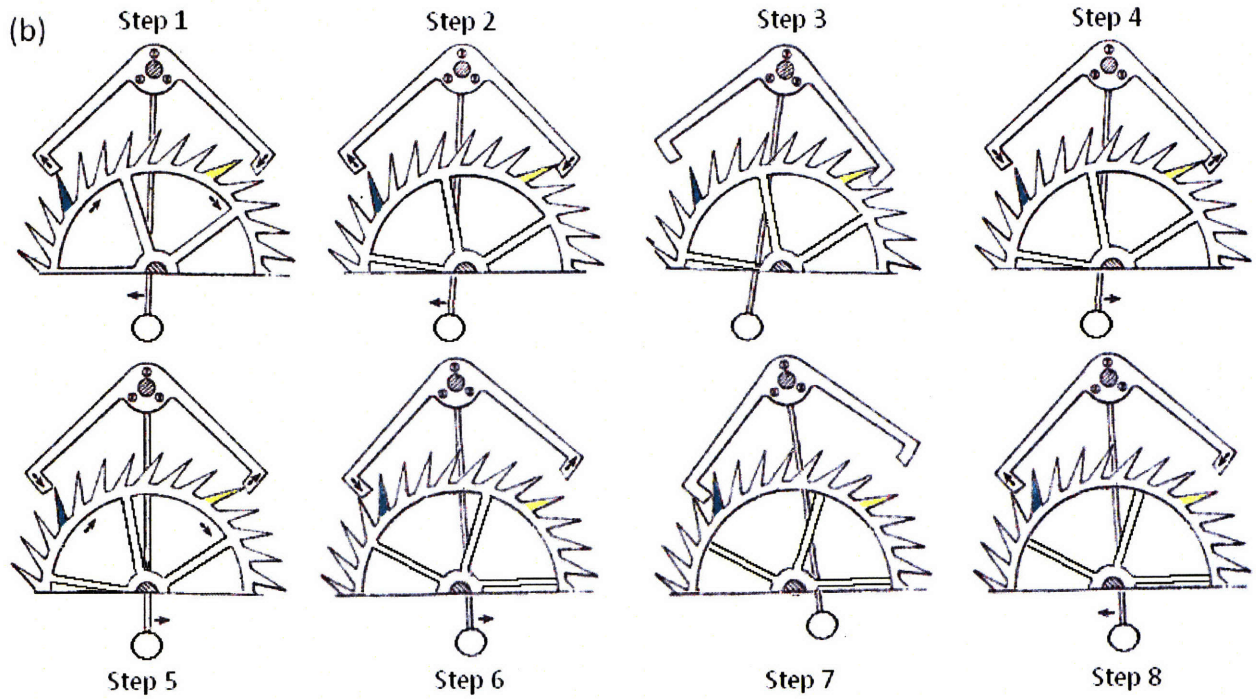

Figure 5.2: (a) Diagram of a deadbeat escapement showing the impulse faces and locking faces of the pallet. (b) Stages of an escapement mechanism. Step 1: An impulse is taking place on the left pallet tooth. The pallet is rotating in the clockwise direction about its pivot. As the escape wheel rotates clockwise, the green escape wheel tooth pushes against the left impulse face of the pallet. Step 2: The impulse is finished as the yellow escape wheel tooth catches the right locking face of the pallet. The escape wheel is locked and cannot rotate, while the pallet is free to oscillate. Step 3: The escape wheel remains locked, and the pallet has reached its maximum oscillation amplitude. Step 4: The escape wheel is still locked as the pallet changes direction and rotates counter-clockwise. Step 5: An impulse is taking place on the right pallet tooth. As the escape wheel rotates, the yellow escape wheel tooth pushes against the right impulse face of the pallet. Step 6: The impulse is finished as an escape wheel tooth catches the left locking face of the pallet, preventing the escape wheel from rotating. Step 7: The escape wheel remains locked, and the pallet has reached its maximum oscillation amplitude. Step 8: The escape wheel is still locked as the pallet changes direction to rotate clockwise. Following this step, the process returns to Step 1. The images in the figure are modified from [115].

5.2. System architecture

The energy storage element implemented in the conceptual power source is a spring made of CNTs. The results of Chapter 3 indicate that energy can be stored with high density in bundles or groupings of bundles of SWCNTs stretched in axial tension, so this is the form of spring chosen for the model. The spring is modeled as a defect-free grouping of aligned, parallel

SWCNTs densely packed into an ideal hexagonal lattice, with a stiffness of 1 TPa and ideal strength. The groupings are assigned microscale diameters and lengths ranging from the microscale to a few millimeters. The length and diameter of the SWCNT groupings are adjusted in the model to vary the amount of energy stored in the spring. All groupings are assumed to be composed of continuous CNTs that span the entire length of the grouping. Van der Waals interactions between the tubes are assumed to give the assemblies ideal properties, and excellent load transfer is expected between the SWCNTs so that all tubes can be loaded to a uniform stress. While combining deformation modes may be more practical and compact in an actual device, loading in pure tension is a simple and useful representation of energy storage in a CNT spring for an analytical model.

A generator is needed to convert the output work from the spring into electricity. Different types of microscale generators have been previously fabricated, including MEMS electrostatic [113], magnetic [109], and piezoelectric [110-112] generators. The disadvantages of electrostatic and magnetic generators are high-speed rotating components and a relatively high level of operation and fabrication complexity. Piezoelectric generators have a small number of moving parts, an energy conversion efficiency as high as 80% [118], and the ability to operate at the microscale [110, 119], and they can be represented analytically using simple models. These reasons have motivated the selection of a piezoelectric generator for the model. The implementation of the piezoelectric generator in this application is similar to vibrational energy harvesters that use resonating piezoelectric cantilever beams to generate electrical power [110, 111]. The main difference between the present application and energy harvesters is that here the mechanical energy comes from a spring rather than from vibrations in the environment. The form chosen for the piezoelectric generator is a unimorph cantilever beam, consisting of a base made of elastic material and a top piezoelectric layer. The unimorph operates in 31 mode to enable large displacements.

The conceptual design presented here employs components that are chosen for simplicity of operation and ease of modeling rather than for microfabricatability. The design can therefore shed light on how such a unit cell would operate, but should not be viewed as a blueprint for microfabrication.

The design of the conceptual power generating unit cell is shown in Figure 5.3. The spring is a grouping of bundles of CNTs connected between a right-handed screw and a left-handed screw. In this conceptual model, the attachments between the CNT grouping and the end of the screws are considered to be sufficiently strong to withstand the force from the fully stretched spring without fracture occurring at the points of attachment. The attachment is assumed to evenly distribute the load among all tubes within the grouping. Energy is stored in the system by rotating both screws at once, stretching the CNTs in pure tension. Two screws with opposite handedness are used so that the linear extension and contraction of the spring can be converted into a rotation without applying torsion to the spring. An escapement mechanism is implemented to control the release rate of energy from the spring using an escape wheel, a pallet, and a pair of cantilevers as the oscillator. In this design, the escapement is the coupling mechanism between the storage element and the generator since its purpose is to convert the energy released from the spring into a form acceptable for input into the generator. Once the spring is fully stretched, the energy is stored in the system by latching the two screws in place to prevent them from both rotating and translating. To discharge the energy from the spring, the latching on the screws is changed so that the screws can translate but still cannot rotate. This latching mechanism allows the escape wheel to spin while preventing the screws from doing so. The force from the spring acting on the screw threads of the escape wheel drives the escape wheel to spin. As the escape wheel spins, the spring contracts. Without any additional mechanisms, the escape wheel would accelerate and release all of the energy from the spring in a single burst. The role of the pallet is to control the rotations of the escape wheel. The motion of the pallet is driven by the pair of identical cantilever beams that oscillate at their resonant frequency and have a phase difference of 180 degrees. As the pallet oscillates, it alternately locks the escape wheel in place and then allows it to rotate by a small increment. The interlocking motion of the pallet and escape wheel is the same as the motion described in Figure 5.2 (b). The escape wheel is locked in place when an escape wheel tooth is in contact with a locking face of the pallet. As the pallet continues its oscillation, an escape wheel tooth comes in contact with an impulse face on the pallet, and the escape wheel is free to rotate. When the escape wheel rotates, it transfers elastic strain energy from the spring through the

pallet to the cantilever beams. The energy received by the cantilever beams during each impulse allows the beams to maintain oscillations with large amplitudes over an extended period of time despite damping losses that would otherwise cause the oscillations to die out rapidly. The two cantilevers are coated by a film of piezoelectric material with patterned electrodes above and below it. The structure of a piezoelectric bender that operates in the 31 mode is shown in Figure 5.4. A mechanical stress in the cantilever beam in the 1 direction induces a voltage in the 3 direction. As the cantilevers oscillate, the piezoelectric layer converts the stress in the beams into electrical energy. The electrical energy is removed from the system using the electrodes contacting the piezoelectric material.

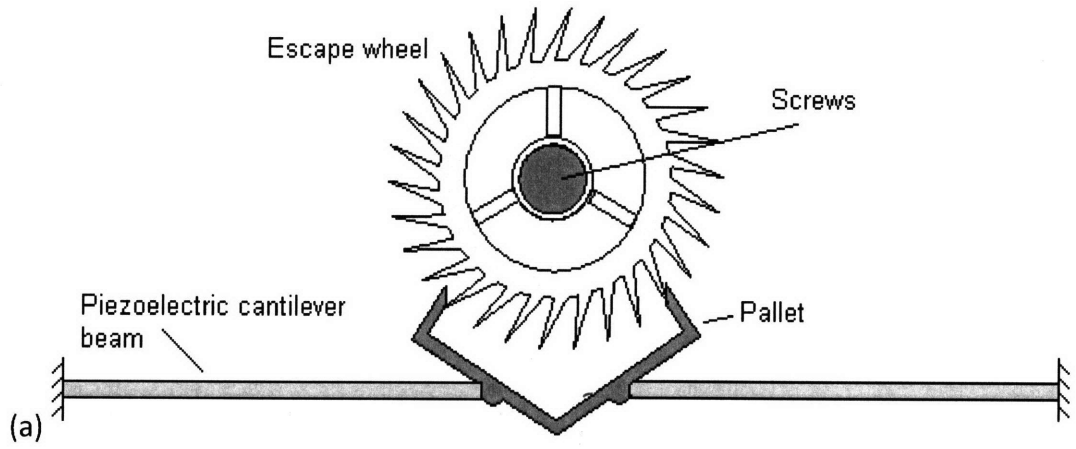

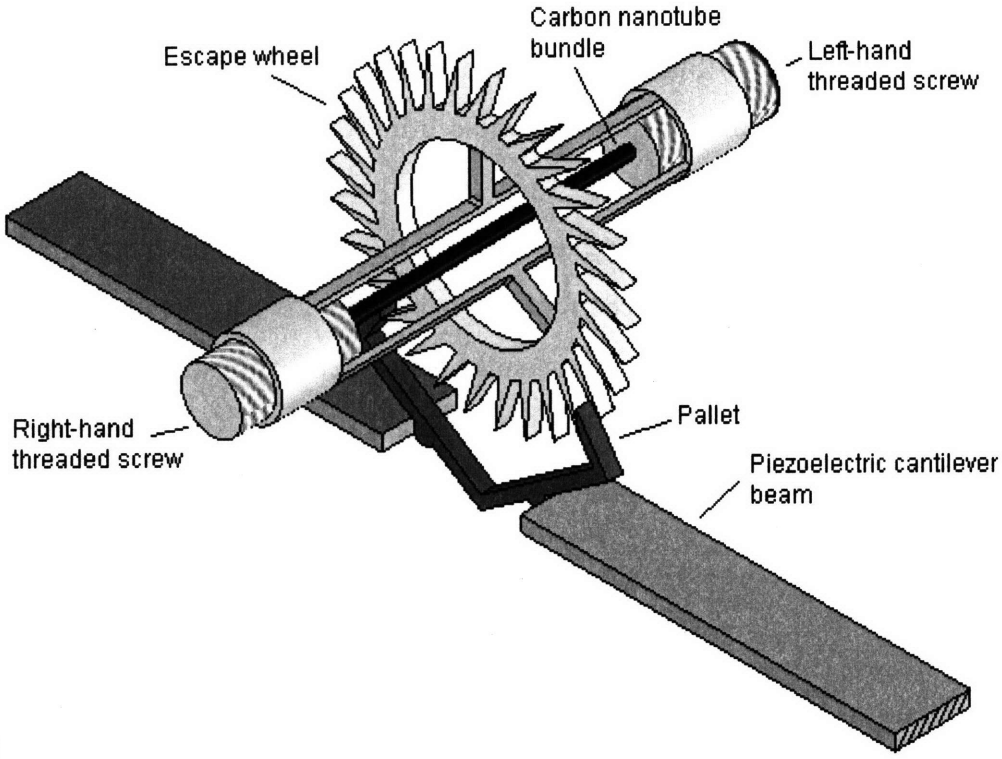

(b)

Figure 5.3: Schematic diagram of a conceptual power generating unit cell in (a) front view and (b) isometric view.

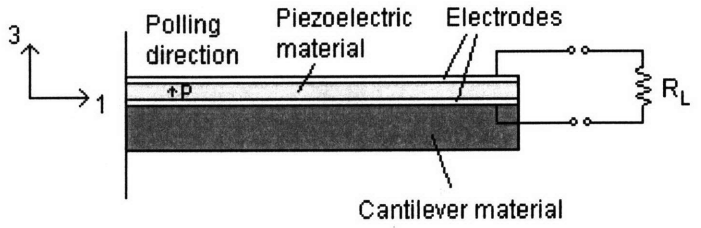

Figure 5.4: Unimorph piezoelectric cantilever beam operating in 31 mode.

The system is designed to be reversible. In the normal mode of operation of an escapement, a moment acting on the escape wheel in the clockwise direction drives the motion of the pallet. However, if it is the pallet that is driven instead, the oscillations of the pallet drive the escape wheel in the counter-clockwise direction. Referring to Figure 5.4, in the charging mode of operation, an alternating voltage applied in the 3 direction to the piezoelectric cantilevers induces alternating tensile and compressive stresses in the 1 direction, which drives the cantilevers to oscillate. The oscillations of the cantilevers drive the motion of the pallet, which

in turn rotates the escape wheel in the counter-clockwise direction. This operation stretches the spring and puts energy into the system for storage. Unimorph cantilevers have been chosen for the design for their ability to have large displacements, which is useful in the discharging mode of operation. In the charging mode of operation, large forces as well as large displacements are needed for the cantilever beams to overcome the forces from the spring, but piezoelectric bending actuators typically can generate only small forces [120]. The maximum forces required of the cantilever beams and the required applied voltages needed to reach these forces to fully stretch a spring will be examined in more detail in the system model.

In practice, the escapement and screws would not literally be implemented in a microscale device, though they could be built at the millimeter scale. The screws here represent a mechanism to convert linear motion to angular motion with frictional losses. Screws have been included in the model for their analytical simplicity, to facilitate a study of the overall system's operating range and performance, but would be replaced with a MEMS mechanism with comparable functionality in an actual implementation.

Although some of the fabrication challenges in the design can be remedied by appropriate design choices, such as the elimination of screws from a MEMS-scale system, others are fundamental to the device. First, CNTs can be manipulated individually using atomic force microscope probe tips, but simple and reliable techniques for aligning and manipulating CNTs on a large scale are still needed. Second, a strong method of attaching the ends of CNTs to a structure is required for the CNT spring to reach high strains without the point of failure being the attachment site. A third challenge will be creating defect-free CNT assemblies that can reliably and uniformly reach the maximum strains reported to date in experimental work on individual CNTs, as well as extending these limits to approach the theoretically predicted strains. The mechanical properties of CNTs are highly sensitive to defects and impurities which reduce their strength, so CNTs of consistently high purity and low defect density are needed. A final challenge will be to design and successfully implement a small, high quality support structure that carries the load of the stretched CNTs. The structure must be both large enough to carry the load of the CNTs and fabricated with high enough quality to avoid premature failure. While large support structures can be built with relative ease, smaller, high quality

support structures have less of a detrimental impact on overall energy density but present significantly greater fabrication and cost challenges.

The size of the system is flexible. The device can be built at a size scale that is most conducive to system performance, ranging from the microscale to millimeter scale, or above, assuming that sufficiently long CNT springs are available. The system's performance at a range of size scales has been studied using simulations.

5.2.1. Escapement Design

For the design of the escapement mechanism, a dead beat escapement, or Graham escapement, has been adopted since it is commonly used in pendulum clocks and is well understood [117]. The operation and geometry of the deadbeat escapement are described by several sources [115, 121-123]. There are two differences between the deadbeat escapement found in pendulum clocks and the one implemented here: microscale components rather than centimeter scale components, and a pair of cantilever beams forming the oscillator to drive the pallet rather than a conventional pendulum.

First, we will examine the geometry of the pallet and escape wheel in detail. The initial step is to form the escape wheel. First, a circle of radius R is drawn. The radius of the circle can be chosen to be any convenient length. A second circle of radius $3/4R$ is drawn inside the first circle. A radius of the larger circle is drawn. A line is drawn that forms a 6° angle with the radius, passing through the point of intersection between the radius and the outer circle. A second line is drawn that forms a 12° angle with the radius, passing through the same point of intersection. These steps are shown in Figure 5.5 (a). The two angled lines form the first escape wheel tooth. To draw a second tooth, a second radius is drawn 12° from the first radius. Once again, two lines are drawn that make 6° and 12° angles with the radius line, passing through the point of intersection between the radius and the outer circle. These two lines form the second tooth. This process is repeated by rotating the radius each time by 12°, until 30 teeth have been drawn. The completed drawing of the escape wheel is shown in Figure 5.5 (b) with construction lines shown as dotted lines.

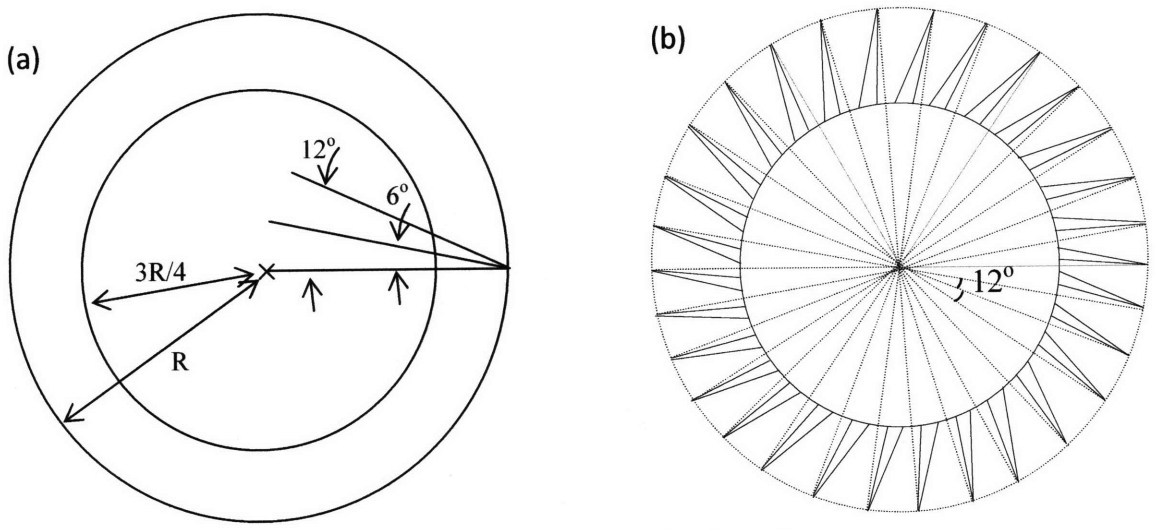

Figure 5.5: Construction lines used to draw the escape wheel teeth.

Once the escape wheel has been drawn, the next step is to add the pallet. A line is drawn through the centre of the escape wheel circle and extended to form a centreline. Two radii of the circle are drawn perpendicular to each other, at 45° angles to the centreline, above and below it. A second circle with a radius of *R* is drawn so that its centre lies on the centreline and it passes through the two points of intersection between the first circle and the two perpendicular radii. The centres of the circles are separated by a distance of $\sqrt{2}R$. Two perpendicular radii of the second circle are drawn to the two points of intersection of the circles. The lines of all four radii are extended for construction purposes. Next, 8 additional lines are drawn that are 3° to either side of the four radii and pass through the centres of the circles. These construction steps are shown in Figure 5.6.

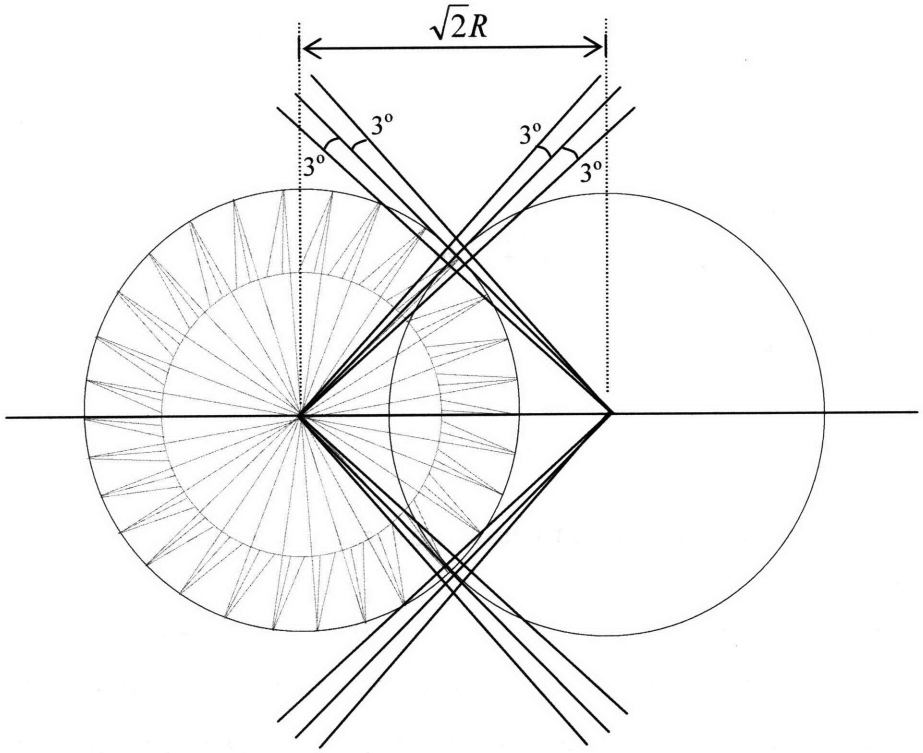

Figure 5.6: Construction lines for drawing the pallet.

To form the locking faces of the pallet, vertical and horizontal lines are drawn through the intersections of these extended lines. Next, two more concentric circles are drawn about the centre of the pallet circle. These two circles have radii lengths of 0.952·R and 1.057·R. A diameter of the pallet circle is drawn perpendicular to the centreline. Two pallet arm construction lines are drawn at an angle of 24° to this diameter through the centre of the circle. An additional two lines are drawn to the right and left of each of the two pallet arm construction lines at a distance of 0.04R, and it is these four lines that form the pallet arms. These steps are shown in Figure 5.7.

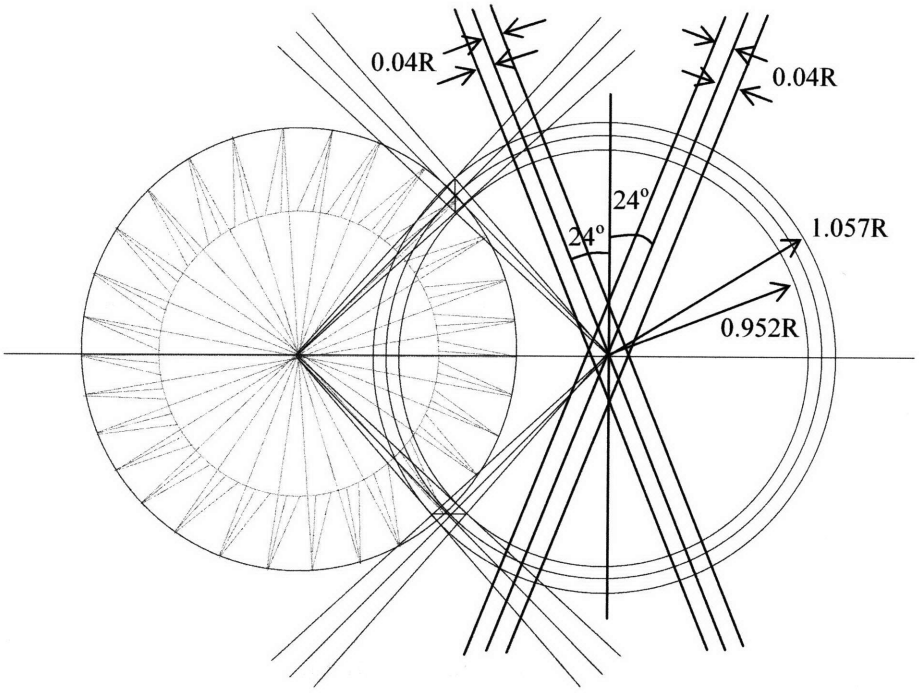

Figure 5.7: Construction lines to form the pallet

The construction of the deadbeat escapement is complete, and the next step is to remove all construction lines. The resulting diagram is shown in Figure 5.8. The final step is to finish the detail on the escape wheel and the pallet. The escape wheel is completed by hollowing out the centre and adding spokes leading outwards. The completed escape wheel and pallet are shown in Figure 5.9.

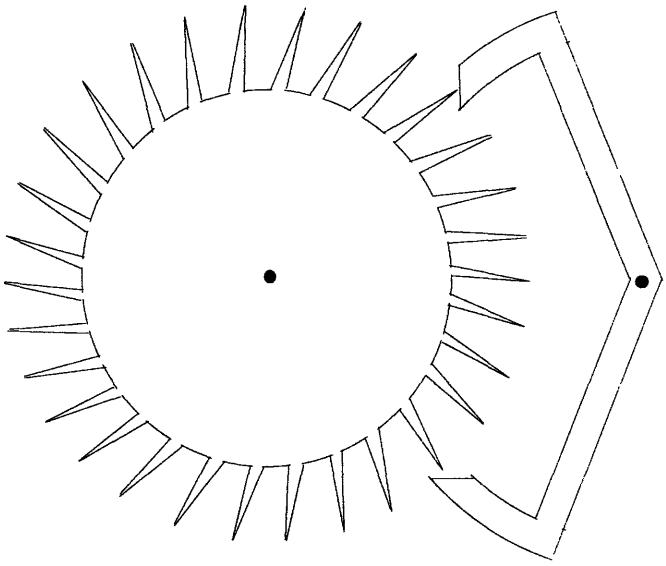

Figure 5.8: Escapement with all construction lines removed.

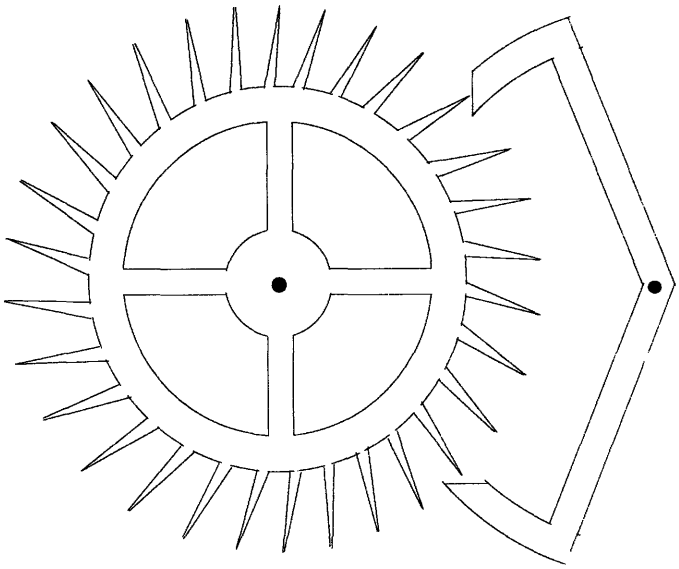

Figure 5.9: Completed drawing of a deadbeat escapement.

5.3. Model and Analysis

5.3.1. System Model

Energy is stored in the spring as elastic strain energy. The spring is assumed to be a grouping of bundles of closely-packed SWCNTs in a hexagonal lattice with a roughly overall circular cross-section, as shown in Figure 5.10. The spacing between adjacent SWCNTs is taken to be 0.34 nm. Treating each SWCNT as a hollow cylinder of thickness 0.34 nm using the continuum approximation, the amount of energy stored in the spring is

$$U = \frac{1}{2} E \varepsilon^2 A_e L, \tag{5.1}$$

where E is the Young's modulus, ε is the applied strain in the spring, A_e is the effective cross-sectional area of the bundle, and L is the length of the bundle. The effective cross-sectional area of the bundle is the area that is filled with solid CNT shells, excluding the hollow centre of the tubes and the space between the tubes,

$$A_e = \pi r^2 k \frac{A}{A_{encl}}, \tag{5.2}$$

where r is the outer radius of the bundle, k is a fill factor to account for the spacing between the SWCNTs in the grouping, A is the cross-sectional area of a SWCNT shell and A_{encl} is the total enclosed cross-sectional area of a SWCNT. The model assumes that the spring is made of SWCNTs in an ideal lattice arrangement as shown in Figure 5.10. The energy in the spring is rewritten as

$$U = \frac{1}{2} E \varepsilon^2 \pi r^2 k \frac{A}{A_{encl}} L. \tag{5.3}$$

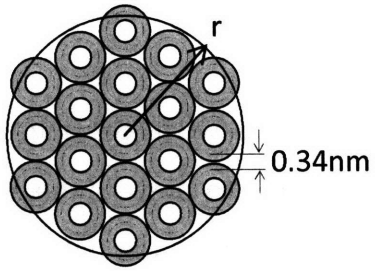

Figure 5.10: Schematic diagram of a CNT grouping cross-section showing each tube as an equivalent continuum structure.

A support structure is needed to support the load of the fully stretched spring. The structure is not shown in Figure 5.3, but its mass can be calculated based on equation (3.15). The mass of the support structure is given by

$$m = \frac{E\varepsilon_{max}}{\sigma_{supp}} \pi r^2 k \frac{A}{A_{encl}} L \rho_{supp} \tag{5.4}$$

where E is the Young's modulus of the CNTs in the spring, ε_{max} is the maximum strain applied to the spring, σ_{supp} is the yield stress of the support structure material, r is the radius of the spring, L is the length of the spring, and ρ_{supp} is the density of the support structure material.

The spring is connected on each end to a screw. When a strain of ε is applied to the spring, the spring exerts a force $F_s = EA_e\varepsilon$ on the two screws, as shown in Fig. 19. This force is distributed over the whole area of the screw threads. When energy is being stored in the system, the screws are in equilibrium and the latches apply forces $F_L = F_s$ to hold the screws in place.

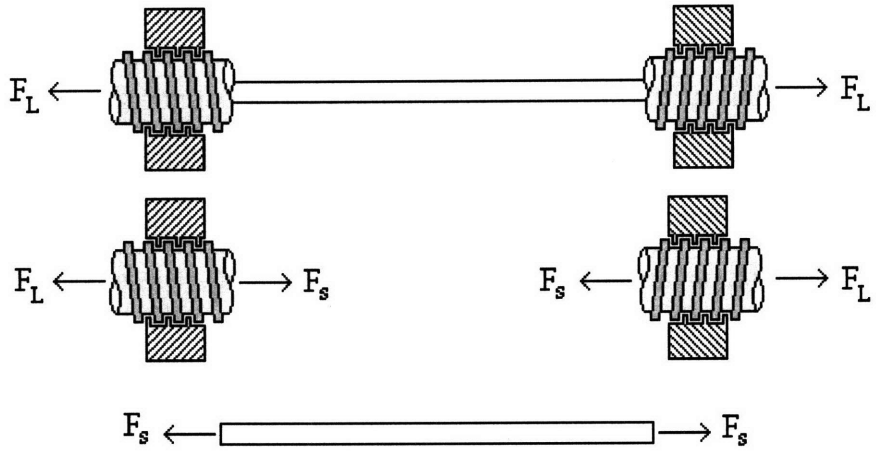

Figure 5.11: Equilibrium forces acting on the stretched spring and the screws.

Once the latches are removed, the two forces F_L are removed and the system is no longer in equilibrium. A mechanism is applied to prevent the screws from rotating, but they can still translate. Since the screws cannot rotate, the only way for the spring to contract is for the escape wheel to rotate. The force from the spring is distributed over the area A_{thread} of the threading in the threaded hole in the escape wheel, as shown in Figure 5.12. Square threaded screws are assumed in the model. The screws have a pitch l, mean screw diameter d_s and

perimeter $\pi \cdot d_s$, as shown in Figure 5.13. Figure 5.14 shows a single unrolled thread of the threading along the hole in the escape wheel with the forces acting on the thread [124]. The net axial force acting on the entire thread surface due to the spring is F_s and N is net normal force from the screw threads acting on the escape wheel threads. The coefficient of friction between the screw threads and the threading surface of the escape wheel hole is μ and the frictional force opposing the motion is F_f. P is an applied force needed to overcome friction and cause the escape wheel to rotate.

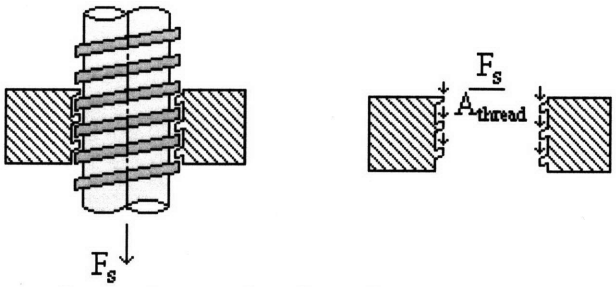

Figure 5.12: The force from the spring is distributed over the area of the threading in the threaded hole of the escape wheel.

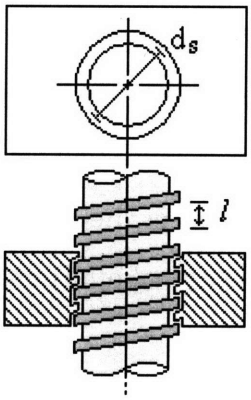

Figure 5.13: Diagram of the square threaded screws used in the model showing the pitch and the mean diameter.

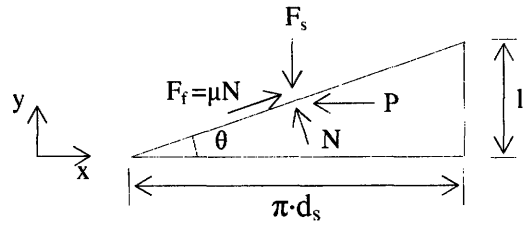

Figure 5.14: Free body diagram of the forces acting on a single unrolled thread of the threaded hole in the escape wheel [124].

For the system in Figure 5.14 to be in equilibrium,

$$\sum F_y = -F_s + N\cos\theta + \mu N\sin\theta = 0 \tag{5.5}$$

$$\sum F_x = \mu N\cos\theta - P - N\sin\theta = 0 \tag{5.6}$$

Eliminating the normal force *N* and substituting in the relation $tan\theta = l/(\pi d_s)$

$$P = \frac{F_s(\pi d_s\mu - l)}{\pi d_s + \mu l} = EA_s\varepsilon\frac{(\pi d_s\mu - l)}{\pi d_s + \mu l} \tag{5.7}$$

When the pitch is large or the coefficient of friction is small, *P* becomes negative. In this case, the escape wheel will rotate without any applied external forces, and a force *P* acting in the positive x-direction is needed to prevent the screw from unwinding on its own. When no external force *P* is applied, the system is no longer in equilibrium and the magnitude of *P* represents the net horizontal force that causes the escape wheel to rotate. For this design, the escape wheel must rotate without any external effort and a negative value of *P* is required, so the condition $\pi d_s\mu < l$ must be satisfied.

The moment acting on the escape wheel from one screw is the product of *P* and the radius of a screw, $d_s/2$, the distance between the applied force and the axis of rotation. Since there are two screws, the total moment on the escape wheel is multiplied by two. During operation, as the spring contracts, the magnitude of the moment is a function of the strain in the spring,

$$M(\varepsilon) = EA_s\varepsilon d_s\frac{(l - \pi d_s\mu)}{\pi d_s + \mu l} \tag{5.8}$$

The efficiency of the screws is equal to the moment on the escape wheel with friction present divided by the moment on the escape wheel when there is no friction, setting $\mu=0$,

$$\eta_{screw} = \frac{\pi d_s}{l} \frac{(l - \pi d_s \mu)}{\pi d_s + \mu l} \tag{5.9}$$

A plot of screw efficiency as a function of l/d_s in Figure 5.15 shows that a maximum efficiency can be reached by choosing an optimal value of l/d_s. Both the optimal value of l/d_s and the maximum efficiency depend on the coefficient of friction. With μ=0.05, the maximum efficiency of 90% occurs at l=3.3d_s. A low coefficient of friction is needed to achieve high screw efficiency. A lubricant applied along the contact area between the screw threads may help to reduce the friction.

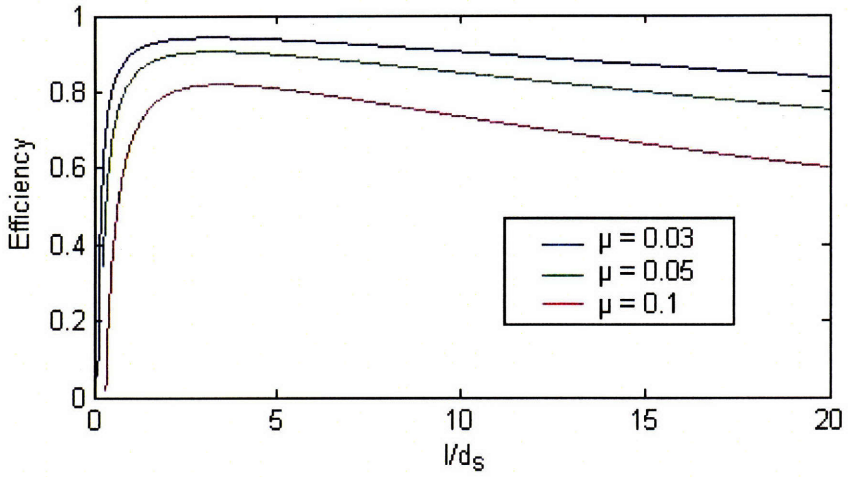

Figure 5.15: The screw efficiency η_{screw} plotted as a function of l/d_s with different values of the coefficient of friction.

The graph in Figure 5.15 shows that a relatively large screw pitch is needed to achieve the highest screw efficiency. Even with a low coefficient of friction of 0.05, the pitch must be 3.3 times greater than the diameter of the screw to reach 90% efficiency. As the pitch gets smaller with respect to the diameter, the efficiency drops off rapidly. A small pitch is preferable for operation of the power source because each incremental rotation of the screw during an impulse should allow the spring to contract by only a small amount, so that the spring returns to its original length with more escape wheel rotations. A greater number of escape wheel rotations results in a longer overall discharge time and provides more control over the rate of energy release from the spring, since a smaller amount of energy is released from the spring with each pallet oscillation. As a result, there is a tradeoff when selecting the pitch of the screw,

which should be carefully designed by considering the energy release rate, discharge time and efficiency that are required of the power source.

A similar analysis of the screws is done to study the efficiency of winding the screws to stretch the spring. The diagram in Figure 5.16 shows a single unrolled thread of one of the screws with the forces that act on it [124]. There is a net axial spring force F_s acting on the entire thread surface, a friction force F_f opposing the motion, a net normal force N from the threads in the escape wheel acting on the screw threads, and an applied force P needed to overcome friction and wind the screws. For the system to be in equilibrium, the sum of the forces in the x- and y-directions is 0. Eliminating the normal force N and using the relation that $\tan\theta = l/(\pi d_s)$, one obtains

$$P = \frac{F_s(l + \mu\pi d_s)}{\pi d_s - \mu l} \tag{5.10}$$

The applied moment required to wind each screw is the product of P and radius of the screw, $d_s/2$. Since there are two screws, the total moment required to wind both screws is multiplied by two,

$$M = F_s d_s \frac{(l + \mu\pi d_s)}{\pi d_s - \mu l} = EA_s \varepsilon d_s \frac{(l + \mu\pi d_s)}{\pi d_s - \mu l} \tag{5.11}$$

The efficiency of winding the screws to stretch the spring is equal to the moment required to wind the screws if there were no friction present, setting μ=0, divided by the moment with friction,

$$\eta_{wind} = \frac{l}{d_s\pi} \frac{(\pi d_s - \mu l)}{\pi d_s \mu + l} \tag{5.12}$$

In order to store energy U in the spring, a larger amount of energy U/η_{wind} must be supplied to the system due to frictional losses during winding. While the value of l/d_s is chosen to meet performance conditions during the unwinding phase rather than to optimize winding efficiency, η_{wind} can be kept high with a low value of the coefficient of friction.

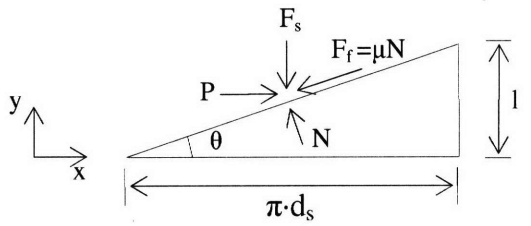

Figure 5.16: Free body diagram of the forces acting on a single unrolled thread of a screw during winding [124].

The fully stretched spring has a starting strain of ε_{max}. During operation, the escape wheel rotates and the spring contracts until it returns to its original length. For every rotation of escape wheel of 2π radians, the spring contracts by $2l$, where l is the pitch of the screw threading. The strain ε in the CNT grouping during operation is a function of the angle θ that the escape wheel has rotated:

$$\varepsilon = \varepsilon_{max} - \frac{\theta l}{\pi L} \text{ for } \frac{\theta l}{\pi L} < \varepsilon_{max}, \text{ and } \varepsilon = 0 \text{ otherwise,} \tag{5.13}$$

where L is the unstretched length of the spring. At any time during operation, the number of times that the escape wheel has rotated is $\theta/(2\pi)$. The total number of escape wheel rotations for the spring to unwind completely is $\varepsilon_{max}L/(2l)$.

The next step is to model the escape wheel, pallet and cantilever beams. The geometry of the pallet and the two cantilever beams is shown in Figure 5.17. The pallet arms have length R. The cantilevers are placed underneath the pallet arms and contact each arm at its midpoint. In the neutral position, the tips of the cantilevers contact the pallet at a vertical height of h_o and a horizontal distance of b_o from the centre of rotation of the pallet. In the neutral position, the pallet arm forms an angle θ_o with the horizontal axis so that $b_o = \frac{r}{2}cos\theta_o$ and $h_o = \frac{r}{2}sin\theta_o$. The design requires that the pallet and the cantilever tip displace together so that the cantilever drives the motion of the pallet. Maintaining a connection between the pallet arm and the cantilever tip is also important so that the cantilever can receive the impulses from the pallet on both the upward and downward motion of the pallet. When a pallet arm is moving downwards, it will press down on the tip of the cantilever beam, constraining the cantilever tip to move with the pallet. When a pallet arm is moving upwards, an additional component is

required to constrain the tip of the cantilever to move with the pallet. Such a component requires careful design in an actual implementation, but in this conceptual model it is represented by a small block on the underside of the pallet arm placed below the point of contact in the neutral position. The angle of displacement of the pallet with respect to its neutral position is denoted $\theta_p(t)$ and the tip displacement of the cantilever beam is denoted $x(t)$, where both are functions of time, and these two variables are related with a simple approximation. Using the geometry of Figure 5.17, the pallet angle and cantilever tip displacement are related by

$$\theta_p(t) = \tan^{-1}\left(\frac{h_o + x(t)}{b_o}\right) - \theta_o \qquad (5.14)$$

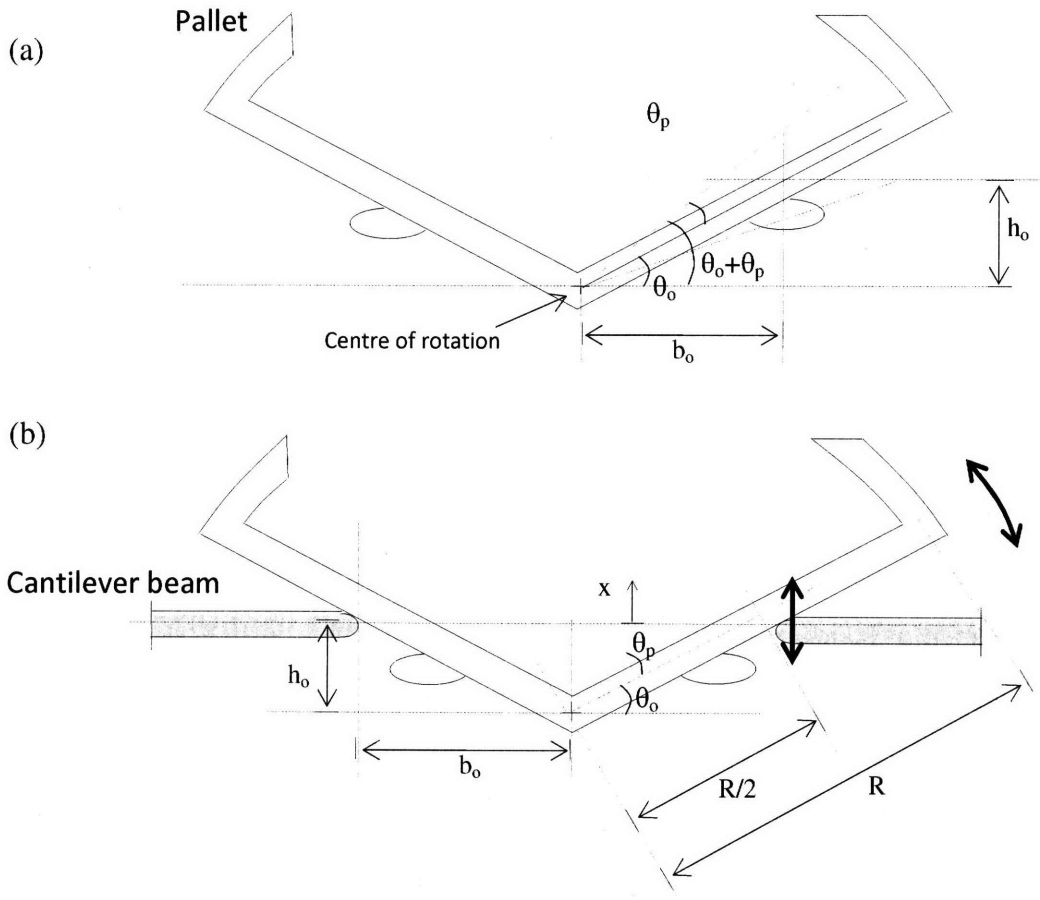

Figure 5.17: (a) Geometry of the pallet. (b) Diagram showing the geometry and connection between the pallet and the cantilever beams, the pallet angle θ_p and the cantilever displacement x.

Together, the escape wheel, pallet and cantilever beams form a mass-spring-damper system. The spring functionality is provided by the two cantilever beams. Damping in the system is a result of mechanical losses and the piezoelectric conversion of energy from the mechanical to the electrical domain. The overall damping coefficient is modeled as a sum of the mechanical damping coefficient b_m and the electrical damping coefficient b_e. The mass functionality comes from the inertia of the cantilevers, pallet and escape wheel. Finally, the spring provides the driving force in the system which is transferred to the mass through the escape wheel mechanism.

Each beam is modeled as a tip loaded cantilever. The cantilevers have length *L*, height *H* and width *W*. The effective mass m_{eff} of each cantilever is calculated as $m_{eff} = \frac{33}{140} \cdot m_{beam}$, where $m_{beam} = \rho \cdot LWH$ is the actual mass of the cantilever beam and ρ is the density of the material of the cantilever. A spring constant of $k = \frac{EWH^3}{4L^3}$ is assigned to the cantilevers, where *E* is the Young's modulus of the cantilever material.

The three free body diagrams in Figure 5.18 show the forces acting on the escape wheel, pallet and cantilevers while an impulse is taking place. As defined previously, θ_p is the angle of rotation of the pallet with respect to its neutral position and *x* is the vertical displacement of the cantilever tip. θ_w is the total angle of rotation of the escape wheel with respect to its starting position prior to the release of the spring. During an impulse, a tooth of the escape wheel pushes against the impulse face of the pallet, and the contraction of the spring drives the escape wheel to rotate. The pallet and escape wheel both rotate by an angle of 6° during an impulse, by design of the escapement. The escape wheel and pallet are constrained to move together, so they must have the same angular velocity and acceleration. In the free body diagram of the escape wheel, E_x and E_y are the reaction forces at the escape wheel's pivot at point E. *M* is the moment driving the escape wheel to rotate due to the spring. F_p is the normal force exerted by the pallet on the escape wheel tooth. In the free body diagram of the pallet, P_x and P_y are reaction forces at pallet's pivot at point P, F_p is the force exerted by the escape wheel tooth on the pallet impulse face, and F_{c1} and F_{c2} are the forces exerted by the cantilever beams

on the pallet. In the free body diagram of the cantilever, F_{c1} is the force exerted by the pallet on the cantilever and F_k and F_b represent the damping and spring forces acting on the cantilever.

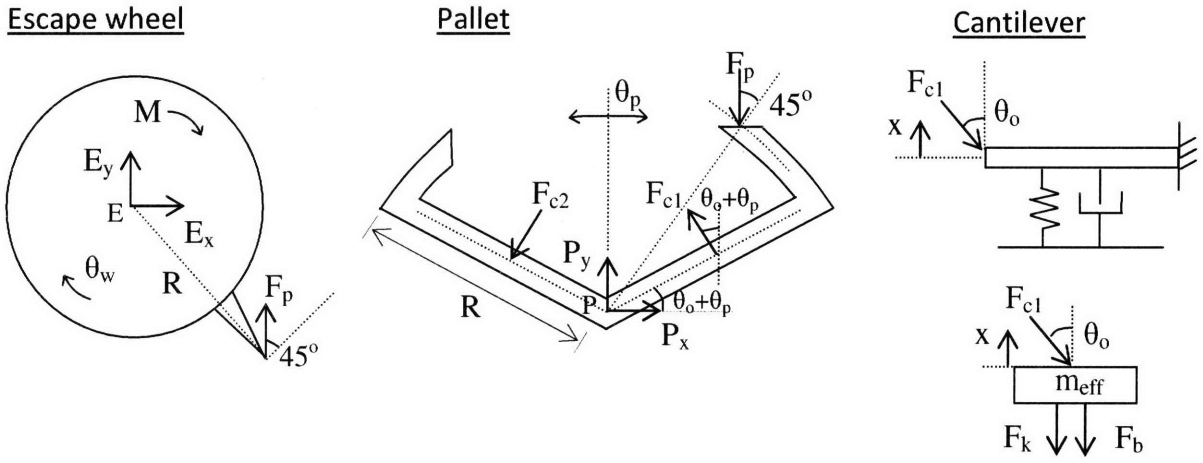

Figure 5.18: Free body diagrams showing the forces acting on the escape wheel, pallet and cantilevers during an impulse.

The following equations are obtained from the free body diagrams:

$$\text{Wheel: } \sum M_R = -F_p R\cos 45 + M = I_w \ddot{\theta}_w \tag{5.15}$$

$$\text{Pallet: } \sum M_P = F_p R\cos 45 - F_{c1}\frac{R}{2} - F_{c2}\frac{R}{2} = I_p \ddot{\theta}_p \tag{5.16}$$

$$\text{Cantilevers: } \sum F_x = -kx - (b_m + b_e)\dot{x} - F_{c1}\cos(\theta_o + \theta_p) = m_{eff}\ddot{x} \tag{5.17}$$

Since the escape wheel and pallet have the same angular velocity and acceleration during an impulse, $\dot{\theta}_w = \dot{\theta}_p$ and $\ddot{\theta}_w = \ddot{\theta}_p$. Combining these three equations, the equation of motion of the escape wheel, pallet and cantilevers during an impulse is:

$$m_{eff}\ddot{x} + (b_m + b_e)\dot{x} + kx = [M - (I_w + I_p)\ddot{\theta}_w]\frac{\cos(\theta_o + \theta_p)}{R} \tag{5.18}$$

where $\theta_p(t) = \tan^{-1}(\frac{h_o + x(t)}{b_o}) - \theta_o$.

A locking phase occurs between impulses. During a locking phase, an escape wheel tooth is in contact with the locking face of the pallet, so that the escape wheel cannot rotate. The free body diagrams in Figure 5.19 show the forces acting on the escape wheel, pallet and cantilevers

during this phase. The reaction force F_p on the escape wheel tooth from the locking face of the pallet produces a moment that balances the moment on the escape wheel from the spring so that the escape wheel is locked in place and prevented from rotating. The force from the escape wheel tooth on the locking face of the pallet acts in the direction of point P, the pallet's pivot, so this force has no effect on the pallet's motion. It is assumed that the effects of friction between the escape tooth tip and the locking face of the pallet are negligible in the simplified analysis. During this phase, the escape wheel is fixed in place while the pallet and the tip of the cantilever beams displace together.

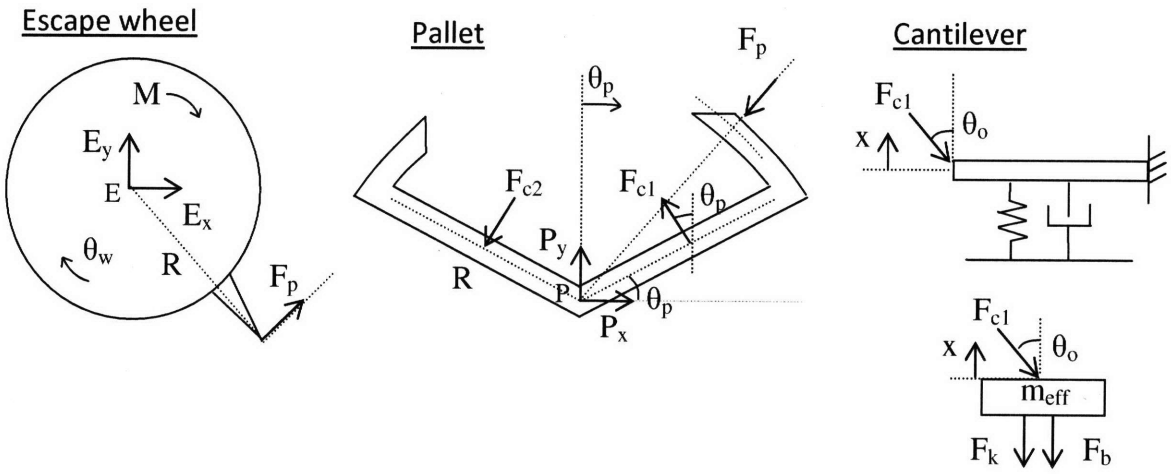

Figure 5.19: Free body diagrams showing the forces acting on the escape wheel, pallet and cantilevers between impulses.

The following equations are obtained from the free body diagrams.

$$\text{Wheel: } \sum M_R = -F_p R + M = 0 \tag{5.19}$$

$$\text{Pallet: } \sum M_P = F_p R\cos 90 - F_{c1}\frac{R}{2} - F_{c2}\frac{R}{2} = I_p\ddot{\theta}_p \tag{5.20}$$

$$\text{Cantilevers: } \sum F_x = -kx - (b_m + b_e)\dot{x} - F_{c1}\cos(\theta_o + \theta_p) = m_{eff}\ddot{x} \tag{5.21}$$

Combining these three equations, the equation of motion of the pallet and cantilever during the locking phase is:

$$m_{eff}\ddot{x} + (b_m + b_e)\dot{x} + kx = -I_p\ddot{\theta}_p\frac{\cos(\theta_o + \theta_p)}{R} \tag{5.22}$$

where $\theta_p(t) = \tan^{-1}(\frac{h_o + x(t)}{b_o}) - 30^o$ and $\dot{\theta}_w = 0$.

With this particular escapement design, an impulse will take place for $-3^o < \theta_p < 3^o$. For $\theta_p > 3^o$ and $\theta_p < -3^o$, the escape wheel is locked in place and the pallet oscillates freely. To summarize, the motion of the pallet is described as

$$m_{eff}\ddot{x} + (b_m + b_e)\dot{x} + kx = -I_p\ddot{\theta}_p \frac{\cos(\theta_o + \theta_p)}{R} + U(\theta_p)\cdot[M - I_w\ddot{\theta}_w]\frac{\cos(\theta_o + \theta_p)}{R} \qquad (5.23)$$

where $U(\theta_p) = 1$ for $-3^o < \theta_p < 3^o$, and $U(\theta_p)=0$ otherwise.

The moment of inertia of the pallet I_p and escape wheel I_w are needed to implement the model. Both components are given a depth of d. The mass of the escape wheel is approximated as

$$m_w = \rho\pi[R^2 - (0.75R)^2]d \cdot 1/4 + \rho\pi[(0.75R)^2 - (0.625R)^2]d\,, \qquad (5.24)$$

and the moment of inertia of the escape wheel is modeled as

$$I_w = \frac{1}{2}m_w[(0.75R)^2 + (0.625R)^2]\,, \qquad (5.25)$$

where ρ is the density of the material of the pallet and escape wheel and R is the outer radius of both the escape wheel and pallet. To calculate the moment of inertia of the pallet, it is separated into two components: the two pallet arms, each with a mass of

$$m_{p1} = \rho R \cdot 0.08Rd\,, \qquad (5.20)$$

and the two pallet teeth, with a mass of

$$m_{p2} = 1/15\rho\pi[(1.05R)^2 - (0.95R)^2]d\,. \qquad (5.26)$$

The total mass of the pallet is $m_p = 2m_{p1} + m_{p2}$. The moment of inertia of the pallet is modeled as

$$I_p = 2\frac{1}{3}m_{p1}R^2 + \frac{1}{15}\frac{1}{2}m_{p2}[(1.05R^2) - (0.95R^2)]\,. \qquad (5.27)$$

The total mass of the device is sum of the masses of the CNT spring, pallet, escape wheel, cantilever beams, screws and the support structure. The percentage of CNTs by mass in the overall system is the mass of the spring divided by the total mass of the device.

The frequency of operation of the system f depends on the effective mass and spring constant of the cantilever beams, the moments of inertia of the pallet and escape wheel and the mechanical and electrical damping in the system. An exact value of the system's frequency is generated by the Simulink model.

Damping can vary considerably depending on the load driven by the piezoelectric generator and the detailed structure of the beam. To capture the effects of these differences, ranges of damping coefficients are considered. The mechanical damping b_m cannot be known precisely without measuring the performance of the actual system, but it can be approximated using values for the quality factor of cantilever beams reported in the literature. The electrical damping coefficient b_e is calculated as

$$b_e = 2m\zeta_e w \tag{5.28}$$

where

$$\zeta_e = \frac{wk_{31}^2}{\sqrt{w^2 + 1/(R_L C)^2}} \tag{5.29}$$

is the electrical damping ratio [111], C is the capacitance of the piezoelectric layer, R_L is the external load resistance, and w is the angular frequency of the cantilever oscillations. The electromechanical coupling factor k_{31} is expressed as [111]

$$k_{31}^2 = \frac{d_{31}^2}{\varepsilon_{33}^T s_{11}^E} \tag{5.30}$$

where d_{31}^2 is the piezoelectric constant, ε_{33}^T is the dielectric constant and s_{11}^E is the mechanical compliance of the piezoelectric material. The capacitance of the piezoelectric layer C is calculated from

$$C = \frac{\varepsilon_{33}^T A_p}{t} \tag{5.31}$$

where A_p is the area of the piezoelectric layer and t is its thickness. The electrical damping coefficient b_e depends on the parameters of the electrical circuit and the load driven by the generator, so a suitable circuit can be designed by choosing an appropriate load resistance to adjust the value of b_e. A range of values for the electrical damping coefficient is considered by varying the magnitude of the load resistance R_L driven by the piezoelectric circuit.

Using a simplified model for piezoelectric power generation [110, 111], the electrical power generated by a single piezoelectric cantilever beam is equal to the power removed from the mechanical system due to the electrical damping,

$$P = \frac{1}{2} b_e \dot{x}^2 . \tag{5.32}$$

Since there are two cantilever beams, the total output power of this device is multiplied by two. The total energy extracted from the system using the cantilever beams over the duration of operation is

$$E = 2 \cdot \int_{t_{start}}^{t_{end}} \frac{1}{2} b_e \dot{x}^2 dt . \tag{5.33}$$

Models of clock escapements show that if the frictional losses and the driving force of the impulses are constant, then the oscillator will settle down to have constant amplitude and be stable to external disturbances [116, 117]. In this device, the driving force on the cantilevers will decrease linearly with time since it is linearly dependent on strain, so the amplitude of the cantilever oscillations will vary over time.

Once energy is stored in the spring, three main sources of losses reduce the amount of energy that can be extracted from the system: the frictional losses in the screws, losses inherent to the escapement mechanism, and losses in the piezoelectric energy conversion. Additional losses to friction in the system may be present but have not been included in this conceptual model. The overall efficiency of the system η is expressed as the total energy removed from the system by the piezoelectric cantilevers divided by the starting energy in the spring U:

$$\eta = \frac{2 \cdot \int_{t_{start}}^{t_{end}} \frac{1}{2} b_e \dot{x}^2 dt}{U} . \tag{5.34}$$

To run the system in reverse and wind the spring, a voltage is applied to the piezoelectric cantilevers to drive their oscillations. For a unimorph cantilever subject to an applied external force F at the tip and an applied voltage V, the tip displacement δ is [120]

$$\delta = aF + bV \tag{5.35}$$

where

$$a = \frac{4s_{11}^E L^3}{Wt_p^3} \frac{AB+1}{1+4AB+6AB^2+4AB^3+A^2B^4} \tag{5.36}$$

$$b = \frac{3d_{31}L^2}{t_p^2} \frac{AB(B+1)}{1+4AB+6AB^2+4AB^3+A^2B^4} \tag{5.37}$$

$A = \frac{E_m}{E_p}$, $B = \frac{t_m}{t_p}$, L is the beam length, W is the beam width, t_m is the thickness of the cantilever substrate layer, t_p is the thickness of the piezoelectric layer, E_m is the Young's modulus of the substrate layer and E_p is the Young's modulus of the piezoelectric layer. For the pallet to drive the escape wheel, the cantilevers must be able to displace a known distance δ while supporting a large force applied to the tip of the beam acting in the opposite direction. The largest force that the cantilever beam must generate to fully recharge the system is

$$F_{c,max} = \frac{M_{max}}{R\,cos45^\circ}, \tag{5.38}$$

where M_{max} is the moment on the escape wheel with the fully stretched spring. As the spring becomes stretched, the voltage required to drive the pallet will increase over time as the strain in the spring increases, up to a maximum voltage V_{max} once the spring reaches its highest strain. The maximum voltage required to displace the cantilever tip by δ while supporting a load $F_{c,max}$ is

$$V_{max} = \frac{\delta + aF_{max}}{b}. \tag{5.39}$$

5.3.2. Design constraints

All of the parameters in the design must be selected prior to running a simulation. The overall scale of the system is flexible and dimensions can be selected accordingly. Parameters can be adjusted to meet a particular specification, such as efficiency, operating frequency or magnitude of energy storage. The choices that must be made include the dimensions of the screws, cantilevers, pallet and escape wheel, the materials of all components, the composition and size of the spring, the friction in the screws and the mechanical and electrical damping. The complete list of parameters is given in the Matlab file parameters.m in Appendix 2. While the

design does allow some degree of flexibility in terms of parameter selection, a number of constraints apply to the parameters to obtain acceptable performance and proper functioning.

A good guideline when selecting the dimensions of the escape wheel, pallet and cantilevers is to keep these components small relative to the size of the spring to maintain a high percentage of CNTs in the system for high overall energy density.

Stresses in the device should not lead to the fracture of any component. The highest stresses are found in the cantilever beams and escape wheel gear teeth, and these stresses must not exceed the yield stress σ_y of the material. If the maximum tip displacement of the cantilever is δ, then

$$\sigma_{max} = \frac{3}{2}\frac{HE}{L^2}\delta \tag{5.40}$$

which must be less than the yield stress. Each gear tooth of the escape wheel is modeled as a cantilever beam with a length L_t of $R/4$, a width W_t equal to the thickness of the escape wheel, and a height H_t of $\pi R/40$. The largest force $F_{p,max}$ applied to the tip of a tooth occurs during the locking phase at the start of operation when the spring is fully extended. The maximum stress is found at the base of the gear tooth and has a magnitude of

$$\sigma_{\max} = \frac{6L_t}{H_t^{\,2}W_t}\frac{EA_s\varepsilon_{\max}d_s}{R}\frac{(\pi d_s\mu + l)}{\pi d_s - \mu l} \tag{5.41}$$

This value must not exceed the yield stress of the material of the escape wheel, and so the dimensions of the escape wheel, the screws and the spring must be selected accordingly.

Another design constraint applies to the inertia of the escape wheel. The resonance frequency of the cantilever beams determines the frequency of the pallet oscillations. The moment from the spring must be able to accelerate the escape wheel from rest to rotate 6 degrees during the time of an impulse. If the inertia of the escape wheel is too large and the wheel cannot rotate 6 degrees during an impulse, the mechanism will fail because the precise interlocking mechanism of the pallet and the escape wheel will become unsynchronized. A small escape wheel inertia ensures proper functioning of the mechanism. Since inertia scales with the fifth power of the linear dimension of an object, reducing the scale of the wheel is advantageous. In addition, overall efficiency of the device is reduced because energy from the spring is needed to drive the motion of the escape wheel and pallet, so keeping the escape

wheel and pallet small helps to reduce these losses. The degree to which the escape wheel can be reduced in size is limited by the stresses in the gear teeth, which increase as the escape wheel gets smaller, for a given magnitude of the impulse forces.

Ensuring that the escape wheel can complete its rotation in the given time can also be done by keeping the resonant frequency of the cantilevers low. The resonant frequency of the cantilevers depends on the dimensions and materials of the cantilevers, the escape wheel and the pallet. In the general case of a simple cantilever, the resonance frequency $f = \frac{t}{4\pi L^2}\sqrt{\frac{140}{33}\frac{E}{\rho}}$ scales with the inverse of the linear dimension of the cantilever, so a cantilever oscillates faster as it gets smaller. A similar trend was observed from simulations of this model, with the resonant frequency scaling roughly with the inverse of the linear dimension of the overall system. Faster cantilever oscillations give the escape wheel less time to complete its required rotation during an impulse, so a good design guideline is that once the size of the pallet and escape wheel have been fixed, the dimensions of the cantilevers should be large within the scale of the system to maintain a relatively low oscillation frequency. Of course, larger cantilever beams reduce the energy density of the overall system.

The oscillation frequency of the cantilever beams affects the rate of energy release from the spring. Two impulses occur during each pallet oscillation, so energy is released twice for each time period of the pallet. With a frequency in kHz or MHz, energy will be released in a time scale on the order of milliseconds and microseconds respectively. A slower oscillation frequency helps to lengthen the discharge time of the spring, which is the purpose of the escapement and one of the main objectives of the design.

Due to the escapement design, the angle of oscillation of the pallet θ_p must not exceed 9 degrees. If the angle is above the limit, a pallet tip will collide with the escape wheel and the mechanism will cease to function. This places a constraint on the oscillation amplitude of the cantilevers which drive the pallet. The dimensions and material of the cantilevers must be chosen so that their oscillation amplitude is acceptable for a given set of impulse forces and mechanical and electrical damping. Large cantilevers with higher stiffness are needed to handle large impulse forces from springs with large diameters. A smaller screw pitch can reduce the magnitude of each impulse force, but this is done at the expense of efficiency.

The cross-sectional area of the spring should be large relative to the scale of the device to maximize energy storage. The spring must have a sufficiently large diameter so that the energy released during an impulse is capable of driving the escape wheel and the pallet. However, a larger cross section means more energy is released in a single impulse, and the magnitude of this energy is constrained by the limits on the oscillation amplitude of the cantilevers. A larger cross-section also means higher stresses on the escape wheel gear teeth. The size of the spring must be carefully chosen as a compromise between these constraints.

The diameter of the screws is chosen to be on a scale compatible with the rest of the system. The choice of the pitch is a tradeoff between efficiency and performance. For a coefficient of friction of 0.05, the maximum efficiency of 90% occurs at $l = 3.3d_m$. A smaller pitch has a lower efficiency but it offers more escape wheel rotations, smaller increments of energy released in each impulse, more impulses, and a longer discharge time, all desirable performance characteristics.

These constraints combine to create a set of interdependent parameters that are restricted to a relatively narrow range of acceptable values. All of the conditions must be met for the escapement mechanism to function properly.

General steps are recommended for selecting the dimensions and materials of a device. The first step is to choose the general scale of the system. Next, the length and diameter of the spring are chosen. The diameter and depth of the escape wheel are selected to be compatible with the diameter of the spring. The size of the escape wheel must be sufficiently small so that it can be driven to rotate by the spring without too much energy loss, but large enough that the stresses in the gear teeth do not exceed the maximum allowable stress. The screw diameter and pitch are chosen as a compromise between efficiency and regulation of energy release. Finally, cantilever dimensions and materials are selected so that the cantilevers are sufficiently large to drive the motion of the pallet, have an acceptable oscillation amplitude under the impulse forces from the spring, and have acceptable maximum stresses.

5.3.3. Simulink model

The simulation is set up in Simulink using equations to model each of the components of the system: the CNT-based spring, the escape wheel, the pallet, and the cantilever piezoelectric generators. A sample input file containing the parameters for the model, parameters.m, is found in Appendix 2. The Simulink model unitcell.mdl is shown in Appendix 3.

5.4. Simulation Results

Simulations are run for systems at different scales to determine the effect of scaling on the stored energy, operating frequency, power output and efficiency. Three cases are presented here of systems that are designed at the micron-scale, the submillimeter-scale and the millimeter-scale, with all dimensions scaled by a factor of 10 in each case. The parameters for each system have been chosen to optimize energy storage, efficiency, overall percentage of CNTs by mass and discharge time while meeting the constraints outlined in section 5.3.2. The dimensions of the three systems are listed in Table 5.1. The operation of the submillimeter-scale device is presented in detail as an example to illustrate the device's operation and demonstrate how energy is released from such a system.

In all three cases, the spring element is taken to be an assembly of 1.36 nm diameter SWCNTs with ideal packing, so that k=91% and A/A_{encl}=0.64. The length of each SWCNT is expected to span the entire length of the spring. A maximum initial strain of 6% is applied to the spring in each case.

The material chosen for the cantilever beams and the escape wheel is silicon carbide because of its high stiffness. The material chosen for the pallet is silicon because stresses in the pallet are not limiting and silicon has a lower density than silicon carbide. The material properties of silicon and silicon carbide are listed in Table 5.2. The piezoelectric material is assumed to be PZT, and the piezoelectric properties used in the model are d_{31}=171$\times 10^{-12}$ m/V, ε_{33}^{T}=1.505$\times 10^{-12}$ F/m, and s_{11}^{E}=16.4$\times 10^{-12}$ m^2/N. The piezoelectric coupling coefficient k_{31} is calculated to be 0.344.

Appropriate values of the mechanical damping coefficient b_m are selected by considering mechanical damping coefficients that yield quality factor Q values of 24 and 200, values that

have previously been reported in the literature for cantilevers used as piezoelectric generators [118, 125]. The corresponding values of b_m are listed in Table 5.3. The electrical damping coefficient b_e is varied by considering a range of values for the load resistance R_L.

The pitch and diameter of the screws are scaled so that η_{screw}=0.47 in all three cases, using a coefficient of friction of μ=0.05. Depending on the scale of the system, the screws are not realistic structures for actual implementation, but they provide a reasonable analytical stand-in for a more practical linear-to-rotational coupling mechanism.

Table 5.1: System dimensions

	Micron-scale	**Submillimeter-scale**	**Millimeter-scale**
CNT grouping diameter	3 μm	30 μm	300 μm
CNT grouping length	80 μm	800 μm	8 mm
Screw pitch	3 μm	30 μm	300 μm
Screw diameter	10 μm	100 μm	1 mm
Escape wheel and pallet thickness	30 μm	300 μm	3 mm
Escape wheel radius, pallet arm length	50 μm	500 μm	5 mm
Cantilever length	400 μm	4 mm	4 cm
Cantilever width	80 μm	800 μm	8 mm
Cantilever height	20 μm	200 μm	2 mm
PZT thickness	0.5 μm	5 μm	50 μm

Table 5.2: Material properties of silicon and silicon carbide [94-96]

	Young's modulus	**Yield stress**	**Density**
Single crystal silicon	160 GPa	120 MPa	2300 kg/m^3
Single crystal SiC	450 GPa	450 MPa	3400 kg/m^3

Table 5.3: Mechanical damping coefficients b_m corresponding to Q=24 and Q=200.

	Micron-scale	**Submillimeter-scale**	**Millimeter-scale**
Q=24	0.00004 kg/s	0.004 kg/s	0.4 kg/s
Q=200	0.0000045 kg/s	0.00045 kg/s	0.045 kg/s

5.4.1. Submillimeter-scale case

To demonstrate how the unit cell works, the operation of the submillimeter-scale device is presented in detail. The spring is a 800 μm long, 30 μm diameter grouping made of 1.36 nm diameter SWCNTs. Filled shells constitute 58% of the volume of the spring. An initial strain of 0.06 is applied to the spring and the stored energy is 5.93×10^{-4} J. For the spring to return to its unstretched length, the escape wheel must rotate 0.8 times. The angular displacement and angular velocity of the escape wheel are plotted against time in Figure 5.21. The graphs show that the rotation of the escape wheel is marked by a series of rapid 6 degree rotations during an impulse followed by a longer period with no displacement during a locking phase. The discharge of the spring is complete once the escape wheel completes 0.8 of a rotation, or 5.02 radians, as shown in Figure 5.21 (a). Energy is gradually released from the spring during each incremental escape wheel rotation.

The graph in Figure 5.22 shows the oscillations of the pallet over time, using damping parameters of b_m=0.004 kg/s and b_e= 0.01 kg/s in this case. The oscillation frequency is 19.4 kHz. As required, the pallet angle does not exceed 9 degrees. The pallet begins with no oscillation since the cantilevers start from rest, and the pallet oscillation amplitude grows rapidly as energy is transferred to the cantilever beams. As operation continues, the amount of energy transferred to the cantilevers with each impulse drops as the strain in the spring decreases, and so the amplitude of the pallet oscillations drops as energy is lost to damping. The red curve is added to the plot to show the escapement phase in relation to the pallet angle. When the pallet angle is between -3 and 3 degrees, an impulse is taking place, and the red line has a value of 1 or -1. The escapement is in the locking phase when the pallet angle is between 3 and 9 degrees or -3 and -9 degrees, and this is denoted by a value of 0 in the red line. After 1.2 ms, the spring has discharged completely, the escape wheel stops rotating, and no further impulses occur. The cantilevers continue to oscillate until all of their energy is dissipated to either mechanical or electrical damping.

Average power output is defined as the average electrical power output during the discharge time, with the discharge time taken to be the time for the electrical system to reach 95% of the total converted energy. The plot of output power vs. time is shown in Figure 5.23,

showing that power output is uneven over time because of the nature of the energy transfer from the spring. The plot in Figure 5.24 shows the converted energy by the piezoelectric generator as a function of time. For this device with b_m=0.004 kg/s and b_e= 0.01 kg/s, the discharge time is 1.02 ms and the average power output is 0.088 W.

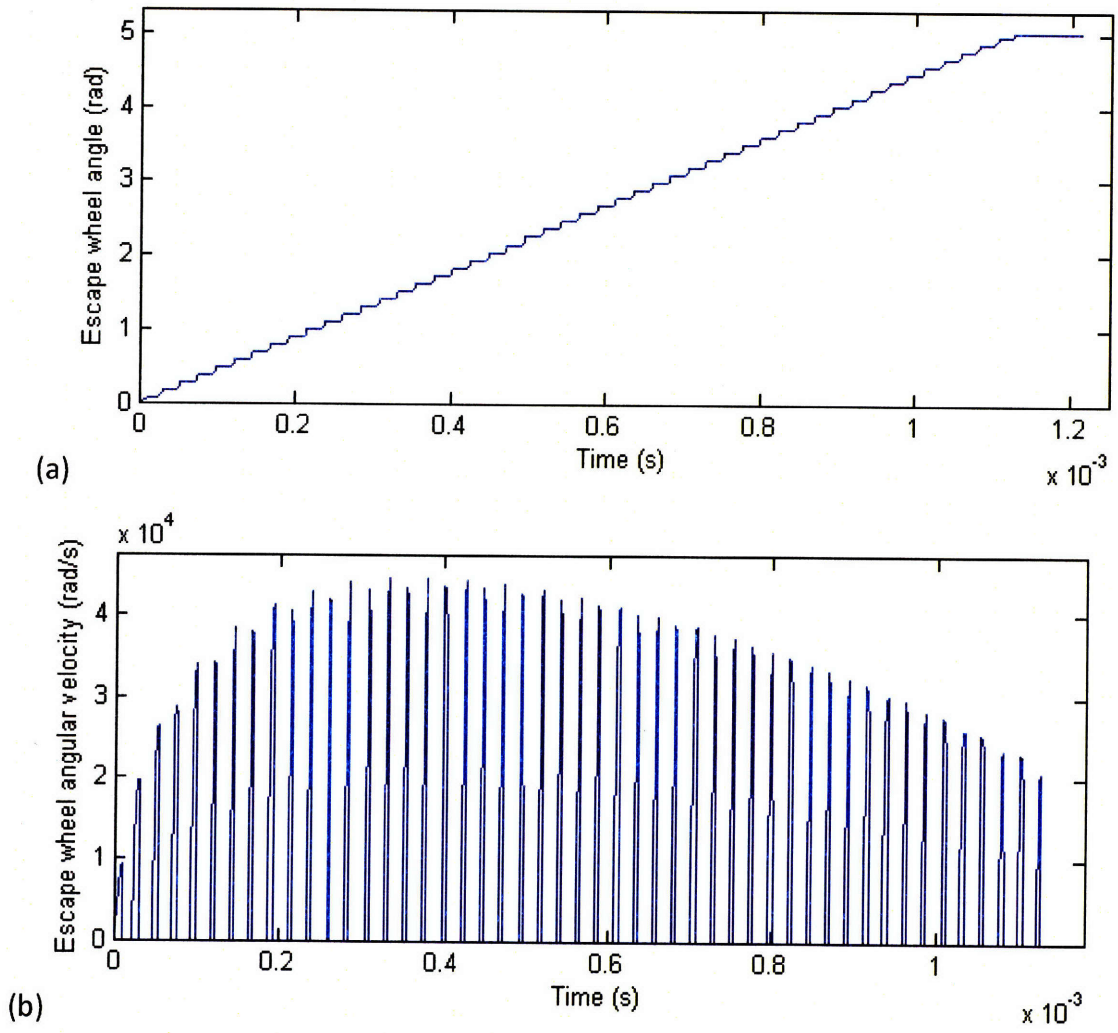

Figure 5.21: (a) Angular displacement and (b) angular velocity of the escape wheel over time.

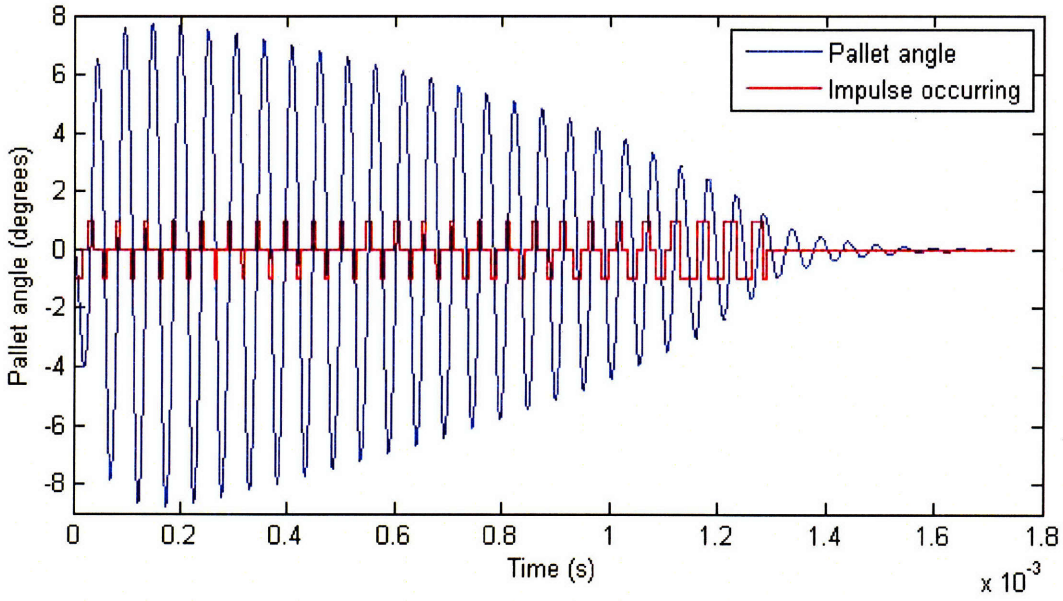

Figure 5.22: Plot of the pallet angle over time. The occurrence of an impulse is shown in red with a value of 1 or -1, while a locking phase is denoted by a value of 0.

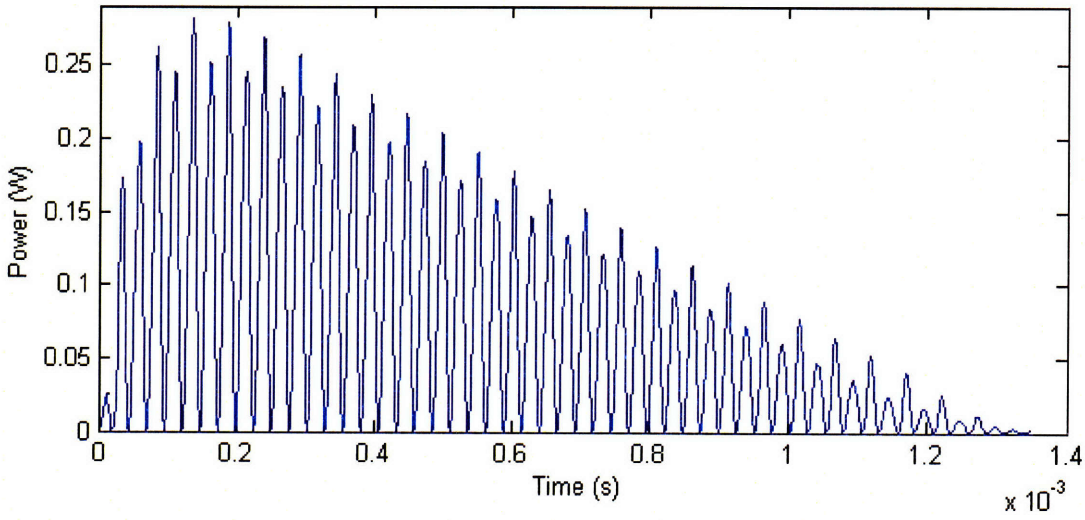

Figure 5.23: Power output from the piezoelectric cantilevers over time for the submillimeter case with b_m=0.004 kg/s and b_e= 0.01 kg/s.

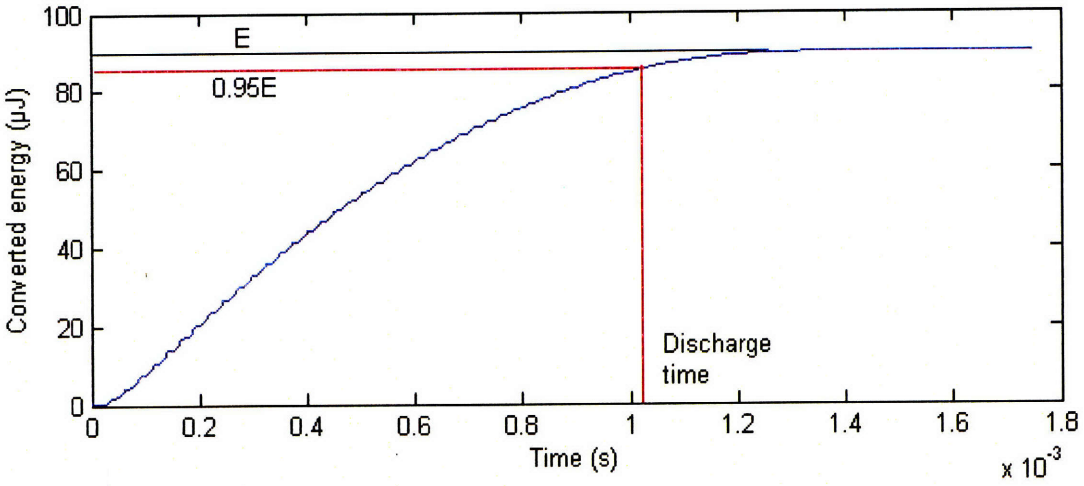

Figure 5.24: Electrical energy converted by the piezoelectric cantilevers as a function of time for the submillimeter case, with b_m=0.004 kg/s and b_e= 0.01 kg/s. The time for the electrical system to reach 95% of its total converted energy is 1.02 ms, as shown on the graph.

The output energy and power from the piezoelectric cantilever beams depend on both the mechanical and the electrical damping in the system. In this case, b_e= 0.01 kg/s corresponds to a load resistance R_L of 440 kΩ, and the total output energy is 8.98×10^{-5} J, from Figure 5.24, for an overall efficiency of 15%. Efficiency and average power output are plotted as a function of load resistance for two different values of the mechanical damping coefficient in Figure 5.25. The efficiency approaches 18% with a Q of 24 and 22% with a Q of 200. Average power output reaches 0.11 W and 0.13 W with a Q of 24 and 200 respectively. As expected, greater efficiencies and higher average power output can be reached with greater values of Q.

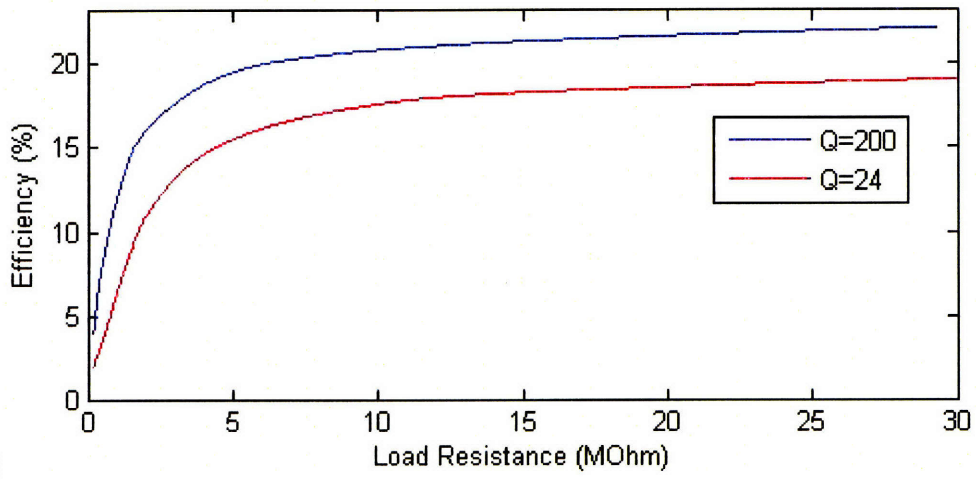

(a)

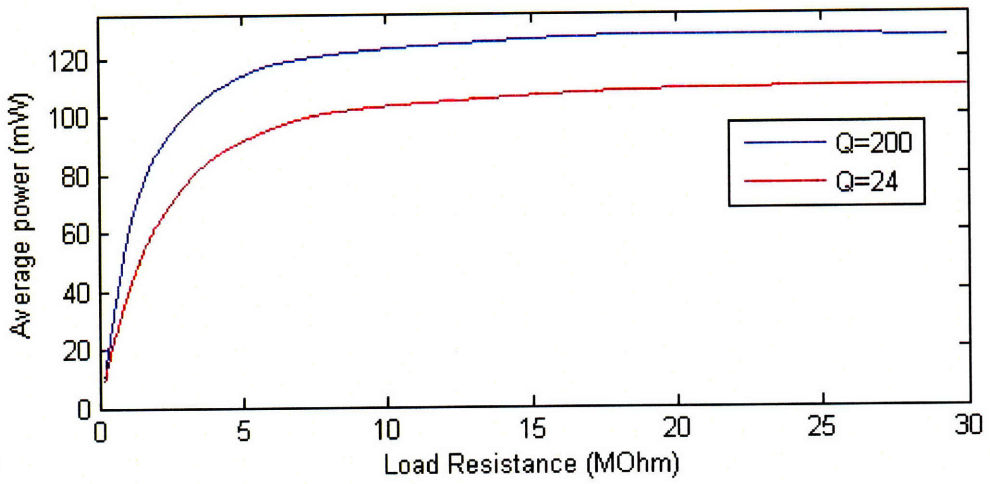

(b)

Figure 5.25: (a) Efficiency vs. load resistance and (b) average power output vs. load resistance for the submillimeter-scale case.

The support structure is considered to made of silicon carbide, with its properties listed in Table 5.2. Using equation (5.4), the mass of the support structure for the spring is 1.5×10^{-7} kg. In contrast, the mass of the spring is 7.25×10^{-10} kg. The mass of the support structure is considerably larger than the mass of the spring because the silicon and silicon carbide used in the design have not been specified as single crystal materials, so the strengths of these materials listed in Table 5.2 are lower than the strengths previously reported in Table 3.1. Once the mass of the escape wheel, pallet, cantilevers, screws and support structure are taken into account, the percentage of CNTs in the device by mass is 0.015%. The cantilevers are the largest structures, and contribute most to the total mass of the system.

The maximum stress on the escape wheel gear teeth is 363 MPa and the maximum stress in the cantilever beams is 338 MPa. These two stresses are high because they are the limiting constraints on the size of the escape wheel. The size of the escape wheel can only be reduced as long as these two stresses do not exceed the yield strength limit of 450 GPa for silicon carbide.

Finally, the reversibility of the device is considered. At the maximum strain in the spring, the moment acting on the escape wheel is M_{max}=1.12 × 10^{-4} Nm. To fully wind the spring, the displaced cantilever must be able to generate a force of $F_{c,max}$ = 0.317 N, based on equation (5.38). A pallet oscillation amplitude of 8 degrees corresponds to a maximum pallet tip

displacement of δ=44 μm. Using equation (5.39), the voltage applied to the piezoelectric material required to generate both a force of $F_{c,max}$ and a displacement of δ is V_{max}=1.6 kV.

5.4.2. Results for three size scales

The operating parameters for all three cases are shown in Table 5.4.

Table 5.4: Operating parameters for devices at three scales, with Q=200

	Micron-scale	**Submillimeter-scale**	**Millimeter-scale**
Applied strain	0.06	0.06	0.06
Energy storage	6×10^{-7} J	6×10^{-4} J	0.6 J
Operating frequency	192 700 Hz	19 400 Hz	1906 Hz
Max overall efficiency	22 %	22 %	22 %
Average power output	0.0013 W	0.13 W	13 W
Discharge time	0.1 ms	1 ms	10 ms
Mass of the spring	7.25×10^{-13} kg	7.25×10^{-10} kg	7.25×10^{-7} kg
Mass of the support structure	1.5×10^{-10} kg	1.5×10^{-7} kg	1.5×10^{-4} kg
Mass of the escape wheel	2.3×10^{-10} kg	2.3×10^{-7} kg	2.3×10^{-4} kg
Mass of the pallet	3.5×10^{-11} kg	3.5×10^{-8} kg	3.5×10^{-5} kg
Mass of the cantilevers	4.4×10^{-9} kg	4.4×10^{-6} kg	4.4×10^{-3} kg
Mass of the screws	2.6×10^{-12} kg	2.6×10^{-9} kg	2.6×10^{-6} kg
Percentage of CNTs by mass	0.015 %	0.015 %	0.015 %
Maximum cantilever tip displacement δ	4.4 μm	44 μm	440 μm
Maximum moment on escape wheel M_{max}	1.12×10^{-7} Nm	1.12×10^{-4} Nm	0.112 Nm
Maximum stress in gear teeth	363 MPa	363 MPa	363 MPa
Maximum stress in cantilever beams	338 MPa	338 MPa	338 MPa
Voltage required to recharge	157 V	1 570 V	15 700 V

Since energy stored in the spring is proportional to volume, energy storage scales with the cube of the linear dimension. Operating frequency scales inversely with the linear dimension of the system. Both the scaling of energy storage and operating frequency favour the use of larger

scale systems. Lower operating frequencies are generally preferred for this type of system because they provide the escapement mechanism with more control and produce longer spring discharge times.

The results in Table 5.4 show that maximum stresses in the gear teeth and the cantilever beams are scale independent, as expected based on equations (5.40) and (5.41) since all dimensions have been scaled by a factor of 10. The overall percentage of CNTs by mass is 0.015% at all three scales. This low result was obtained because the components coupled to the spring are far larger than the spring itself. While this result is lower than desired, it is the highest value that could be obtained within the limits of the constraints of the problem, which indicates the difficulty of obtaining a significant composition of CNTs in the overall device. The principal limiting factors were the stresses in the cantilever beams and escape wheel teeth, which dictated that the cantilever and the escape wheel had to be much larger than the size of the spring for the forces acting on them to be manageable.

Figure 5.26 (a) and Figure 5.27 (a) show plots of efficiency vs. load resistance for the micron-scale and the millimeter-scale cases. In both cases, overall efficiency approaches 18% with a Q of 24 and 22% with a Q of 200, just as in the submillimeter-scale case. The same magnitude of load resistance is required to achieve the highest efficiency in all three cases. These results indicate that efficiency is unaffected by the scale of the system within the limits of this model. The results here should not be taken as the maximum achievable efficiency but rather as the efficiency that can be realistically expected based on a preliminary examination of this type of system.

Average power output vs. load resistance is plotted for the micron-scale and the millimeter-scale cases in Figure 5.26 (b) and Figure 5.27 (b). Power reaches 13 W in the millimeter-scale case, 0.13 W in the submillimeter-scale case, and 0.0013 W in the micro-scale case. Energy scales cubically with the linear dimension and the discharge time scales linearly with the dimensions, so as expected power output scales with the square of the linear dimension. High load resistances are required to reach the highest power output levels.

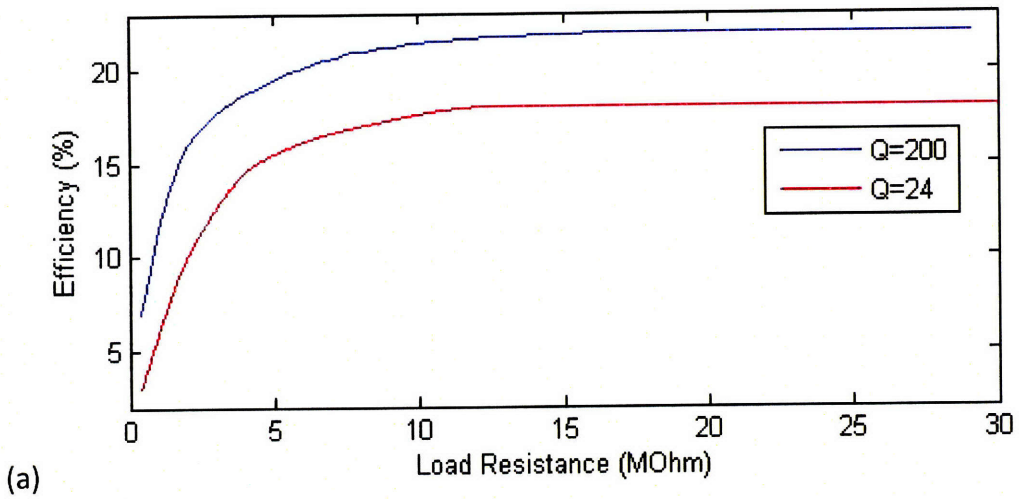

(a)

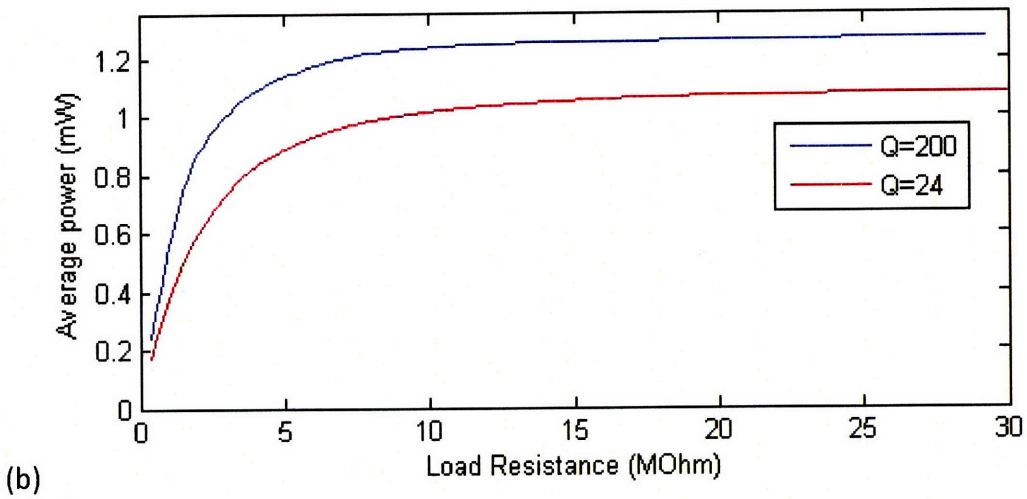

(b)

Figure 5.26: (a) Efficiency vs. load resistance and (b) average power vs. load resistance for the micron-scale case.

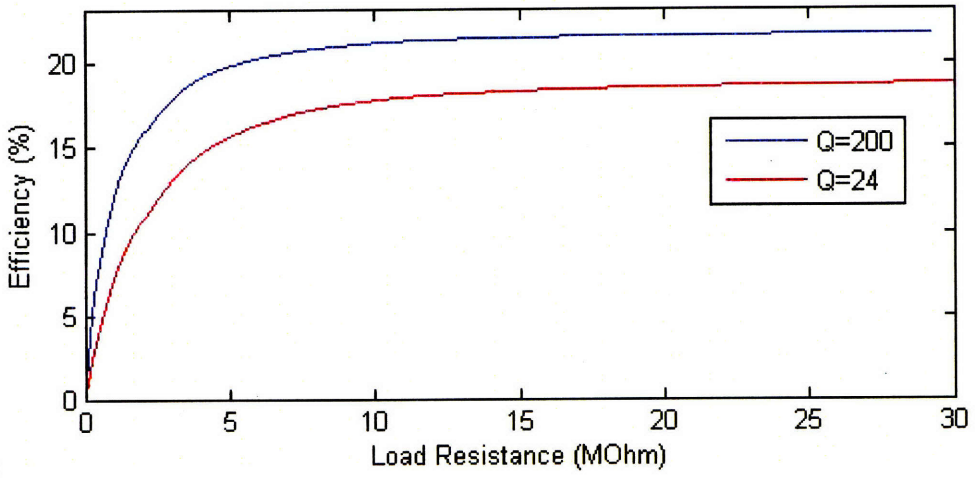

(a)

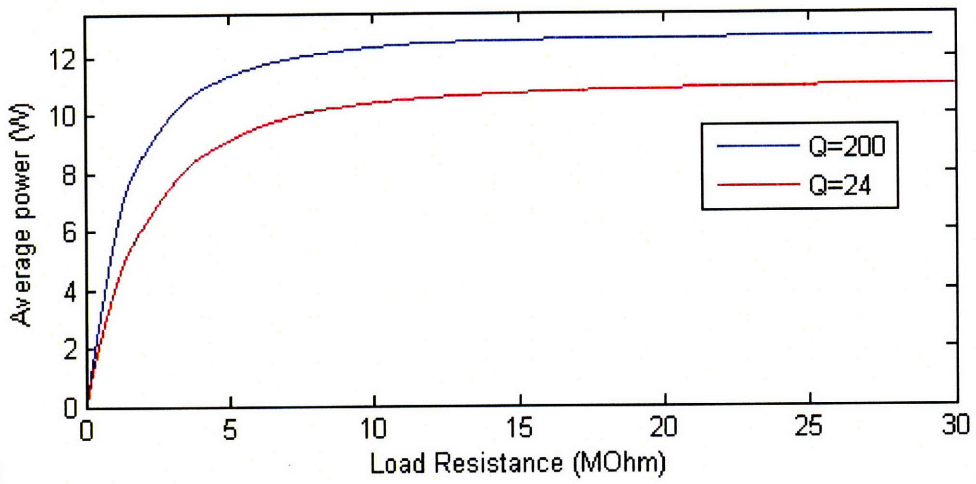

(b)

Figure 5.27: (a) Efficiency vs. load resistance and (b) average power vs. load resistance for the millimeter-scale case.

In terms of reversibility, the voltage required to drive the cantilever beams to recharge the systems scales linearly with the overall scale of the system, with 157 V, 1570 V and 15700 V required for the micron-scale, submillimeter-scale and millimeter-scale case devices respectively. These voltages are high and largely infeasible, although they can be lowered by using thicker layers of piezoelectric material. The high voltages needed to recharge the system favour a micron-scale or smaller system for this particular configuration of piezoelectric material. To avoid needing to apply such large voltages, the devices could be intended for single use only or recharged to strains in the springs lower than the 6% applied here. While the piezoelectric unimorph is useful as a generator, it may not be the most practical actuator for recharging the system since unimorphs can generate large displacements, but only small forces. As a result, alternative actuators or motors should be considered for recharging the system, though they would add considerable more complexity.

5.4.3. Submillimeter-scale case with a long spring

The lengths of the CNT springs used in the previous simulations were 80 µm, 800 µm, and 8mm for the devices at three different scales. These lengths were chosen to reflect the current state of technology available for growing CNTs, which are typically grown to lengths no longer

than several millimeters. No long, macroscale assemblies have been built to date that demonstrate a stiffness of 1 TPa and strains as high as 6%. However, it is assumed that the technology for fabricating individual CNTs and high quality assemblies of CNTs will continue to progress so that high quality, much longer springs will be available in the near future. One can neglect the current constraints of CNT technology to examine the results that can be obtained using more optimistic dimensions for the CNT springs.

The simulation for the submillimeter-scale case is rerun using the same parameters listed in Table 5.1, but changing the length of the spring from 800 μm to 50 cm. In this case, the energy stored in the spring is 0.37 J. For the spring to return to its unstretched length following an initial strain of 6%, the escape wheel rotates 500 times. The discharge time of the spring is 3s, for an average power output of 0.12 W. Comparing these results to the results of the submillimeter-scale device with a spring length of 800 μm indicates that power remains unchanged but discharge time increases significantly. Efficiency remains unchanged at 22%. The higher energy storage and longer discharge time indicate that the use of longer springs is advantageous.

The mass of all of the components in the design are listed in Table 5.5. The mass of the spring, the support structure and the screws are different than in Table 5.4. The mass of the screws have increased to accommodate 500 rotations instead of 0.8 rotations. The mass of the support structure increases since it must support a longer spring. The mass of the remaining components are unchanged. The percentage by mass of CNTs in the device is 0.46%, an improvement over the previous result of 0.015%, but still a low value. With the longer spring, the mass of the overall system is dominated by the mass of the support structure, rather than the mass of the cantilever beams, as was previously observed. The support structure is now the limiting component to achieving a high percentage of CNTs by mass in the system, illustrating the importance of using very high quality material to build the support structure. If the strength of silicon carbide of 450 MPa used in the calculation for the mass of the support structure is replaced by the strength of single crystal silicon carbide, with properties listed in Table 3.1 and a strength of 21 GPa, then the mass of the support structure becomes 2×10^{-6} kg, and the overall percentage of mass of CNTs in the system becomes 5%, a far more encouraging result.

Table 5.5: Mass of the components in the submillimeter-scale device with a 0.5 m long spring

Mass of the spring	9.1×10^{-7} kg
Mass of the support structure	1.9×10^{-4} kg
Mass of the escape wheel	2.3×10^{-7} kg
Mass of the pallet	3.5×10^{-8} kg
Mass of the cantilevers	4.4×10^{-6} kg
Mass of the screws	3.3×10^{-6} kg

5.5. Discussion of results

The current work to model a portable power source provides only an early-stage mathematical proof of concept design; it is not yet optimized for performance or manufacturability. At all three size scales presented here, the CNT-based energy storage element occupies only a small fraction of the mass and volume of the total system because of the power-regulating and energy conversion hardware. The model indicates that such a system can be used to first store and subsequently release and convert the stored energy to the electrical domain, but does not show that a complete system can be engineered that maintains high overall energy density. However, the model is a useful tool to study the implementation issues associated with building a power source based on CNT springs.

The results of this work indicate that energy storage, operating frequency, efficiency, discharge time and power all scale well with size, leaving flexibility in the choice of the overall size scale. Higher power output and energy storage levels are achieved at larger scales. The voltages required to recharge the system using piezoelectric actuation are prohibitively large at larger scales, indicating that an alternative type of motor should be implemented for recharging a system with dimensions of millimeters or above.

The inclusion of the generator and the escapement added considerable complexity and mass to the system. While both perform useful functions, the resulting fraction of CNTs in the system ranging from 0.015 - 0.5% is too low for implementation in an actual device. Further

work is needed to design an optimized system that provides power regulation and energy conversion without significantly affecting the energy density of the overall device.

The design of this conceptual power source has highlighted that an important challenge of working with CNT springs is managing their forces. For their size, the forces from the springs are large and tend to overwhelm other structures coupled to the spring. Since there are no materials with properties to match those of CNTs, the only way to build structures that are able to interact with a CNT spring and handle its forces is to make these structures much larger than the spring. In this design, the forces on the escape wheel teeth were a limiting factor, so the diameter of the escape wheel had to be much larger than the diameter of the spring. Increasing the size of the coupled extraction hardware significantly reduces the energy density of the overall system, losing the energy storage advantage of CNTs. The system's design has demonstrated the challenge of designing a complex power source that maintains the high energy density of the spring.

Alternative design paths can be pursued to obtain higher energy densities. One option is to build all coupling structures from the highest quality materials such as single crystal silicon carbide or single crystal diamond to limit the energy density losses. A shortcoming of this particular design was that it tried to match the scale of the spring to the scale of the rest of the hardware, which proved to be difficult. Rather than match the scale of a single spring to the scale of the generator, it is possible to couple a large number of smaller springs, with smaller applied loads, to a single generator. The springs can be triggered to release sequentially so that the forces on the coupling mechanism and generator are manageable. In this way, the fraction of the system composed of CNTs can be high without overwhelming the rest of the coupling structures. Alternatively, eliminating the power-regulating hardware would be suitable for power systems that can utilize uneven power levels. Eliminating the conversion hardware would be appropriate for applications that require input power in the mechanical domain. Both options would simplify the design of the power source and increase the volume fraction of the CNT-based energy storage element.

The design of only a single unit cell has been presented here. Further work should address the design of a larger power source made from an assembly of a large number of unit cells that

are triggered to release in parallel or sequentially to customize the level of power output and overall discharge time.

6. Conclusions and Future Work

The concept for a highly promising new method of energy storage using carbon nanotubes has been presented. An examination of the capabilities of CNT super-springs for elastic energy storage has been motivated by extensive experimental and theoretical studies of the mechanical properties of CNTs that have revealed nanoscale structures with a remarkable combination of high stiffness, strength and flexibility. The ability of CNTs to sustain tensile strains of 6% and potentially as high as 20% in a reversible manner indicates that mechanical springs based on these structures are likely to surpass the current storage capabilities of existing steel springs. Considering the spring element alone, calculations predict the energy density of CNT springs at the highest applied strains to be three orders of magnitude greater than that of steel springs and almost ten times greater than the energy density of electrochemical batteries. Once practical considerations are taken into account, such as the need for a support structure or additional extraction hardware, the energy density of a power source containing a CNT spring will be lower than the calculations predict for the spring element alone. However, even when a support structure is taken into consideration in energy density calculations, a CNT spring can still store energy with a density more than two orders of magnitude higher than a steel spring and on the same level as batteries. CNT springs incorporated into a power source may offer a viable alternative to batteries because of their predicted high power density, ability to store energy without self-discharge, potentially infinite lifetime, and ability to operate in extreme temperatures.

Models of CNTs as continuum structures under different deformation modes were used to estimate the energy density that can be reached in CNT springs. Loading was applied in tension, compression, bending and torsion. The assumption was made that a spring should not be loaded past its buckling limit to ensure reversible energy storage. As a result, tension offers the most promise for high density energy storage because tensile strains are limited only by the elastic limit of the material rather than the buckling limit. Calculations of energy density in CNTs under combined loadings have shown that there is little to gain in terms of energy density by combining two or more deformation modes. However, it is likely that the best choice of loading

for a spring will be a combination of two or more deformation modes so that a spring can be built that is compact and can integrate well with the rest of the architecture of a power source.

Energy density estimates indicate that SWCNTs are best suited for energy storage. Poor load transfer between shells of a MWCNT limits the effectiveness of these structures for energy storage. The radial deformation of SWCNT cross-sections due to van der Waals interactions from other nanotubes or a substrate suggests that SWCNTs with small diameters, ideally 1 nm or smaller, would be best for springs. Since SWCNTs naturally occur in bundles, the springs should be composed of dense groupings of bundles of SWCNTs with spacing between tubes that approaches the ideal spacing of 0.34 nm.

The conceptual design of a portable power source was presented to study how energy can be stored in the elastic deformation of CNTs and subsequently released as an electrical output. The power generating unit cell design is composed of a CNT-based spring, an escapement mechanism to regulate the energy release from the spring, and a piezoelectric generator to convert the released mechanical energy into the electrical domain. A model of the power source was generated as a tool to study the operation of the system at different size scales and assess the potential utility and challenges associated with building such a device. Modeling results of systems at different scales indicated that energy storage, power output and overall efficiency scale well with size, leaving some flexibility in the choice of the size scale for the system. A support structure, generator and escapement mechanism all contributed useful functionality to the power source, but their added mass and volume resulted in a system that was composed of only a small fraction of CNTs by mass because of limitations inherent to the design. The current model is an early-stage design that indicates only that energy can be stored and released from a spring in a controlled manner using a coupling mechanism and generator. It does not yet demonstrate the extent to which systems can be engineered to maintain high overall energy density. Optimizing the fraction by mass and volume of CNTs in the power source should be the main focus of subsequent designs.

The presented models indicate that CNT super-springs show significant potential, but additional experimental research is still needed before a spring can be fabricated and incorporated into a power source. Future work should focus on building and testing CNT

springs. Assumptions are made throughout this work that large groupings of CNTs can achieve ideal stiffness and strength. In reality, many macroscale assemblies, such as yarns and mats, demonstrate mechanical properties inferior to those of individual CNTs and would be inadequate as a medium for energy storage. High quality macroscale SWCNT assemblies are still needed that display a high degree of alignment, near-ideal packing density, strong interactions between adjacent tubes and good load transfer. Forests of CNTs grown using CVD are promising starting materials for super-springs because of their long lengths, close-packing, organized structure and parallel alignment. Further progress is needed in CVD synthesis and purification techniques to grow high quality, millimeter-length forests of SWCNTs with ideal stiffness and strength. Densification techniques using capillary forces and mechanical pressure have already demonstrated that it is possible to increase the density of as-grown forests, and these densified structures are expected to display excellent mechanical properties. Subsequent work should be done to further develop the densification techniques to build aligned groupings of SWCNTs with graphitic spacing that can have a range of diameters and lengths. Fabrication of springs should focus on groupings in which SWCNTs span the entire length of an assembly, for shorter springs, as well as on longer groupings of discontinuous SWCNTs with high contact surface area between the tubes to ensure excellent load transfer. The development and testing of strong attachment methods, using either epoxy or strong covalent bonding to silicon, is essential to ensure that applied loads are distributed evenly throughout an assembly and that springs can be loaded up to near their elastic limit. Finally, work in mechanical characterization and modeling is needed to determine the effect of packing density, inter-tube spacing, tube diameter, defect density, twisting, contact lengths and load transfer on the measured stiffness and strength of bundles. The results of this work will provide valuable information about the behaviour and properties of macroscale assemblies and help to identify the best structure and configuration to maximize energy storage in CNT springs.

References

[1] D. A. Walters, L. M. Ericson, M. J. Casavant, J. Liu, D. T. Colbert, K. A. Smith, R. E. Smalley, "Elastic strain of freely suspended single-wall carbon nanotube ropes," *Applied Physics Letters,* vol. 74, pp. 3803-3805, 1999.

[2] M. Yu, B. S. Files, S. Arepalli, R. S. Ruoff, "Tensile loading of ropes of single wall carbon nanotubes and their mechanical properties," *Physical Review Letters,* vol. 84, pp. 5552-5555, 2000.

[3] K. M. Liew, X. Q. He, C. H. Wong, "On the study of elastic and plastic properties of multi-walled carbon nanotubes under axial tension using molecular dynamics simulation," *Acta Materialia,* vol. 52, pp. 2521-2527, 2004.

[4] M. Meo, M. Rossi, "A molecular-mechanics based finite element model for strength prediction of single wall carbon nanotubes," *Materials Science and Engineering A,* vol. 454-455, pp. 170-177, 2007.

[5] B. I. Yakobson, M. P. Campbell, C. J. Brabec, J. Bernholc, "High strain rate fracture and C-chain unraveling in carbon nanotubes," *Computational Materials Science,* vol. 8, pp. 341-348, 1997.

[6] S. Iijima, "Helical microtubules of graphitic carbon," *Nature,* vol. 354, pp. 56-58, 1991.

[7] R. S. Ruoff, D. C. Lorents, "Mechanical and thermal properties of carbon nanotubes," *Carbon,* vol. 33, pp. 925-930, 1995.

[8] D. Qian, G. J. Wagner, W. K. Liu, M. Yu, R. S. Ruoff, "Mechanics of carbon nanotubes," *Applied Mechanics Reviews,* vol. 55, pp. 495-533, 2002.

[9] A. Loiseau, P. Launois, P. Petit, S. Roche, J. P. Salvetat, *Understanding carbon nanotubes*. New York: Springer, 2006.

[10] M. Meyyappan, *Carbon Nanotubes: Science and Applications*. New York: CRC Press, 2005.

[11] K. M. Liew, C. H. Wong, X. Q. He, M. J. Tan, S. A. Meguid, "Nanomechanics of single and multiwalled carbon nanotubes," *Physical Review B,* vol. 69, 2004.

[12] M. S. Dresselhaus, G. Dresselhaus, R. Saito, "Physics of carbon nanotubes," *Carbon,* vol. 33, pp. 883-891, 1995.

[13] A. Pantano, D. M. Parks, M. C. Boyce, "Mechanics of deformation of single- and multi-wall carbon nanotubes," *Journal of the Mechanics and Physics of Solids,* vol. 52, pp. 789-821, 2004.

[14] N. Grobert, "Carbon nanotubes - becoming clean," *Materials Today,* vol. 10, pp. 28-35, 2007.

[15] M. Terrones, "Science and technology of the twenty-first century: synthesis, properties, and applications of carbon nanotubes," *Annual Review of Materials Research,* vol. 33, pp. 419-501, 2003.

[16] B. N. Wang, R. D. Bennett, E. Verploegen, A. J. Hart, R. E. Cohen, "Quantitative characterization of the morphology of multiwall carbon nanotube films by small-angle x-ray scattering," *Journal of Physical Chemistry,* vol. 111, pp. 5859-5865, 2007.

[17] R. Saito, G. Dresselhaus, M.S. Dresselhaus, *Physical Properties of Carbon Nanotubes*. London: Imperial College Press, 1998.

[18] M. M. Treacy, T. W. Ebbesen, J. M. Gibson, "Exceptionally high Young's modulus observed for individual carbon nanotubes," *Nature,* vol. 381, pp. 678-680, 1996.

[19] O. Lourie, H. D. Wagner, "Evaluation of Young's modulus of carbon nanotubes by micro-Raman spectroscopy," *Journal of Materials Research,* vol. 13, pp. 2418-2422, 1998.

[20] M. Yu, O. Lourie, M. J. Dyer, K. Moloni, T. F. Kelly, R. S. Ruoff, "Strength and breaking mechanism of multiwalled carbon nanotubes under tensile load," *Science,* vol. 287, pp. 637-640, 2000.

[21] J. Salvetat, G. A. Briggs, J. Bonard, R. R. Bacsa, A. J. Kulik, T. Stöckli, N. A. Burnham, L. Forró, "Elastic and shear moduli of single-walled carbon nanotube ropes," *Physical Review Letters,* vol. 82, pp. 944-947, 1999.

[22] B. I. Yakobson, C. J. Brabec, J. Bernholc, "Nanomechanics of carbon tubes: instabilities beyond linear response," *Physical Review Letters,* vol. 76, pp. 2511-2514, 1996.

[23] Q. Wang, S. T. Quek, V. K. Varadan, "Torsional buckling of carbon nanotubes," *Physics Letters A,* vol. 367, pp. 135-139, 2007.

[24] M. S. Dresselhaus, G. Dresselhaus, P. Avouris, *Carbon nanotubes: synthesis, structure, properties, and applications*. New York: Springer, 2001.

[25] J. P. Lu, "Elastic properties of carbon nanotubes and nanoropes," *Physical Review Letters,* vol. 79, pp. 1297-1300, 1997.

[26] E. W. Wong, P. E. Sheehan, C. M. Lieber, "Nanobeam mechanics: elasticity, strength, and toughness of nanorods and nanotubes," *Science,* vol. 277, pp. 1971-1975, 1997.

[27] W. Yu, X. X. Wang, X. Ni, "Atomistic simulation of the torsion deformation of carbon nanotubes," *Modelling and Simulation in Materials Science and Engineering,* vol. 12, pp. 1099-1107, 2004.

[28] V. N. Popov, V. E. Van Doren, M. Balkanski, "Elastic properties of single-walled carbon nanotubes," *Physical Review B,* vol. 61, pp. 3078-3084, 2000.

[29] A. R. Hall, L. An, J. Liu, L. Vicci, M. R. Falvo, R. Superfine, S. Washburn, "Experimental measurement of single-wall carbon nanotube torsional properties," *Physical Review Letters,* vol. 96, 2006.

[30] J. P. Lu, J. Han, "Carbon nanotubes and nanotube-based nano devices," *International Journal of High Speed Electronics and Systems,* vol. 9, pp. 101-123, 1998.

[31] MatWeb Material Property Data, http://www.matweb.com/.

[32] M. R. Falvo, G. J. Clary, R. M. Taylor, V. Chi, F. P. Brooks, S. Washburn, R. Superfine, "Bending and buckling of carbon nanotubes under large strain," *Nature,* vol. 389, pp. 582-584, 1997.

[33] M. Arroyo, T. Belytschko, "Continuum mechanics modeling and simulation of carbon nanotubes," *Meccanica,* vol. 40, pp. 455-469, 2005.

[34] K. Mylvaganam, L. C. Zhang, "Deformation-promoted reactivity of single-walled carbon nanotubes," *Nanotechnology,* vol. 17, pp. 410-414, 2006.

[35] Z. W. Pan, S. S. Xie, L. Lu, B. H. Chang, L. F. Sun, W. Y. Zhou, G. Wang, D. L. Zhang, "Tensile tests of ropes of very long aligned multiwall carbon nanotubes," *Applied Physics Letters,* vol. 74, pp. 3152-3154, 1999.

[36] W. B. Choi, D. S. Chung, J. H. Kang, H. Y. Kim, Y. W. Jin, I. T. Han, Y. H. Lee, J. E. Jung, N. S. Lee, G. S. Park, J. M. Kim, "Fully sealed, high-brightness carbon-nanotube field-emission display," *Applied Physics Letters,* vol. 75, pp. 3129-3131, 1999.

[37] M. H. Chen, Z. C. Huang, G. T. Wu, G. M. Zhu, J. K. You, Z. G. Lin, "Synthesis and characterization of SnO–carbon nanotube composite as anode material for lithium-ion batteries," *Materials Research Bulletin,* vol. 38, pp. 831-836, 2003.

[38] A. Bachtold, P. Hadley, T. Nakanishi, C. Dekker, "Logic circuits with carbon nanotube transistors," *Science,* vol. 294, pp. 1317-1320, 2001.

[39] V. Derycke, R. Martel, J. Appenzeller, P. Avouris, "Carbon nanotube inter- and intramolecular logic gates," *Nano Letters,* vol. 1, pp. 453-456, 2001.

[40] T. Rueckes, K. Kim, E. Joselevich, G. Y. Tseng, C. Cheung, C. M. Lieber, "Carbon nanotube-based nonvolatile random access memory for molecular computing," *Science,* vol. 289, pp. 94-97, 2000.

[41] J. Kong, N. R. Franklin, C. Zhou, M. F. Chapline, S. Peng, K. Cho, H. Dai, "Nanotube molecular wires as chemical sensors," *Science,* vol. 287, pp. 622-625, 2000.

[42] H. J. Hwang, K. R. Byun, J. W. Kang, "Carbon nanotubes as nanopipette: modelling and simulations," *Physica E,* vol. 23, pp. 208-216, 2004.

[43] S. Akita, Y. Nakayamaa, W. Mizooka, Y. Takano, T. Okawa, Y. Miyatake, S. Yamanaka, M. Tsuji, T. Nosaka, "Nanotweezers consisting of carbon nanotubes operating in an atomic force microscope," *Applied Physics Letters,* vol. 79, pp. 1691-1693, 2001.

[44] A. Bianco, K. Kostarelos, M. Prato, "Applications of carbon nanotubes in drug delivery," *Current Opinion in Chemical Biology,* vol. 9, pp. 674-679, 2005.

[45] A. C. Dillon, K. M. Jones, T. A. Bekkedahl, C. H. Kiang, D. S. Bethune, M. J. Heben, "Storage of hydrogen in single-walled carbon nanotubes," *Nature,* vol. 386, pp. 377-379, 1997.

[46] J. E. Jang, S. N. Cha, Y. Choi, G. A. Amaratunga, D. J. Kang, D. G. Hasko, J. E. Jung, J. M. Kim, "Nanoscale capacitors based on metal-insulator-carbon nanotube-metal structures," *Applied Physics Letters,* vol. 87, 2005.

[47] J. Schindall, "The Charge of the Ultracapacitors," *IEEE Spectrum,* vol. 44, pp. 42-46, 2007.

[48] J. H. Hafner, C. Cheung, T. H. Oosterkamp, C. M. Lieber, "High-yield assembly of individual single-walled carbon nanotube tips for scanning probe microscopies," *Journal of Physical Chemistry B,* vol. 105, pp. 743-746, 2001.

[49] R. Andrews, M. C. Weisenberger, "Carbon nanotube polymer composites," *Current Opinion in Solid State and Materials Science,* vol. 8, pp. 31-37, 2004.

[50] N. Tai, M. Yeh, J. Liu, "Enhancement of the mechanical properties of carbon nanotube/phenolic composites using a carbon nanotube network as the reinforcement," *Carbon,* vol. 42, pp. 2735-2777, 2004.

[51] E. T. Thostenson, Z. Ren, T. Chou, "Advances in the science and technology of carbon nanotubes and their composites: a review," *Composites Science and Technology,* vol. 61, pp. 1899-1912, 2001.

[52] S. A. Chesnokov, V. A. Nalimova, A. G. Rinzler, R. E. Smalley, J. E. Fischer, "Mechanical energy storage in carbon nanotube springs," *Physical Review Letters,* vol. 82, pp. 343-346, 1999.

[53] A. Cao, P. L. Dickrell, W. G. Sawyer, M. N. Ghasemi-Nejhad, P. M. Ajayan, "Super-compressible foamlike carbon nanotube films," *Science,* vol. 310, pp. 1307-1310, 2005.

[54] J. C. Meyer, M. Paillet, S. Roth, "Single-molecule torsional pendulum," *Science,* vol. 309, pp. 1539-1541, 2005.

[55] S. J. Papadakis, A. R. Hall, P. A. Williams, L. Vicci, M. R. Falvo, R. Superfine, S. Washburn, "Resonant oscillators with carbon-nanotube torsion springs," *Physical Review Letters,* vol. 93, 2004.

[56] D. N. Futaba, K. Hata, T. Yamada, T. Hiraoka, Y. Hayamizu, Y. Kakudate, O. Tanaike, H. Hatori, M. Yumura, S. Iijima, "Shape-engineerable and highly densely packed single-walled carbon nanotubes and their application as super-capacitor electrodes," *Nature Materials,* vol. 5, pp. 987-994, 2006.

[57] D. Qian, W. K. Liu, R. S. Ruoff, "Load transfer mechanism in carbon nanotube ropes," *Composites Science and Technology,* vol. 63, pp. 1561-1569, 2003.

[58] T. V. Sreekumar, T. Liu, S. Kumar, L. M. Ericson, R. H. Hauge, R. E. Smalley, "Single-wall carbon nanotube films," *Chemistry of Materials,* vol. 15, pp. 175-178, 2003.

[59] J. A. Astrom, A. V. Krasheninnikov, K. Nordlund, "Carbon nanotube mats and fibers with irradiation-improved mechanical characteristics: A theoretical model," *Physical Review Letters,* vol. 93, 2004.

[60] L. M. Ericson, H. Fan, H. Peng, V. A. Davis, W. Zhou, J. Sulpizio, Y. Wang, R. Booker, J. Vavro, C. Guthy, A. N. Parra-Vasquez, M. J. Kim, S. Ramesh, R. K. Saini, C. Kittrell, G. Lavin, H. Schmidt, W. W. Adams, W. E. Billups, M. Pasquali, W. Hwang, R. H. Hauge, J. E. Fischer, R. E. Smalley, "Macroscopic, neat, single-walled carbon nanotube fibers," *Science,* vol. 305, pp. 1447-1449, 2004.

[61] Y. Li, I. A. Kinloch, A. H. Windle, "Direct spinning of carbon nanotube fibers from chemical vapor deposition synthesis," *Science,* vol. 304, pp. 276-278, 2004.

[62] A. Thess, R. Lee, P. Nikolaev, H. Dai, P. Petit, J. Robert, C. Xu, Y. H. Lee, S. G. Kim, A. G. Rinzler, D. T. Colbert, G. E. Scuseria, D. Tomanek, J. E. Fischer, R. E. Smalley, "Crystalline ropes of metallic carbon nanotubes," *Science,* vol. 273, pp. 483-487, 1996.

[63] J. C. Lasjaunias, K. Biljakovic, P. Monceau, J. L. Sauvajol, "Low-energy vibrational excitations in carbon nanotubes studied by heat capacity," *Nanotechnology,* vol. 14, pp. 998-1003, 2003.

[64] J. Salvetat, S. Bhattacharyya, R. B. Pipes, "Progress on mechanics of carbon nanotubes and derived materials," *Journal of Nanoscience and Nanotechnology,* vol. 6, pp. 1857-1882, 2006.

[65] B. I. Yakobson, G. Samsonidze, G. G. Samsonidze, "Atomistic theory of mechanical relaxation in fullerene nanotubes," *Carbon,* vol. 38, pp. 1675-1680, 2000.

[66] R. B. Pipes, P. Hubert, "Helical carbon nanotube arrays: mechanical properties," *Composites Science and Technology,* vol. 62, pp. 419-428, 2002.

[67] M. Sammalkorpi, A. V. Krasheninnikov, A. Kuronen, K. Nordlund, K. Kaski, "Irradiation-induced stiffening of carbon nanotube bundles," *Nuclear Instruments and Methods in Physics Research B,* vol. 228, pp. 142-145, 2005.

[68] A. Kis, G. Csanyi, J. P. Salvetat, T. Lee, E. Couteau, A. J. Kulik, W. Benoit, J. Brugger, L. Forro, "Reinforcement of single-walled carbon nanotube bundles by intertube bridging," *Nature Materials,* vol. 3, pp. 153-157, 2004.

[69] A. J. Hart, L. Laake, A. H. Slocum, "Desktop growth of carbon-nanotube monoliths with in situ optical imaging," *Small,* vol. 3, pp. 772-777, 2007.

[70] K. Hata, D. N. Futaba, K. Mizuno, T. Namai, M. Yumura, S. Iijima, "Water-assisted highly efficient synthesis of impurity-free single-walled carbon nanotubes," *Science,* vol. 306, pp. 1362-1364, 2004.

[71] H. Dai, J. H. Hafner, A. G. Rinzler, D. T. Colbert, R. E. Smalley, "Nanotubes as nanoprobes in scanning probe microscopy," *Nature,* vol. 384, pp. 147-150, 1996.

[72] Z. W. Xu, Q. L. Zhao, T. Sun, L. Q. Guo, R. Wang, S. Dong, "Welding method for fabricating carbon nanotube probe," *Journal of Materials Processing Technology,* vol. 190, pp. 397-401, 2007.

[73] M. Yoshimura, S. Jo, K. Ueda, "Fabrication of carbon nanostructure onto the apex of scanning tunneling microscopy probe by chemical vapor deposition," *Japanese Journal of Applied Physics,* vol. 42, pp. 4841–4843, 2003.

[74] J. D. Whittaker, M. Brink, G. A. Husseini, M. R. Linford, R. C. Davis, "Self-aligned mechanical attachment of carbon nanotubes to silicon dioxide structure by selective silicon dioxide chemical-vapour deposition," *Applied Physics Letters,* vol. 83, pp. 5307-5309, 2003.

[75] S. Akita, Nishijima, H., Nakayama, Y., Tokumasu, F., Takeyasu, K., "Carbon nanotube tips for a scanning probe microscope: their fabrication and properties," *Journal of Physics D: Applied Physics,* vol. 32, pp. 1044-1048, 1999.

[76] B. Baugher, Personal Communication.

[77] B. Vigolo, A. Penicaud, C. Coulon, C. Sauder, R. Pailler, C. Journet, P. Bernier, P. Poulin, "Macroscopic fibers and ribbons of oriented carbon nanotubes," *Science,* vol. 290, pp. 1331-1334, 2000.

[78] P. L. Dickrell, S. B. Sinnott, D. W. Hahn, N. R. Raravikar, L. S. Schadler, P. M. Ajayan, W. G. Sawyer, "Frictional anisotropy of oriented carbon nanotube surfaces," *Tribology Letters,* vol. 18, pp. 59-62, 2005.

[79] L. C. Zhang, K. Mylvaganam, K. Q. Xiao, "The intrinsic frictional property of carbon nanotubes," *Advanced Materials Research,* vol. 32, pp. 1-4, 2008.

[80] C. M. Wang, Y. Q. Ma, Y. Y. Zhang, K. K. Ang, "Buckling of double-walled carbon nanotubes modeled by solid shell elements," *Journal of Applied Physics,* vol. 99, 2006.

[81] C. Q. Ru, "Effective bending stiffness of carbon nanotubes " *Physical Review B,* vol. 62, pp. 9973-9976, 2000.

[82] A. Sears, R. C. Batra, "Macroscopic properties of carbon nanotubes from molecular-mechanics simulations," *Physical Review B,* vol. 69, 2004.

[83] G. M. Odegard, T. S. Gates, L. M. Nicholson, K. E. Wise, "Equivalent-continuum modeling of nano-structured materials," *Composites Science and Technology,* vol. 62, pp. 1869-1880, 2002.

[84] K. M. Liew, C. H. Wong, M. J. Tan, "Twisting effects of carbon nanotube bundles subjected to axial compression and tension," *Journal of Applied Physics,* vol. 99, 2006.

[85] Q. Zhao, M. B. Nardelli, J. Bernholc, "Ultimate strength of carbon nanotubes: A theoretical study," *Physical Review B,* vol. 65, 2002.

[86] T. Chang, W. Guo, X. Guo, "Buckling of multiwalled carbon nanotubes under axial compression and bending via a molecular mechanics model," *Physical Review B,* vol. 72, 2005.

[87] K. M. Liew, C. H. Wong, M. J. Tan, "Buckling properties of carbon nanotube bundles," *Applied Physics Letters,* vol. 87, 2005.
[88] K. M. Liew, C. H. Wong, M. J. Tan, "Tensile and compressive properties of carbon nanotube bundles," *Acta Materialia,* vol. 54, pp. 225-231, 2006.
[89] T. Chang, "Torsional behavior of chiral single-walled carbon nanotubes is loading direction dependent," *Applied Physics Letters,* vol. 90, 2007.
[90] X. Wang, G. Lu, Y. J. Lu, "Buckling of embedded multi-walled carbon nanotubes under combined torsion and axial loading," *International Journal of Solids and Structures,* vol. 44, pp. 336-351, 2007.
[91] S. P. Timoshenko, J. M. Gere, *Theory of Elastic Stability*. New York: McGraw-Hill, 1963.
[92] X. Wang, H. K. Yang, K. Dong, "Torsional buckling of multi-walled carbon nanotubes," *Materials Science and Engineering A,* vol. 404, pp. 314-322, 2005.
[93] M. B. Nardelli, B. I. Yakobson, J. Bernholc, "Brittle and ductile behavior in carbon nanotubes," *Physical Review Letters,* vol. 81, pp. 4656-4659, 1998.
[94] N. Maluf, *An Introduction to Microelectromechanical Systems Engineering*. Boston: Artech House, 2000.
[95] K. E. Petersen, "Silicon as a mechanical material," *Proceedings of the IEEE,* vol. 70, pp. 420-457, 1982.
[96] H. Wang, K. T. Ramesh, "Dynamic strength and fragmentation of hot-pressed silicon carbide under uniaxial compression," *Acta Materialia,* vol. 52, pp. 355-367, 2004.
[97] Electricity Storage Association, "Technology comparisons," http://electricitystorage.org/tech/technologies_comparisons_sizeweight.htm.
[98] Advertised specifications for A. Lange & Soehne's 31-day watch, http://www.alange-soehne.com/en/watches/lange_31_movement.php?ID=cc332d1a2ea3b999fd38407.
[99] M. Madou, *Fundamentals of Microfabrication*. Boca Raton, 2002.
[100] B. Lukic, J. W. Seo, E. Couteau, K. Lee, S. Gradecak, R. Berkecz, K. Hernadi, S. Delpeux, T. Cacciaguerra, F. Beguin, A. Fonseca, J. B. Nagy, G. Csanyi, A. Kis, A. J. Kulik, L. Forro, "Elastic modulus of multi-walled carbon nanotubes produced by catalytic chemical vapour deposition," *Applied Physics A,* vol. 80, pp. 695-700, 2005.
[101] P. B. Koeneman, I. J. Busch-Vishniac, K. L. Wood, "Feasibility of micro power supplies for MEMS," *Journal of Microelectromechanical Systems,* vol. 6, pp. 355-362, 1997.
[102] A. Burke, "Ultracapacitors: why, how, and where is the technology," *Journal of Power Sources,* vol. 91, pp. 37-50, 2000.
[103] G. Cacciola, V. Antonucci, S. Freni, "Technology up date and new strategies on fuel cells," *Journal of Power Sources,* vol. 100, pp. 67-79, 2001.
[104] C. K. Dyer, "Fuel cells for portable applications," *Journal of Power Sources,* vol. 106, pp. 31-34, 2002.
[105] M. R. Brent, J. M. Papadopoulos, "Regenerative braking systems for bicycles," USPTO, Ed. United States, 1988.
[106] D. Tuite, "Get The Lowdown On Ultracapacitors," http://electronicdesign.com/Articles/Index.cfm?AD=1&ArticleID=17465&pg=1.
[107] J. Y. Huang, S. Chen, Z. Q. Wang, K. Kempa, Y. M. Wang, S. H. Jo, G. Cheng, M. S. Dresselhaus, Z. F. Ren, "Superplastic carbon nanotubes," *Nature,* vol. 439, p. 281, 2006.

[108] Y. A. Kim, H. Muramatsu, T. Hayashi, M. Endo, M. Terrones, M. S. Dresselhaus, "Thermal stability and structural changes of double-walled carbon nanotubes by heat treatment," *Chemical Physics Letters,* vol. 398, pp. 87-92, 2004.

[109] S. Das, D. P. Arnold, I. Zana, J. W. Park, J. H. Lang, M. G. Allen, "Multi-watt electric power from a microfabricated permanent-magnet generator," in *18th IEEE International Conference on Micro Electro Mechanical Systems (MEMS 2005)*, 2005, pp. 287-290.

[110] Y. B. Jeon, R. Sood, J. H. Jeong, S. G. Kim, "MEMS power generator with transverse mode thin film PZT," *Sensors and Actuators A,* vol. 122, pp. 16-22, 2005.

[111] S. Roundy, P. K. Wright, J. Rabaey, "A study of low level vibrations as a power source for wireless sensor nodes," *Computer Communications,* vol. 26, pp. 1131-1144, 2003.

[112] N. G. Stephen, "On energy harvesting from ambient vibration," *Journal of Sound and Vibration,* vol. 293, pp. 409-425, 2005.

[113] J. L. Steyn, S. H. Kendig, R. Khanna, T. M. Lyszczarz, S. D. Umans, J. U. Yoon, C. Livermore, J. H. Lang, "Generating electric power with a MEMS electroquasistatic induction turbine-generator," in *18th IEEE International Conference on Micro Electro Mechanical Systems*, 2005, pp. 614-617.

[114] S. Whalen, M. Thompson, D. Bahr, C. Richards, R. Richards, "Design, fabrication and testing of the P3 micro heat engine," *Sensors and Actuators A,* vol. 104, pp. 290-298, 2004.

[115] D. de Carle, *Watch and Clock Encyclopedia*. New York: Bonanza Books, 1977.

[116] M. Denny, "The pendulum clock: a venerable dynamical system," *European Journal of Physics,* vol. 23, pp. 449–458, 2002.

[117] M. Kesteven, "On the mathematical theory of clock escapements," *American Journal of Physics,* vol. 46, pp. 125-129, 1978.

[118] C. D. Richards, M. J. Anderson, D. F. Bahr, R. F. Richards, "Efficiency of energy conversion for devices containing a piezoelectric component," *Journal of Micromechanics and Microengineering,* vol. 14, pp. 717-721, 2004.

[119] Z. L. Wang, J. Song, "Piezoelectric nanogenerators based on zinc oxide nanowire arrays," *Science,* vol. 312, pp. 242-246, 2006.

[120] Q. Wang, X. Du, B. Xu, L. E. Cross, "Electromechanical coupling and output efficiency of piezolectric bending actuators," *IEEE Transactions on Ultrasonics, Ferroelectrics, and Frequency Control,* vol. 46, pp. 638-646, 1999.

[121] F. J. Britten, *Watch and Clockmaker's Handbook*. Woodbridge, England: Baron Publishing, 1976.

[122] W. I. Milham, *Time and Timekeepers*. New York: The MacMillan Company, 1929.

[123] M. Headrick, "Clock and Watch Escapement Mechanics," http://www.geocities.com/mvhw/TToc.htm.

[124] J. E. Shigley, C. R. Mischke, *Mechanical Engineering Design*. Boston: McGraw-Hill Inc., 1977.

[125] J. H. Cho, R. F. Richards, D. F. Bahr, C. D. Richards, "Efficiency of energy conversion by piezoelectrics," *Applied Physics Letters,* vol. 89, 2006.

Appendix 1

Optimization of energy density for multiple deformation modes

```
function [] = optimize_energy_density()

% This function takes a maximum compressive stress and maximum
% tensile stress and computes the maximum strain energy density that is
% possible in the structure by varying values of sigma_zz and tau_ztheta.
% Principal stresses sigma1 and sigma2 are varied over their allowable
% range to find the optimized objective function.

% Parameter definition
E=1e12;                 % Young's modulus
G=450e9;                % Shear modulus

sigmac = -50e9;         % Limiting compressive stress
sigmat = 100e9;         % Limiting tensile stress

% Radius of failure envelope circles for tension (r2) and compression (r1)
r1 = abs(sigmac/2);
r2 = sigmat/2;

% X-coordinate of left and right intercepts between tangent line and
% tensile and compressive failure envelope circles
xlim_comp = -2*r1*r2/(r1+r2);
xlim_tens = 2*r1*r2/(r1+r2);

% Define range of principal stresses
sigma2 = sigmac:.1e9:0;
sigma1 = 0:.1e9:sigmat;

% Initialize variables
track_sigma1=0;             % sigma1 at max energy density
track_sigma2=sigmac;        % sigma2 at max energy density
track_tau_ztheta = 0;       % tau_ztheta at max energy density
max_energy = 0;             % Maximum energy density


% Dimensions of the CNT
diameter = 1.36e-9;             % CNT diameter
n=1;                            % number of shells
ro = diameter/2+0.17e-9*n;      % outer radius
```

```
ri = diameter/2-0.17e-9*n;              % inner radius
ratio_tension = (ro^2-ri^2)/ro^2;
ratio_tors = (ro^4-ri^4)/ro^4;

% Begin computation

for i=1:length(sigma1)
   for j=1:length(sigma2)

      centre_x = (sigma1(i)+sigma2(j)) /2;      % center of current sigma1, sigma2 circle
      peak_y = (sigma1(i)-sigma2(j))/2;         % max tau of current sigma1, sigma2 circle

      % Check if sigma1, sigma2 combination is admissible
      if ((centre_x <= xlim_comp & peak_y <= sqrt(r1^2 - (centre_x+r1)^2) )  | (( peak_y <= ( (r2-
r1)/(2*sqrt(r1*r2)) * (sigma1(i)+sigma2(j))/2 + sqrt(r1*r2) & centre_x>=xlim_comp &
centre_x<=xlim_tens)) | (centre_x >=xlim_tens & peak_y <= sqrt(r2^2 - (centre_x-r2)^2) ))

         % Compute energy density of current sigma1, sigma2 values and
         % compare it to the previous maximum
         sigmazz = sigma1(i)+sigma2(j);
         tau_ztheta = sqrt(-sigma1(i)*sigma2(j));
         energy = 1/(2*E) * sigmazz^2* ratio_tension + 1/(4*G)*tau_ztheta^2* ratio_tors;
         track_energy(i,j) = energy;

         if energy>max_energy
            max_energy = energy;                % max energy density to date
            track_sigma1 = sigma1(i);           % sigma1 at max energy
            track_sigma2 = sigma2(j);           % sigma2 at max energy
            track_tau_ztheta = tau_ztheta;      % tau_ztheta at max energy
            track_sigmazz = sigmazz;            % sigmazz at max energy
         end;
      else
         track_energy(i,j) = 0;     % Not an admissible sigma1, sigma1 combination
      end;
   end;
end;

% Print results
max_energy          % Maximum energy density found
track_sigma1        % sigma1 value at maximum energy density
track_sigma2        % sigma2 value at maximum energy density
track_tau_ztheta    % corresponding tau_ztheta value at maximum energy density
track_sigmazz       % corresponding sigmazz value at maximum energy density
```

```
% Convert sigmazz and tau_ztheta back into principal stresses, for verification
s1 = track_sigmazz/2 + sqrt(track_sigmazz^2/4+track_tau_ztheta^2)
s2 = track_sigmazz/2 - sqrt(track_sigmazz^2/4+track_tau_ztheta^2)

% Compare resulting energy density value with energy density of pure tension
compare = 1/(2*E) * sigmat^2 * ratio_tension

% 3D Plot of resulting energy density over range of sigma1 and sigma2 values
mesh(sigma2,sigma1,track_energy)
```

Appendix 2

Input file parameters.m for Simulink model unitcell.mdl

```
% Model parameters

strain_max = 0.06;          % maximum strain applied to the spring

% Material properties
E_Si = 160e9;               % Young's modulus of silicon
rho_Si = 2330;              % density of silicon
sigma_Si = 7e9;             % strength of silicon
E_SiC = 450e9;              % Young's modulus of silicon carbide
rho_SiC = 3400;             % density of silicon carbide
sigma_SiC = 21e9;           % strength of silicon carbide

% CNT dimensions
CNTdm = 30e-6;              % diameter of the spring
LengthCNT=800e-6;           % length of the spring
A_CNT = pi*(CNTdm/2)^2;     % cross-section of the spring
E_CNT=1e12;                 % CNT Young's modulus

% Elastic energy stored
U = 1/2 * E_CNT * strain_max^2 * A_CNT * LengthCNT * 0.91 * 0.64

% Screw dimensions
l=30e-6;                    % screw pitch
dm=100e-6;                  % diameter of screws
mu=0.05;                    % coefficient of friction of screws

% Unwinding screw efficiency
screw_efficiency = (pi*dm)/l*(l-pi*dm*mu)/(pi*dm+mu*l)

% Number of escape wheel rotations for the screw to unwind
rots_to_unwind = strain_max*LengthCNT / (2*l)

% Escape wheel parameters
LengthEscape=300e-6;        % length of escape wheel
douter=1000e-6;             % outer diameter of escape wheel
dinner=douter*3/4;          % inner diameter of escape wheel
router=douter/2             % radius outer of escape wheel, length pallet arm
rinner=dinner/2;            % radius inner of escape wheel
```

```
mass_wheel = rho_SiC*pi*((0.25*(router^2 - rinner^2))+((0.75*router)^2-
(0.625*router)^2))*LengthEscape                    % mass of the escape wheel
inertia_wheel=1/2*mass_wheel*((3/4*router)^2+(5/8*router)^2)        % wheel inertia
moment_wheel_noeps = E_CNT*A_CNT*0.64*0.91*dm * (-pi*mu*dm+l)/(pi*dm+mu*l);
bo=router/2*cos(pi/6)
ho=router/2*sin(pi/6)
x_displacement = bo*tan(38*pi/180)-ho

% Pallet parameters
m1=rho_Si*router*0.08*router*LengthEscape;
m2=12/180 *rho_Si* pi*((1.05*router)^2-(0.95*router)^2)*LengthEscape;
m_pallet=2*m1+m2                                                    % pallet mass
I_pallet = 2*1/3*m1*router^2 + 12/180*1/2*m2*((1.05*router)^2+(0.95*router)^2)
                                                                    % pallet inertia

% Cantilever parameters
L= router * 8                          % cantilever length
W = L/5                                % cantilever width
h = W/4                                % cantilever height
m_beam = 3400*L*W*h;                   % actual mass of the cantilever
m_eff = 33/140*m_beam;                 % effective cantilever mass
k = E_SiC*W*h^3/(4*L^3);               % cantilever spring constant

% Damping coefficients
bm=0.00045;          % mechanical damping coefficient
be=0.001;            % electrical damping coefficient
b=bm+be;             % total damping coefficient

% Frequency estimates
wo = sqrt(k/m_eff - (b/(2*m_eff))^2);
fo = wo/(2*pi)
calculate_f = 1/(2*pi)*sqrt(k/(m_eff+I_pallet*(cos(pi/6))^4/(2*bo^2)))

% Piezoelectric properties
eps=1.505e-12;                         % dielectric constant
k31 = 0.344196;                        % electromechanical coupling factor
C=eps * L * W / (0.5e-6);              % capacitance of piezoelectric layer
Re = be/C / sqrt(4*m_eff^2*wo^4*k31^4-wo^2*be^2)     % external load resistance
be = 2*m_eff*wo^2 * k31^2 / sqrt(wo^2+1/(Re*C)^2)    % electrical damping coefficient

% Mass of the support structure
mass_Support = E_CNT*0.06/sigma_SiC * A_CNT * 0.91 * 0.64 * LengthCNT * rho_SiC

% Percentage of CNTs by mass
```

```
CNT_density = 2200;                                    % density of CNT spring
mass_CNT = A_CNT*LengthCNT*CNT_density*0.91*0.64       % mass of the spring
mass_Escape = mass_wheel                               % mass of escape wheel
mass_Screw = 2*rots_to_unwind*l*3*pi*(dm/2)^2*rho_Si;  % mass of screws
mass_Pallet = m_pallet                                 % mass of pallet
CNT_percent = mass_CNT / (mass_CNT + mass_Escape + mass_Screw + mass_Pallet +
m_beam*2 + mass_Support) * 100                                  % percentage of CNTs
by mass

% Maximum stresses in the cantilevers and escape wheel teeth
delta = 4e-5;                                  % maximum cantilever displacement
largest_force = delta*E_SiC*W*h^3/(4*L^3);     % maximum force applied to cantilever
sigma_max = 6*largest_force*L/(W*h^2)          % maximum stress in cantilever
Max_stress_gear_teeth = 6*router/4 / ( (router*pi/40)^2 * LengthEscape ) *
moment_wheel_noeps * strain_max / router       % maximum stress in escape wheel teeth
```

Appendix 3

Simulink Model: unitcell.mdl

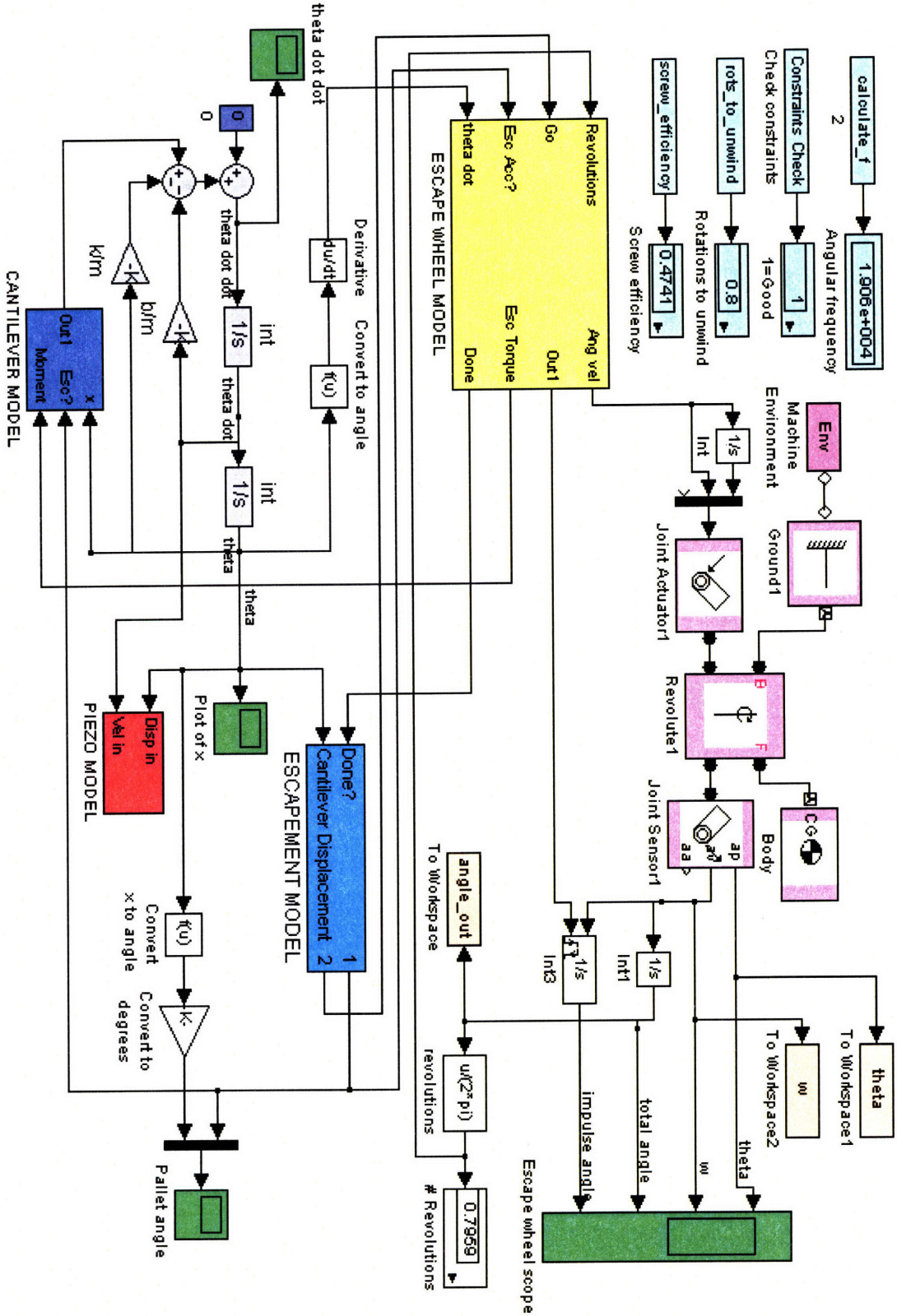

unitcell/PIEZO MODEL

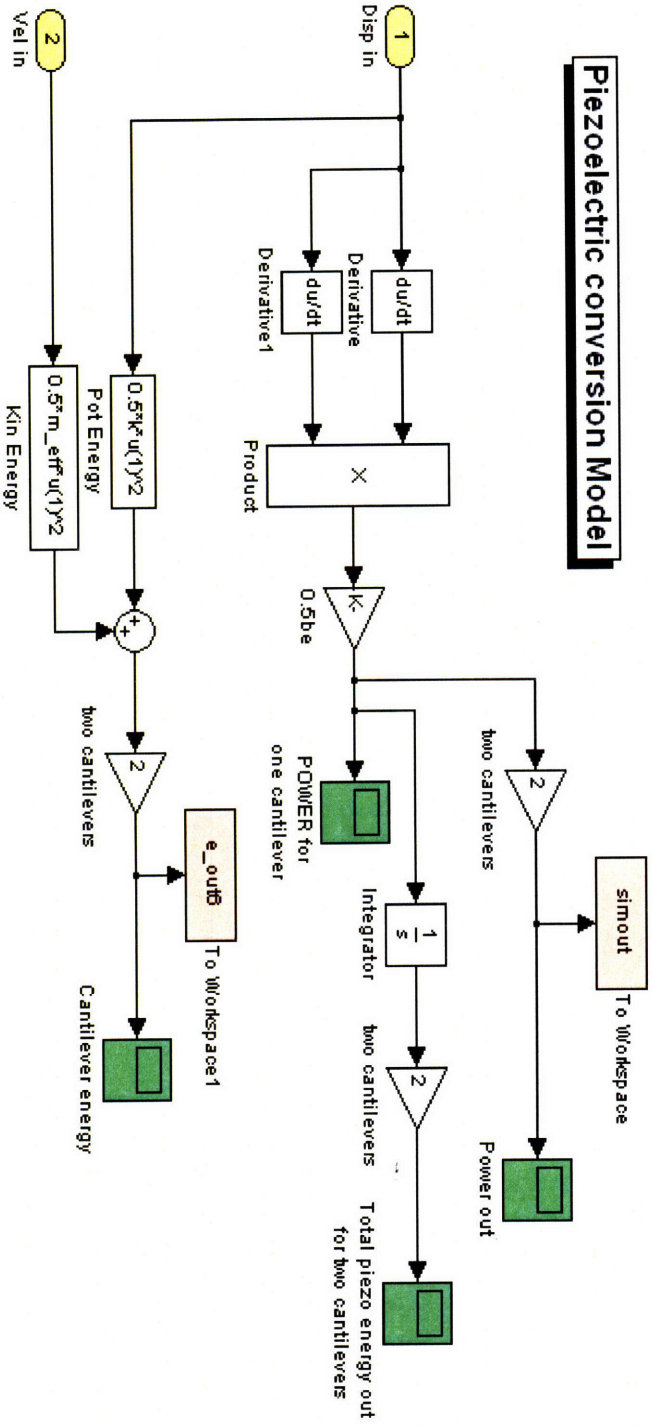

unitcell/ESCAPEMENT MODEL